OPTIMIZING HEAT EXCHANGER PARAMETERS OF A JOULE-THOMSON
CRYOGENIC COOLER TO IMPROVE THE COOLING PERFORMANCE

A THESIS SUBMITTED TO
THE GRADUATE SCHOOL OF NATURAL AND APPLIED SCIENCES
OF
MIDDLE EAST TECHNICAL UNIVERSITY

BY

MURAT BAKI

IN PARTIAL FULFILLMENT OF THE REQUIREMENTS
FOR
THE DEGREE OF DOCTOR OF PHILOSOPHY
IN
MECHANICAL ENGINEERING

NOVEMBER 2018

Approval of the thesis:

OPTIMIZING HEAT EXCHANGER PARAMETERS OF A JOULE-THOMSON CRYOGENIC COOLER TO IMPROVE THE COOLING PERFORMANCE

submitted by **MURAT BAKI** in partial fulfillment of the requirements for the degree of **Doctor of Philosophy in Mechanical Engineering Department, Middle East Technical University** by,

Prof. Dr. Halil Kalıpçılar
Dean, Graduate School of **Natural and Applied Sciences**　　＿＿＿＿＿＿＿＿

Prof. Dr. M. A. Sahir Arıkan
Head of Department, **Mechanical Engineering**　　＿＿＿＿＿＿＿＿

Assoc. Prof. Dr. Hanife Tuba Okutucu Özyurt
Supervisor, **Mechanical Engineering, METU**　　＿＿＿＿＿＿＿＿

Assoc. Prof. Dr. Cüneyt Sert
Co-Supervisor, **Mechanical Engineering, METU**　　＿＿＿＿＿＿＿＿

Examining Committee Members:

Prof. Dr. Abdullah Ulaş
Mechanical Engineering, METU　　＿＿＿＿＿＿＿＿

Assoc. Prof. Dr. Hanife Tuba Okutucu Özyurt
Mechanical Engineering, METU　　＿＿＿＿＿＿＿＿

Assist. Prof. Dr. Özgür Bayer
Mechanical Engineering, METU　　＿＿＿＿＿＿＿＿

Prof. Dr. Murat Köksal
Mechanical Engineering, Hacettepe University　　＿＿＿＿＿＿＿＿

Assoc. Prof. Dr. Murat Kadri Aktaş
Mechanical Engineering, TOBB ETU　　＿＿＿＿＿＿＿＿

Date: 02.11.2018

I hereby declare that all information in this document has been obtained and presented in accordance with academic rules and ethical conduct. I also declare that, as required by these rules and conduct, I have fully cited and referenced all material and results that are not original to this work.

Name, Surname: Murat Baki

Signature:

ABSTRACT

OPTIMIZING HEAT EXCHANGER PARAMETERS OF A JOULE-THOMSON CRYOGENIC COOLER TO IMPROVE THE COOLING PERFORMANCE

Baki, Murat
Doctor of Philosophy, Mechanical Engineering
Supervisor: Assoc. Prof. Dr. Hanife Tuba Okutucu Özyurt
Co-Supervisor: Assoc. Prof. Dr. Cüneyt Sert

November 2018, 126 pages

Cryocoolers are one of the key components of cooled infrared (IR) imaging systems, where it is not possible to form an image in photon detectors without decreasing the sensor temperature to cryogenic temperatures. In detector cooling applications where low cool down times, small size and weight are required, mostly Joule Thomson (JT) cryocoolers are preferred. The aim of this study is to analyze the heat exchanger of a JT cryocooler operating with argon as the working gas, numerically and optimize its design parameters. For this purpose, a numerical model is built to solve Navier-Stokes and heat transfer equations. Using the numerical model, an optimization study is applied using stochastic method to maximize the specific cooling power of the cryocooler and minimize the shell side pressure drop. The possible optimization parameters are determined as total length of the heat exchanger, capillary tube diameter, capillary tube wall thickness, fin density, fin thickness and fin length. The design parameters are varied within certain limits. A result cloud is obtained using full factorial method. The two contradicting objectives are brought together by weighted averages approach and an optimization function is formed. The optimum geometry which maximizes the optimization function is searched using grid search method. Finally, a second iteration of the optimization is performed by using the optimum

geometry obtained from the first iteration. An optimum geometry is obtained, where flow rate is decreased by 46%, which results in an increase of the operation time, and the shell side pressure drop is decreased by 90%, which results in a decrease of the target body working temperature.

Keywords: Joule-Thomson Cryocooler, Microscale Heat Transfer, Detector Cooling, Numerical Modeling, Optimization

ÖZ

JOULE-THOMSON KRİYOJENİK SOĞUTUCULARI ISI DEĞİŞTİRİCİSİ ÖZELLİKLERİNİN SOĞUTMA PERFORMANSINI İYLEŞTİRMEYE YÖNELİK ENİYİLEMESİ

Baki, Murat
Doktora, Makina Mühendisliği
Tez Danışmanı: Doç. Dr. Hanife Tuba Okutucu Özyurt
Ortak Tez Danışmanı: Doç. Dr. Cüneyt Sert

Kasım 2018, 126 sayfa

Kriyo-soğutucular soğutmalı kızılötesi (IR) görüntüleme sistemlerinin en önemli bileşenlerindendir. Foton detektörlerinde algılayıcı sıcaklığı kriyojenik sıcaklıklara düşürülmediği sürece görüntü oluşturulamaz. Düşük ilk soğuma süresi, küçük boyutlar ve ağırlığın önemli olduğu dedektör soğutma uygulamalarında çoğunlukla Joule-Thomson (JT) soğutucular kullanılır. Bu çalışmanın hedefi argon gazı ile çalışan bir JT soğutucunun ısı değiştiricisini sayısal yollarla incelemek ve en uygun tasarım boyutlarını belirlemektir. Bu amaçla, Navier-Stokes ve enerji denklemlerini çözmek üzere sayısal bir model oluşturulmuştur. Sayısal model kullanılarak stokastik yöntemle eniyileme çalışması gerçekleştirilmiştir. Eniyileme çalışmasının hedefleri sistemin birim kütlede soğutma gücü en yüksek ve kabuk tarafından akan akışın basınç düşüşü en düşük olacak şekilde en uygun tasarım boyutlarının belirlenmesidir. Eniyileme çalışmasında incelenen olası tasarım boyutları toplam uzunluk, kılcal boru çapı, kılcal boru et kalınlığı, kanat sıklığı, kanat uzunluğu ve kanat kalınlığıdır. Bu boyutlardan hedeflere etkisi düşük olanların eniyileme çalışmasında incelenmemesi için öncelikle bir hassasiyet analizi yapılmıştır. Seçilen tasarım boyutları belli aralıklarda incelenmiştir. Tüm boyut kombinasyonlarının değerlendirileceği şekilde bir sonuç bulutu oluşturulmuştur. Birbiriyle çelişen iki hedefin bir arada

incelenebilmesi için ağırlıklı ortalamalarının toplanması yoluyla bir eniyileme fonksiyonu oluşturulmuştur. En iyi boyutlar, oluşturulan sonuç bulutunda eniyileme fonksiyonunun en yüksek değerinin tespit edilmesi ile belirlenmiştir. Son olarak tespit edilen en iyi boyutlar ikinci bir eniyileme hesaplamasının başlangıç boyutları olarak kullanılmıştır. Bu sayede en iyi boyutlar tespit edilmiştir. Önerilen yeni boyutlar ile çalışma debisi %46 oranında azaltılabilmiştir. Bu sayede soğutucunun çalışma süresi uzayacaktır. Ayrıca kabuk akışı basınç düşüşü %90 oranında azaltılmıştır. Bu sayede soğutulmak istenen hedefin çalışma sıcaklığının düşürülmesi sağlanmıştır.

Anahtar Kelimeler: Joule-Thomson Kriyo-Soğutucu, Mikro Boyutlarda Isı Transferi, Detektör Soğutma, Sayısal Modelleme, Eniyileme

To my family. Past, present, future …

ACKNOWLEDGMENTS

TABLE OF CONTENTS

LIST OF TABLES

LIST OF FIGURES

FIGURES

LIST OF ABBREVIATIONS

EGM: Entropy Generation Minimization

IR : Infrared

JT : Joule – Thomson

LWIR: Long Wave IR

MCT: Mercury – Cadmium – Telluride

NETD: Noise Equivalent Temperature Difference

SLPM: Standard Liters Per Minute

SWIR: Short Wave IR

LIST OF SYMBOLS

Symbols		
A_{cross}	Cross sectional area	[mm^2]
Bi	Biot number	[-]
c_p	Specific heat	[J/g.K]
d	Diameter	[mm]
E	Availability	[W]
Ec	Eckert number	[-]
f	Fanning friction factor	[-]
G	Mass flux	[kg/m^2.s]
h	Convective heat transfer coefficient	[W/m^2.K]
i	Specific enthalpy	[kJ/kg]
I	Irreversibility	[W]
k	Thermal conductivity	[W/m.K]
L	Length	[mm]
$\dot{m}$	Mass flow rate	[SLPM]
n	Number (of)	[-]
Nu	Nusselt number	[-]
P	Pressure	[bar]
P_w	Wetted perimeter	[mm]
Pr	Prandtl number	[-]
q	Specific cooling power	[W/SLPM]
Q	Cooling power	[W]
R	Thermal resistance	[K/W]
Re	Reynolds number	[-]
S	Pitch	[mm]
s	Specific entropy	[kJ/kg.K]
t	Thickness	[mm]
T	Temperature	[K]
w	Weight (of objectives)	[-]
V	Velocity	[m/s]

Greek Symbols		
ρ	Density of the fluid	[kg/m3]
ε	Emissivity	[-]
σ	Stefan-Boltzmann constant	[W/m2.K4]
μ	Dynamic viscosity	[Pa.s]
μ_{JT}	Joule-Thomson coefficient	[K/bar]
φ	Optimization function	[-]
η	Efficiency	[-]

Subscripts	
2nd	Second law (efficiency)
amb	Ambient
atm	Atmospheric
c	Finned capillary tube
cond	Conduction heat transfer
conv	Convection heat transfer
e	Entrance (length)
ext	External
f	Fin
hel	Helical
hex	Heat exchanger
hyd	Hydraulic (diameter)
i	Inside
JT	Joule-Thomson
m	Mandrel
norm	Normalized
o	Outside
s	Shield
sat	Saturation
ssf	Shell side flow
tsf	Tube side flow
w	Wall

CHAPTER 1

INTRODUCTION

1.1. Motivation and Objective

In this study, the heat exchanger section of a Joule Thomson (JT) cryocooler is numerically investigated. JT coolers make use of JT expansion concept to reach cryogenic temperatures. As they offer short cool down time, small dimensions, high temperature stability and high heat flux, JT cooler are preferred in applications including infrared (IR) sensors [1, 2], liquefaction systems [3, 4], cryosurgery and cryo-preservation [5, 6], superconductivity [7], space applications [8], etc. The photon detectors used in thermal imaging systems that require fast response and high image quality are cooled by JT coolers down to cryogenic temperatures in order to detect radiation at IR wavelength.

JT coolers are mostly operated at critical operation conditions. The working temperature is at cryogenic temperatures near liquefaction temperatures of the working gases (77 K for nitrogen and 87 K for argon). Small dimensions and cryogenic working temperature results in very high temperature gradients within the system. The working pressure required in JT coolers is very high, may change from 100 bar up to 500 bar [9]. The operation time is limited when operated in open cycle [10]. To meet all these system requirements, it is important to optimize the design of a JT heat exchanger. As the geometry and working conditions are highly complex, it is not possible to derive direct relations between design parameters and the objectives. The effect of each design parameter, and combined effect of several design parameters can only be analyzed through a numerical model of the system.

This study is carried out to improve the heat exchanger performance of a JT cooler to meet the operation requirements of an IR sensor while considering optimization

constraints imposed by detector size (hence cooling requirement), thermodynamic state requirements of the working gas, as well as fabrication limitations. The optimization is conducted through a numerical model of the heat exchanger, which is built using thermal and physical interactions of the fluid and solid bodies. A multi-objective optimization is done using a stochastic method. The objectives are determined as the maximization of specific cooling power (which is denoted as q throughout the study) and at the same time minimization of the shell side pressure drop. The two objectives contradict with each other, therefore a pareto optimal solution is searched.

1.2. Scope and Contribution

In the current study, a numerical model of the heat exchanger section of a JT cryocooler is built using Navier-Stokes equations, heat transfer and friction coefficient correlations for gas flows inside the cooler and energy equations of solid bodies. The code is first validated using a widely cited reference case [11] from the literature. Once the model is validated, several improvements are made on the numerical model. As the first modification, the friction correlation for tube side flow which is wrongly used in several studies is reconsidered and corrected. Secondly, the change of enthalpy with pressure is employed within the energy equation of gases. The friction correlation used for the shell side flow is changed with a more suitable one suggested for Collins tubing [12], which is applied for the first time in this study. The boundary conditions of shell side flow are redefined so that an optimization study can be performed. Finally, the change in emissivity of heat exchanger casing (shield) material with temperature is considered.

After finalizing the numerical model, a sensitivity analysis is followed to study the effects of possible design parameters, namely the heat exchanger length, finned capillary inner diameter, finned capillary wall thickness, fin pitch, fin thickness and fin length on selected objectives. The first objective is to maximize q by changing the geometric parameters. The second objective is to minimize the shell side pressure

2

drop. The results of sensitivity analysis are used as a pre-optimization step where the suitable design parameters and better starting values are determined for the optimization study. The study is finalized by an optimization study, where an optimization function is built from the two objectives. The optimum geometry resulting in maximized optimization function is determined.

The present study is important as it fixes commonly repeated errors in the friction coefficient definition while making further improvements by considering the change in enthalpy with pressure and change in emissivity with temperature. The friction correlation suggested in this study for the shell side friction coefficient, where the geometry is similar with the JT cooler shell side and the Reynolds range fits, was not used in JT cooler analysis before. Several improvements applied in the current study were separately considered in literature; such as including the change of enthalpy with pressure or defining shell side flow exit at atmospheric pressure, instead of inlet pressure at a measured value. However, these improvements are all considered together for the first time in this study. The study is also unique in the literature in taking q and the shell side pressure drop as the two objectives in the JT heat exchanger optimization.

1.3. Outline of the Thesis

The first chapter of the thesis briefly describes the motivation, scope and outline of the study. Background and a thorough literature review can be found in chapter 2. In the literature review, first IR imaging is introduced as the planned application area of JT heat exchangers. Details about cryocoolers and heat exchangers used in cryocoolers are given next. Then a description of JT cryocoolers are presented. The JT effect, JT cycle and subcomponents of a JT cooler are included. The literature review is finalized with a summary of the numerical as well as optimization studies performed on JT coolers up to date. Finally, a critical assessment of these studies is given and gaps in the literature are identified.

Chapter 3 presents the details of the numerical model developed in the present study for the analysis of JT heat exchangers. The assumptions needed for the simplification of Navier-Stokes equations and their justifications are given. The final forms of the Navier-Stokes equations after the application of assumptions and the correlations used for heat transfer and friction coefficients are provided. The derivations of the equations are presented in Appendix A. Variable thermophysical and transport properties of the working gas are considered, and they are evaluated from equations given in [13] and [14]. The model built for the calculation of thermophysical properties is presented in Appendix B. Finally, the solution algorithm of the numerical model, discretization of equations and boundary conditions are given. Verification of the numerical model is then provided and modifications for further improvements are discussed.

Chapter 4 describes the optimization study. First, a brief summary is given about the selection of the optimization method. Then, optimization constraints are discussed. A sensitivity analysis is performed where effect of each possible design parameter on selected objectives are studied. Design parameters which do not have significant effect on the objectives are eliminated. Using the sensitivity analysis, better initial values for the selected design parameters are suggested so that the number of results obtained in the optimization study which are out of constraint limits are decreased. The study is named as pre-optimization. Another advantage of the pre-optimization is that number of levels required during the optimization where design parameters are varied is decreased. This way the complexity and operation time of the optimization is decreased. From the objectives, an optimization function is built through the relative importance of objectives on each other. A result cloud for the optimization function is generated, where the values of design parameters are varied along certain ranges. A full factorial approach is adopted to build the result cloud, where every possible combination of each design parameter is considered. The geometry which corresponds to the maximum value of optimization function is determined using a grid search approach. The optimization is further iterated by updating the ranges through which

the design parameters are varied. By comparing the values of objectives and geometry suggested at each iteration, the study is finalized with a final, optimum geometry.

CHAPTER 2

BACKGROUND AND LITERATURE REVIEW

2.1. IR Imaging

IR imaging has found many practical applications ever since its discovery around 1960's [15]. In IR imaging, a system/device (i.e. a thermal camera, etc.) which contains a material sensitive to IR radiation is directed to an object/space (the scene). An image of the scene is formed on a screen according to the temperature distribution throughout the scene. This image formed is called the thermal image. In other words, an IR imaging device allows imaging scenes with respect to the temperature distribution. There are several important advantages of IR imaging. First of all, it allows imaging at the absence of visible light (wavelength spectrum that the human eye is sensitive to). Second, it allows discrimination of targets, for example living bodies can be identified as their temperature is mostly higher than their surroundings. Finally, it allows imaging behind solid bodies up to some degree. This aspect can be used for example in biology or medicine, in detecting embryo, damaged tissues, etc. [16] Some other important usages of IR imaging are in guided missiles, space telescopes, fire detection systems, medical thermographic examination for early cancer detection, earth resource mapping, etc. [17].

It is known that every atom emits IR radiation as a result of electron movement between different energy levels [18]. For every wavelength, the intensity of the IR radiation is a function of temperature according to Wien's displacement law. For every temperature, an atom emits different intensities of IR radiation at different wavelengths, which may be seen from Figure 2.1. These IR wavelengths are sensed through IR detectors. IR detectors can be divided into two categories based on the sensing principle: thermal and photon detectors [19]. In thermal detectors the sensor

material absorbs IR wavelength. This absorption causes the temperature of the material to increase, which results in a change of physical property of the material (electrical resistance, bimetal effect, polarization, gas expansion, reflectivity, Peltier current, etc.) [19]. The property change is converted into an electrical signal. Similar to a digital camera, the sensor material of the thermal detector is divided into pixels. Electrical signal coming from each pixel is carried to a processor, which converts them into an image and prints on a screen.
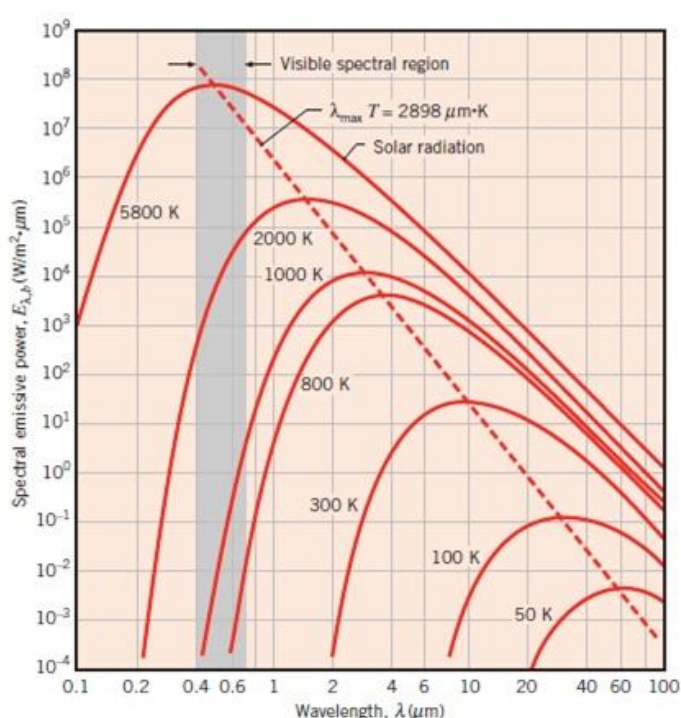
Figure 2.1. Spectral blackbody emissivity power at different temperatures [20]

In photon detectors, incident wavelength causes change in the electronic energy distribution [21]. The electrical output signal is formed through the excitation of these electrons due to the incident radiation. However, there are also some effects which causes electrons to move to higher energy levels, other than absorption of the incident IR radiation coming from the scene. The electrical signal generated due to these

sources is called noise signal. The noise results in distortions of the image formed on the screen. To have a clear image, the ratio of signal to noise should be high. One of the main sources of noise is temperature of the sensor material, which is called as the thermal noise [22]. To decrease the thermal noise, the sensor material is cooled to cryogenic temperatures. In other words, the photon detectors are operated together with a cryocooler system. The operation temperature of the detector is determined according to the wavelength to be detected, which varies from 10 to 150 K in most of the applications [19]. In space applications, where lower wavelengths are to be detected, temperatures down to 2 K may be required [23].

For systems where wavelengths to be detected are in the band between short wavelength IR (SWIR) to long wavelength IR (LWIR), the detector needs to be cooled to temperatures around 80 K (liquid nitrogen – liquid argon temperatures) [22]. JT cryocoolers are good candidates in these applications, as they utilize liquefied working fluids to cool the sensor material.

The photon detectors have many advantages over thermal detectors. First of all, the photon detectors have faster response time compared to the thermal detectors [19]. This is because the electric signal is directly generated by absorption of IR radiation in the photon detectors where in the thermal detectors, the electric signal generation due to change of a physical property takes a longer time. Secondly, the electric signal power is a function of the incident wavelength for the photon detectors. Depending on the sensor material, the signal power generated has a peak at certain wavelengths and zero outside a wavelength band [19]. The signal power generated in the thermal detectors in not a function of wavelength. As a result, the image formed by the photon detectors is sharper than the image formed by the thermal detectors. A thermal image formed by a photon detector, cooled by a JT cooler may be seen in Figure 2.2.

Figure 2.2. A thermal image formed using a photon detector, cooled by a Joule-Thomson cooler

Finally, the Noise Equivalent Temperature Difference (NETD), which is an important parameter to quantify the detector performance, is lower for the photon detectors compared with the thermal detectors [19]. NETD is the minimum temperature difference of the image formed due to the noise intensity, therefore can be considered as a measure of the noise-to-signal ratio [24]. To reach lower NETD value, the temperature distribution throughout the sensor material needs to be uniform and should not vary with time. Compared with other cryocoolers, JT coolers result in both more uniform and more steady temperature. NETD values reached with JT coolers are lower.

2.2. Cryogenics

Cryogenics is the area of science which deals with very low temperatures. The upper limit for the cryogenic temperatures is not well defined but mostly agreed as 120 K. Most of the fluids used in many refrigeration systems have boiling point above 120 K. Only some fluids (helium, hydrogen, neon, nitrogen, argon, carbon monoxide, oxygen, methane, etc.) have boiling/condensation temperature below 120 K, which are the key fluids used in the cryogenic applications [17]. Cryogenic temperatures are required in many fields today. Some practical applications are liquefaction of gases for transportation (LNG, etc.), purification of gases, achieving high vacuum (cryopumping), preservation of organic material (blood, tissue, foods, etc.), some

medical usages (cryosurgery, cryotherapy etc.) and using material properties at cryogenic temperatures (superconductivity, sensing IR radiation, decreasing rubber temperature below glass transition temperature for grinding, decreasing wear and improving life of cutting tools, increasing yield strength of pressure vessels during manufacturing, etc.) [17].

A very common usage of cryogenics other than IR imaging is in the field of superconductivity. Magnetic fields of certain substances (metals and alloys) are increased in cryogenic temperatures due to the loss of the electrical resistance at these temperatures [25]. This effect is being used in the magnetic trains (Maglev, etc.), MRI/NMR machines, particle accelerators, superconducting motors or gyroscopes, electric power transmission, etc. Since their first development, over 22.000 MRI magnets are in use today [23]. Electric power transmission is another very important application of the superconductors, as electricity is being used in every field of daily life. Theoretically, every component of an electric power generation and transmission system may be replaced by a superconductor device which has a higher efficiency. However, the large-scale usage of the electric power limits the use of the superconductors to only some areas and the rest of the transmission system is built through conventional components [26]. The superconducting materials may be used either instead of the resistive conductors (cables, motors, generators, transformers) or in areas where the conventional components cannot be used or limit the application severely (superconducting magnetic energy storage – SMES, fault current limiters - FCL, fault current controllers - FCC, etc.) [26].

2.3. Cryocoolers

To reach cryogenic temperatures, special cryogenic cooling devices are used. In some applications a cryostat filled with cryogenic fluid can be used (passive cooling). Some applications require cryocooling devices which provide continuous cooling (active cooling). These devices differ in design according to the needs of the application: temperature to be reached, cooling power (or amount of liquefied gas) needed, cool

down time, volume and mass limitations of the system, etc. The suitable cryogenic refrigeration cycle is selected according to these requirements. Sub-components of the cryocoolers are defined based on the refrigeration cycle to be used. Sub-components of most of the cryocoolers can be divided into 3 main parts: Hot chamber, heat exchanger and cold chamber [17]. A schematic representation of sub-components of a cryocooler can be found in Figure 2.3.
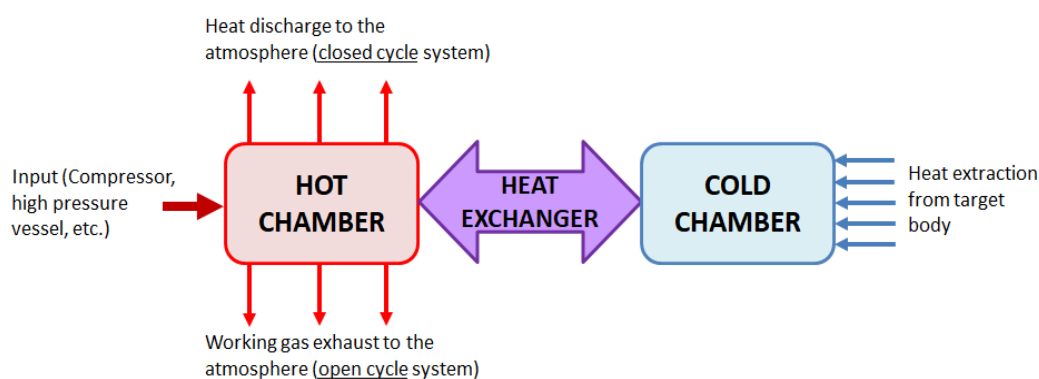
Figure 2.3. A simple representation of the sub-components of a cryocooler

Hot chamber is the place where necessary input is given to the system; such as work input (e.g. compressor), gas input (high pressure vessel) etc. In closed cycle systems, the working fluid discharges heat to the atmosphere at hot chamber. Cold chamber is the part where the working fluid reaches cryogenic temperatures, mostly through an expansion process. Heat extraction from the target system occurs in the cold chamber. The final subcomponent of the cryocooler systems is the heat exchanger, where the temperature of the working fluid flowing from the hot chamber to the cold chamber decreases. Due to this temperature decrease, the working fluid is able to reach cryogenic temperature in the cold chamber. Kanoğlu et al. [27] stated that in a liquefaction process if effectiveness of the heat exchanger is decreased from 100% to 96.5%, amount of liquid obtained decreases by 22%. For a cryocooler working with nitrogen gas, there may not be any liquefaction for a heat exchanger with effectiveness

less than 85% [12]. Heat exchangers constitute 20-30% of the total investment cost for liquefaction systems (air separation, LNG plants, etc.) [28]. Therefore, it is important to optimize the heat exchanger parameters in order to obtain a system with higher performance.

2.4. Heat Exchangers Used in Cryocoolers

The heat exchangers can be divided into two categories in general: regenerative heat exchangers and recuperative heat exchangers [29]. This division is mainly based on the fluid flow characteristic of the heat exchanger. However, many other properties of the heat exchanger also change due to this classification; such as geometry, working fluids, materials, etc.

2.4.1. Regenerative Heat Exchangers

In regenerative heat exchangers, there is an oscillatory fluid flow instead of a continuous flow. The fluid flows between two chambers, through the heat exchanger with a change in flow direction. The fluid temperature also varies with the flow direction so that it is high when it flows from the hot chamber to the cold chamber, and low when the flow direction is reversed. The heat exchanger, which is called the regenerator is a matrix type material with a high surface area to volume ratio. The regenerator absorbs heat while the fluid temperature is high and rejects this heat to the return flow, when the fluid temperature is low. Both the high and low temperature flows occupy the same space at different time intervals. The cryogen used in the regenerative heat exchangers is helium in most of the applications [23]. This is because of the low molecular weight of helium, which brings many advantages when the transport properties (density, viscosity, thermal conductivity and specific heat) are considered. The cooling capacity to work input ratio (i.e. system efficiency) is higher if the molecular weight is small [30]. Some examples of cryocoolers that runs with the regenerative heat exchangers are Stirling, Vuilleumier, Gifford McMahon, Solvay, pulse-tube cryocoolers [17].

2.4.2. Recuperative Heat Exchangers

In recuperative heat exchangers, there are two continuous fluid flows which are physically separated by a wall. High temperature gas (with ambient temperature at the inlet) flows from the hot chamber to the cold chamber through the heat exchanger. The fluid reaches cryogenic temperature at the cold chamber through an expansion process. After extracting heat from the target body at cryogenic temperature, the cold return gas flows through the heat exchanger in counter/cross flow configuration with the inlet flow. The returning flow extracts heat from the inlet flow by convection heat transfer through the separating wall between two flows. Some examples of cryocoolers that runs with recuperative heat exchangers are Joule-Thomson cryocoolers, Brayton cryocoolers [23], Collins helium liquefaction system [3], etc.

2.4.3. A Critical Assessment of Regenerative and Recuperative Heat Exchangers

In regenerative heat exchangers, as both hot and cold fluid flow through the same channel, the structure of the heat exchangers is simpler than the recuperative heat exchangers [17]. However, when a temperature below 50 K is required; the change of the heat capacity of the matrix material with temperature needs to be considered. The heat capacity of most of the materials used in the regenerative heat exchangers decreases below the heat capacity of the working fluid (generally helium) at around 10 K [23]. As a result, the heat exchanger needs to be more complex with several stages [17]. For a Gifford McMahon cryocooler to cool down to 4.2 K, a staged regenerator is used where copper screens, lead spheres and rare earth materials are used in different stages [31]. For the selection of regenerator material, the heat capacity at different working temperatures is crucial where for the recuperative heat exchangers, the thermal conductivity of the wall material is the important parameter.

In some of the cryocoolers operating with regenerators, valves are being used to obtain steady high pressure [23]. However, use of these valves decreases the reliability (and

therefore total life time) of the system, which is not suitable to some of the applications (such as the space applications).

The Cryocoolers with regenerative heat exchangers have higher cryocooler efficiency (in terms of work input and heat removal) than the cryocoolers with recuperative heat exchangers. Due to their comparatively lower efficiencies, higher working pressures are required for the cryocoolers with recuperative heat exchangers which may be around 200 to 250 bar in some applications, or even can go to 600 to 700 bar for a heat exchanger with low effectiveness [32]. Hence, as a drawback, multiple stage compressors are required in the recuperative heat exchangers. For a compressor, the compression efficiency decreases at high pressures [33].

On the other hand, the cryocoolers with recuperative heat exchangers are superior when vibrations in the system must be eliminated and refrigerant transportation is required [34]. In recuperative heat exchangers, the flow of the hot and cold fluids is not oscillatory as in regenerative heat exchangers, therefore the working temperatures are steadier in the recuperative heat exchangers [23]. Another advantage of steady fluid flow is that it allows distribution of the fluid to different locations at the same time which may be far away from the pressure source [33] using a distribution line. For the regenerators, the distribution line is essentially an additional volume increasing the dead space which also needs to be pressurized, therefore an increase of input power. As the target object can be placed far away from the pressure source, the system to be cooled can be isolated from the vibration effect of pressurization through compressors [33]. Moreover, as far as the cryocooler can be miniaturized, the dimension of the cooler may have little impact on the total system dimensions as the cooler and the pressure source can be separated [9].

The cryocoolers with regenerative heat exchangers are mostly preferred in applications where the cooling requirement is lower [35]. The cryocoolers with recuperative heat exchangers on the other hand are preferred when lower cool down times are needed which may be around 2-5 seconds, where cool down times for the

15

cryocoolers with regenerative heat exchangers are in the order of minutes [9]. The cryocoolers with recuperative heat exchangers are mostly fed with coolant from a pressure vessel and the return gas is exhausted to the atmosphere. The operation time of the system is limited with the volume of the pressure vessel. When long or unlimited operation is required, the cryocoolers with regenerative heat exchangers may be preferred or the cryocoolers with recuperative heat exchangers may be operated in closed cycle.

In some applications, cascaded systems may be required when the application requires advantages of both types of heat exchangers. An example of such a system is the Polatron receiver which is built to detect the cosmic microwave background of Big Bang [36]. This device is designed to be placed in South Pole; it requires a totally motorized operation without an operator. As very low wavelengths are required to be detected, the detector needs to be cooled to very low temperatures. The system is expected to function for very long times, therefore a closed cycle operation is required with high efficiency and high reliability. For this application, a closed cycle regenerative Gifford McMahon cryocooler is developed to cool helium below its inversion temperature, which is frequently used in the ground-based astronomical observations. As a second stage, the cooled helium is expanded within a recuperative Joule-Thomson cryocooler and liquefies at 4.2 K. This liquid helium is cooled further to about 0.3 K through a sorption cooler and liquid helium at 0.3 K is used to cool the detector material [36].

2.4.4. Types of Recuperative Heat Exchangers

The recuperative heat exchangers can be divided into two according to the shape of the heat exchanger: tubular heat exchangers and plate heat exchangers [25].

2.4.4.1. Plate Heat Exchangers

The plate heat exchangers used in the cryogenic systems are mostly plate-fin heat exchangers or perforated plate heat exchangers. These heat exchangers are used when there is too little space available.

In the plate-fin heat exchangers, a thin metal sheet is bent and brazed to two flat plates, forming small channels. The number and geometry of these channels are designed according to the system requirements to achieve the desired flow passages. The flow may be directed to different channels in order to achieve cross flow, counter flow or multi-pass flow heat exchanger.

The plate-fin heat exchangers have larger surface area to volume ratio than the tubular heat exchangers [35] and have a more compact structure compared with the tubular heat exchangers. This compactness also results in lower weight heat exchangers, which may be an important issue in applications such as high temperature superconductor (HTS) wind turbine generators, using helium as working fluid [35]. However, if the temperature required is low, this compactness becomes a drawback as it increases the heat loss through axial conduction. Another important disadvantage of the plate heat exchanger is that as the heat exchanger has small-diameter channels for compactness, the pressure drop across the heat exchanger is large [35]. As the plate fin heat exchangers are joined (brazed or welded), they are not suitable for high pressure applications [35]. It is noted that for the aluminum brazed plate fin heat exchanger, the maximum allowable working pressure is 110 bar [35] where in JT coolers, pressures up to 600 bar may be needed.

In the perforated plate heat exchangers, the perforated plates of high thermal conductivity are stacked. The holes of the plates form flow passages for the fluids. Low thermal conducting materials are placed between stacks to prevent axial conduction as well as provide leak tightness. As the channels formed by the holes on the plates are small (in the order of 0.3 – 1.0 mm diameter [37]), the total heat transfer surface area of the perforated plate heat exchangers is very high. As a result, the perforated plate heat exchangers are very compact. According to the design and working conditions, the perforated plate heat exchangers may be advantageous in high flow rate, low flow rate or low pressure drop applications [38]. Different types of the perforated plate heat exchangers working with nitrogen, neon, or helium are found in literature [38], with pressure reported up to 1150 bar [37]. Main applications of the

perforated plate heat exchangers are helium liquefiers, sorption refrigerators, cryoprobes and Kleemenko coolers running with gas mixtures [39]. Due to their compactness, both the perforated plate and the plate fin heat exchangers are suitable for applications where smaller volume is required. In the space applications or when liquid helium is required (4 K applications), the plate heat exchangers are used where high effectiveness (>95%), low axial conduction, low heat leak from environment are required. The perforated plate heat exchangers are superior to the plate-fin heat exchangers when high effectiveness values are concerned. Obtaining an effectiveness above 95% is difficult in the plate-fin heat exchangers where effectiveness of the perforated plate heat exchangers can easily be achieved ~99% [40].

2.4.4.2. Tubular Heat Exchangers

In the tubular heat exchangers, either one or both of the cold and hot fluids flows through the tubes. The tubular heat exchangers may be subcategorized as concentric tube heat exchangers (tube-in-tube) and coiled tube heat exchangers.

In the concentric tube heat exchangers, one of the fluids flows inside the inner tube while the other flows through the annular gap between the inner tube and the outer tube. In order to decrease the space occupied, the heat exchanger may be spirally (helically) wounded. Another additional advantage of wounding the tubes is induction of secondary flow, which increases the heat transfer through the heat exchanger [41]. Generally, the high temperature fluid flows from the inner tube while the low temperature fluid flows through the annular gap. Linde used this kind of simple tube-in-tube heat exchanger in liquefaction of air for the first time, in 1895 [25]. Helically coiled tube-in-tube heat exchangers have also been discussed to be used in the mixed refrigerant JT cryocoolers, for refrigeration and air conditioning, power engineering applications [42]. Another tube-in-tube helically coiled heat exchanger has been reported to be used in the helium purification system, with 200 bar inlet pressure [41]. In order to increase the mass flow rate of the high temperature fluid, several tubes instead of one may be placed inside the external tube. In order to generate turbulence

in the fluid flowing through the annulus, spirally wounded spacers between the inner tube and outer tube may be used. These spacers increase the heat transfer coefficient between the two flows. Another design alternative for the tube-in-tube heat exchangers is using a bundle of tubes instead of concentric tubes. High temperature fluid flows through the tube(s) at the core of the bundle while the low temperature fluid flows through the tubes at the outer tubes. The bundle is soldered so that the tubes are in good thermal contact with each other.

A special tube-in-tube heat exchanger designed to liquefy the helium is the Collins heat exchanger [17]. A schematic of the Collins heat exchanger is given in Figure 2.4. In this type of heat exchanger, the edge-wound copper helix is wrapped around the inner tube, at the annulus between the two tubes and soldered to both tubes. More than one level of tubes (tube with a diameter of d1 inside a tube with diameter of d2 inside a tube with diameter of d3, where d1<d2<d3, etc.) may be used in this design according to the requirements (pressure, volumetric flow rate, etc. of each channel) of the system. There are generally around 6 levels of heat exchangers [3]. An example system with the Collins heat exchanger may produce 25-32 l/hr of liquid helium with 45 kW power input, working at 12.5 atm pressure [17].
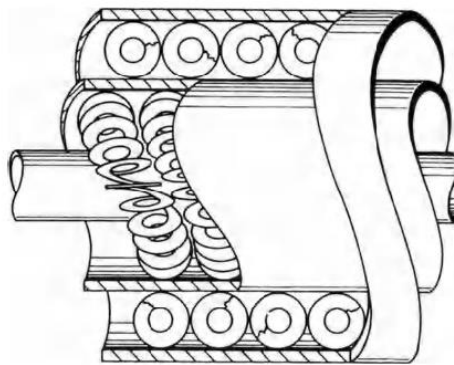
Figure 2.4. Schematic of the Collins heat exchangers [12]

In the coiled tube heat exchangers, a tube is wounded spirally around a mandrel and both are placed inside a shell. The high pressure fluid flows through the spirally wounded tube while the low pressure fluid flows through the annular space between the mandrel and shell, around the coiled tube. The coiled tube heat exchanger may be considered as a kind of shell and tube type heat exchanger. The high pressure gas flow may be considered as the tube side flow and the low pressure flow as the shell side flow. There may be more than one coiled tube in order to increase the mass flow rate of the tube side flow. An additional advantage of using multi-layer tubes is increasing the effectiveness of the heat exchanger [9]. In this case, it is important to keep the spacing between tubes constant to prevent escaping of the shell side flow through wider spacing. Thus, the shell side flow is forced to pass around each tube equally. The tubes may be finned in order to increase the heat transfer between two flows. A further improvement of the coiled tube heat exchangers is using a matrix material at the annular space instead of the fins around the tubes to increase the heat transfer surface area of the shell side flow.

A special design for the coiled tube heat exchangers is the Parkinson's heat exchanger [30]. This type of heat exchanger consists of a capillary coiled tube, whose central cylinder is wounded around a mandrel. This kind of heat exchangers is helically wounded twice; first with a small core diameter, then the core cylinder is wounded with a larger diameter. The Parkinson's heat exchanger was developed to liquefy hydrogen and helium gases [9]. It is reported that the advantages of the Parkinson's heat exchangers over traditional coiled tube heat exchangers (also known as the Giauque-Hampson type) is the simplicity of production. However, as the length of the high pressure tube increases, the pressure drop at the tube side flow also increases. In addition, due to the absence of fins at the shell side flow, the pressure drop at the shell side decreases. Both of these effects decrease the effectiveness of the heat exchanger [43]. The Parkinson's heat exchanger design had been studied by Air Liquide Company. The researchers used this design to develop flat JT coolers which may be used when the shape of the cryocooler cannot be cylindrical [44].

The coiled tube heat exchangers are preferred in areas where high pressures are required. They are also used in applications where large number of transfer units is needed at low temperatures [24], when there is high temperature difference [45]. There are many studies in the literature stating that the helically coiled heat exchangers have favorable heat transfer characteristics compared with the straight heat exchangers [46]. The helical flow passage results in higher turbulence with the same amount of pressure drop compared with other heat exchangers [45]. Moreover, the helically coiled structure is reported to prevent problems occurring due to thermal shock and thermal expansion/contraction, which are seen in the cryogenic applications [45]. A temperature distribution from cryogenic temperature to room temperature occurs along the heat exchanger, therefore the helical structure may act as a spring to damp the thermal expansion/contraction of the heat exchanger. Moreover, it allows different amount of contraction/expansion along the length, as the coils are not joined physically along the length.

It is stated in the literature that the circulation of the shell side flow is better in the wounded tube-in-tube heat exchangers than in the coiled tube heat exchangers [47]. However, the coiled tube heat exchangers can be insulated with vacuum in radial direction due to the design of the heat exchanger [48]. The tube-in-tube heat exchangers are either reported to be used in systems where they are placed inside a cryostat [41], or they are designed integrated with the system [9]. Although designing the cryocooler integrated into the system may result in a simpler configuration [9], it prevents interchangeability of the cooler. The coolers are needed to be interchangeable, due to their high failure rate because of the impurities inside the gas flow [49]. An interchangeable heat exchanger with vacuum insulation and simple integration cannot be achieved by tube-in-tube heat exchanger, in contrast with the coiled tube heat exchanger.

In JT cryocoolers, mostly tubular heat exchangers are preferred, as the working pressure needs to be high for the liquefaction of the working fluid. The heat transfer inside the tubes is enhanced due to the secondary flows generated inside the helical

21

capillary. In order to increase the heat transfer rate outside the tubes, the fins are used. As a result, shorter heat exchangers with same effectiveness can be obtained. Both the tube-in-tube and the coiled tube heat exchangers are found to be used in JT cryocoolers. The tube-in-tube heat exchangers are mostly found to be used in the helium liquefaction systems (4 K systems). The coiled tube heat exchangers are mostly found in applications where nitrogen or argon is used as the working fluid. IR imaging applications requires decoupling of the cooler and the detector. As also stated above, JT cryocoolers with the coiled tube heat exchangers are better suited for such applications.

2.5. Joule-Thomson Cryocooler

JT cryocooler is a special kind of cryocooler that makes use of JT expansion concept to reach cryogenic temperatures. The details of JT effect, subcomponents and geometry of a JT cooler and JT cycle are described in the following sections. A solid model of a JT cryocooler can be seen in Figure 2.5.
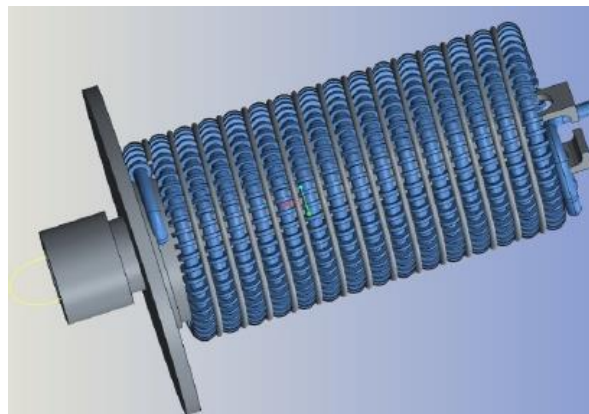
Figure 2.5. A 3D solid model of a JT cryocooler

2.5.1. Joule-Thomson Effect of Real Gases

Ideal gas law states that enthalpy of a gas is only a function of its temperature. For real gases on the other hand, enthalpy is a function of both temperature and pressure. A

change in the pressure of a gas may result in a change of the temperature at isenthalpic conditions. This phenomenon is called as the JT effect. The amount of temperature change due to pressure change is determined by the JT coefficient ($\mu_{JT} = \partial T / \partial P_h$) of the gas [50]. The JT coefficient of argon may be seen in Figure 2.6 on a temperature-entropy diagram, along constant enthalpy lines. A positive JT coefficient indicates that a decrease in pressure of the fluid results in a decrease of the temperature. In order to cool a gas with JT expansion, the JT coefficient of the gas should have a positive value.
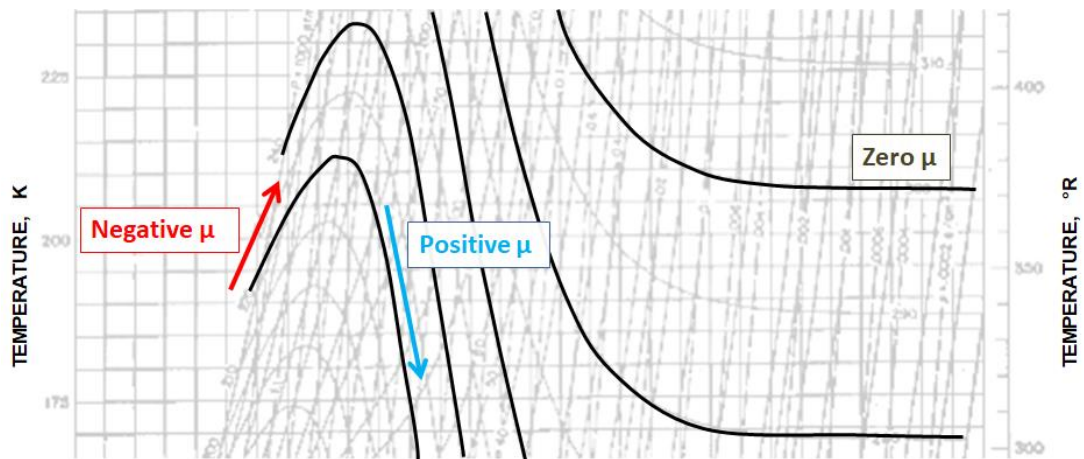
Figure 2.6. Temperature – entropy graph of argon gas [51]. JT coefficient of argon gas shown on constant enthalpy lines (black)

The value and sign of the JT coefficient depends on the temperature and pressure of the gas. The change of the JT coefficient of nitrogen gas may be seen in Figure 2.7. The states at which the JT coefficient changes sign is shown with dots. The curve which passes through the dots is called as the inversion curve. The JT coefficient of the gas is positive at the left side of this curve and negative elsewhere. The intersection of the inversion curve with the vertical (temperature) axis (point A) is called the maximum inversion temperature [52]. The JT coefficient of the gas above the

maximum inversion temperature is always negative. Below the maximum inversion temperature, the sign of the JT coefficient depends on pressure.
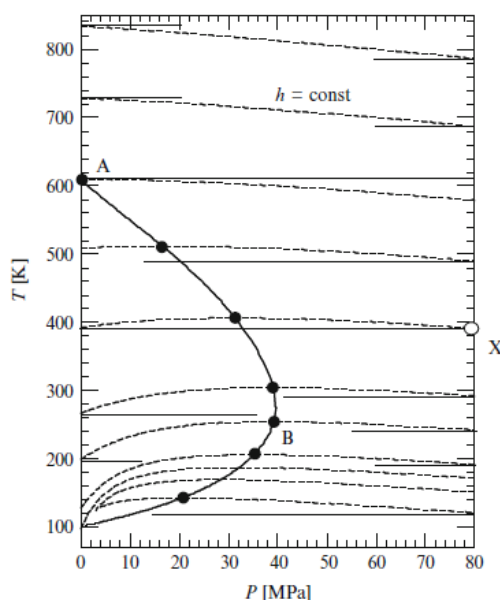
Figure 2.7. Temperature – pressure diagram of the nitrogen gas [9]

The maximum inversion temperatures and boiling points of some gases used in cryogenic applications may be seen in Table 2.1. Within these fluids hydrogen, helium and neon have maximum inversion temperatures below the room temperature. In order to use one of these cryogens within a JT cryocooler, a pre-cooling of the fluid is needed until the fluid temperature is decreased below the maximum inversion temperature. Nitrogen, argon, krypton, oxygen and hydrocarbons have positive JT coefficients at room temperature [53]. At atmospheric pressure, the lowest boiling points within these gases belong to the nitrogen (77 K) followed by the argon (87 K). These two gases are the most preferred working gases in the JT cooler applications. In order to achieve high cooling power, argon and nitrogen require a high inlet pressure, varying between 120 bar to 700 bar [11, 54, 55]. To decrease the required inlet pressure and increase the cooling power at the same time, gas mixtures (nitrogen,

argon, neon, hydrocarbons, etc.) are also used in some applications [5]. It is seen that the inlet pressure can be decreased down to 12-15 bar, in exchange of higher working temperature (100-120 K) [5].

Table 2.1. *Maximum inversion temperatures and boiling temperatures at 1 atm pressure of some common cryogens used in JT coolers [17]*

Fluid	Max. Inv. Temp. [K]	Boiling Temp. [K]
Helium	45	4.21
Hydrogen	205	20.27
Neon	250	27.09
Nitrogen	621	77.36
Air	603	78.80
Argon	794	87.28

Alternative to the isenthalpic expansion process, some other processes are also used in cryocoolers. In reverse Brayton cryocoolers, a continuous isentropic expansion takes place where the expansion takes place through a loaded turbine with extraction of work [9]. Isentropic expansion is also used in regenerative cryocoolers, where the flow rate, and therefore the expansion process is oscillatory with time. Stirling, Solvay and Vuilleumier cryocoolers are examples of coolers which uses oscillatory isentropic expansions with work extraction. [9]

2.5.2. Geometry of The Joule-Thomson Cryocooler

JT cryocoolers consists of mainly two functional components: a heat exchanger and an expansion valve (orifice). Different types of heat exchangers are used in the JT coolers, according to the application. Some of these are tube-in-tube helically wounded heat exchangers, coiled tube heat exchangers (Giauque-Hampson type heat exchangers), perforated plate heat exchangers or MEMS (also called as printed circuit or micro miniature) heat exchangers [9]. The heat exchanger of Gifford McMahon –

JT cooler system for refrigeration at 4.2 K is spirally wounded heat exchanger with high pressure helium as the working fluid [35]. The MEMS cryocoolers are developed by W.A. Little. In this heat exchanger, the channels, expansion orifice and cold chamber are all formed on planar glass substrates with photolithography and etching methods [34]. Due to the heat capacity of glass, this kind of cryocoolers does not have the fast cooldown characteristic [34]. They are mostly used in laboratory applications. In some JT cryocoolers, a flow regulation mechanism is also used which is designed to decrease the cool down time.

The heat exchanger of JT coolers used in SWIR, LWIR thermal detectors are mostly coiled tube heat exchangers (Giauque-Hampson type). Different geometrical designs of the coiled tube heat exchangers for JT cryocoolers are found in literature such as cylindrical, stepped cylinders (with a larger diameter at the entrance region and a smaller diameter close to the end), conical or flat (conical with 180° cone angle) heat exchangers.

The Giauque-Hampson type heat exchanger consists of a capillary tube, which is helically wounded around a cylindrical mandrel. In order to increase the heat transfer rate of the shell side, the capillary tube is finned in radial direction. The sum of the fin thickness and the gap between two fins is called as the fin pitch. The helical capillary together with the mandrel is placed inside a cylindrical shield. The mandrel and shield form the framework of the cryocooler. The orifice is placed at the end of the heat exchanger. The finned capillary is connected to the orifice. The space between orifice and target body is called as cold chamber. A cross sectional view of a JT cooler working in open cycle can be seen in Figure 2.8.
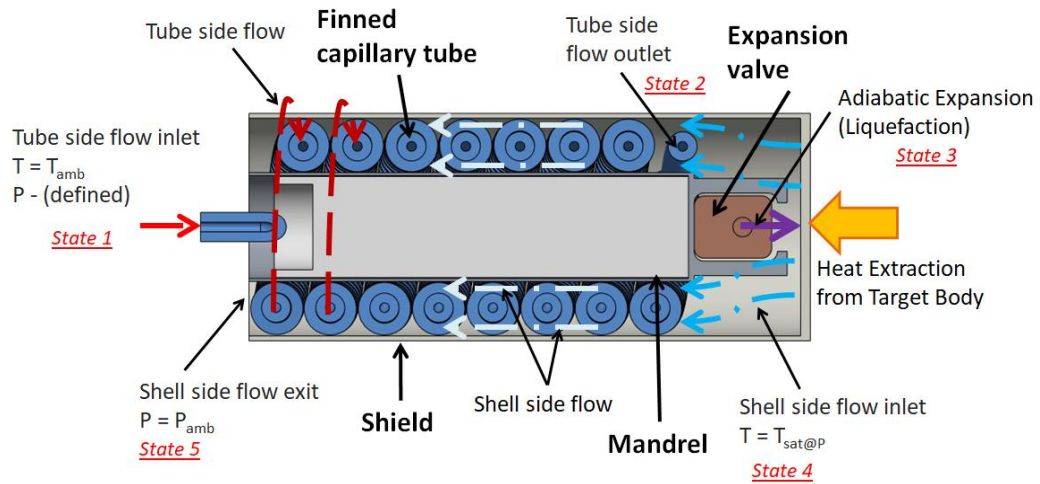
Figure 2.8. Sectional view of JT heat exchanger along the axial direction – not to scale

For cryocoolers with flow regulation, the regulator mechanism is mounted inside the mandrel. As the capillary tube is wounded around the mandrel, the length of the mandrel is equal to the total length of the heat exchanger. The mandrel is a closed body, the shell side flow does not pass through the mandrel. Inside of the mandrel is thermally insulated. The shield is a part of the framework which carries the target body to be cooled (i.e. IR sensor). The shield is covered with an external cylinder, which is the detector body in the thermal cameras. The space between the shield and the detector body is vacuumed, so the external surface of the shield is thermally insulated.

2.5.3. Joule-Thomson Cycle

The Joule-Thomson cycle is one of the mostly used refrigeration cycles in the cryogenic systems. The definition of each state of the cycle can be seen in Figure 2.8. A simplified representation of the cycle showing the heat interactions and the gas flow directions can be seen in Figure 2.9. The high pressure working gas at room temperature enters the inlet of the finned capillary, which is state 1. It flows helically inside the capillary and called as tube side flow. At the exit of the capillary which is the state 2, it expands isenthalpically through the orifice to a lower pressure. The pressure decrease at constant enthalpy results in a temperature decrease. The gas is at

27

state 3 after the isenthalpic expansion. The low pressure, low temperature gas enters the heat exchanger through the annulus between the mandrel and the shield. The low pressure gas flow is called as the shell side flow. Inlet of the shell side flow is state 4. It flows in counter/cross direction with the tube side flow, around the finned capillary, between the fins and cools the tube side flow. The exit of the shell side flow is state 5. When steady state condition is reached, some portion of the cryogen after isenthalpic expansion through the orifice (state 3) liquefies. This liquid cryogen extracts heat from the target body which needs to be cooled. The amount of liquid formed (i.e. the enthalpy difference between states 3 and 4) determines the cooling power (Q) of the cryocooler. Chua [66] discussed that the gas is at saturated vapor state at shell side flow inlet (state 4).
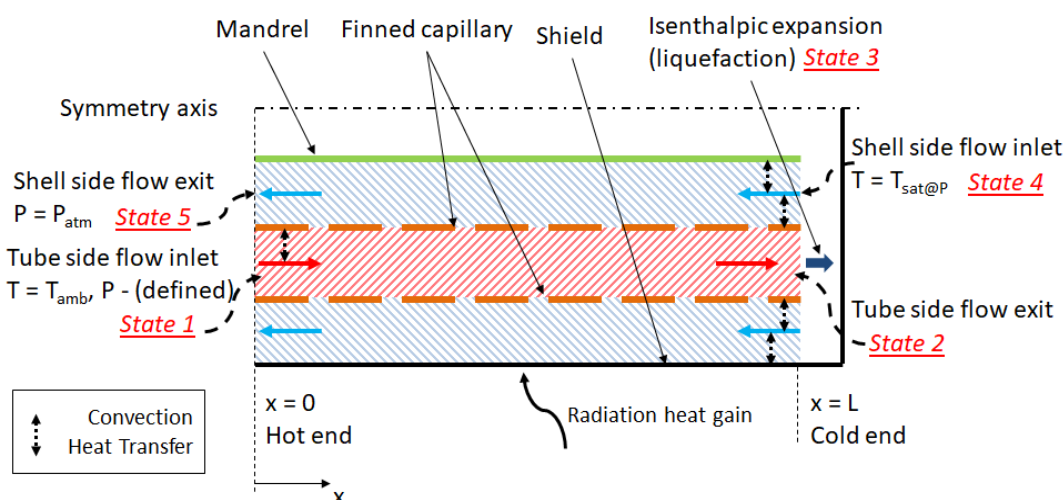
Figure 2.9. Schematic representation of the Joule-Thomson cycle, with fluid flow paths and heat interactions within the heat exchanger

The JT coolers can be used in closed or open cycle configuration. In open cycle configuration, the exit of the shell side flow is exhausted to the atmosphere, as shown in Figure 2.8 and Figure 2.9. In closed cycle configuration, the exhaust gas is fed to a compressor where it is pressurized and fed back to the inlet of the heat exchanger.

2.5.4. Advantages of Joule-Thomson Cryocooler over Other Cryocooler Types

JT coolers have many important advantages over other types of cryocoolers. First of all, the most distinct advantage is low cool down time. Second, JT coolers may be designed without any moving parts [23]. As material abrasion is much lower for the heat exchangers without any moving parts, the lifetime and reliability of JT coolers are higher. Having no moving parts at the cold end is especially important, which is an advantage of JT cooler over some of the other cryocoolers operating with a recuperative heat exchanger, such as Brayton cooler. Eliminating moving parts also prevents mechanical vibrations, which is an important parameter in an imaging system. Due to the simplicity of the geometry and the working conditions, JT cryocoolers can be miniaturized and can be used in applications where small size and weight are required.

As the cryogen is liquefied at the cold end, the cooling of the target body is achieved by phase change in JT coolers. This is an important advantage of JT coolers over other types of cryocoolers where cooling is achieved by the sensible heat of the working fluid [9]. When single component pure refrigerants are used as cryogen, the temperature distribution over the target cooled object is homogeneous and do not vary with time. This may be crucial in some applications such as IR imaging, where the temperature variation of the sensor with time causes noise on the signal generated. In addition, inhomogeneous temperature distribution along the sensor surface results in a distortion of the IR image formed on the screen. The temperature of the sensor affects the NETD stability of the sensor [36]. A Joule-Thomson cryocooler may achieve 0.1 K temperature stability [8]. Moreover, due to the phase change, the heat flux is higher.

Finally, JT cryocoolers allow operation at open cycle, which decouples the cryocooler and the gas source. The gas may be supplied from a constant volume gas source, eliminating the requirement of a compressor at the inlet. Open cycle operation also eliminates the heat rejection from the working fluid to the ambient at hot end, resulting

in a simpler design. Therefore, for a specified heat transfer requirement, either the cryocooler or the heat exchanger may be made smaller in size [9].

JT coolers also have some drawbacks compared with other cryocoolers. The main disadvantage is the requirement of high purity of the working gas [49]. Impurities of the working gas results in malfunction of the orifice and may result in failure of the cooler. Second, the thermodynamic efficiency is lower for JT coolers. For an application where more than one cryocooler can be preferred, cost of operating a JT cooler may be higher than other types. Finally, JT coolers need high inlet pressure. Compressor efficiency decreases at higher pressures. In addition, the liquefaction is not achieved when inlet pressure decreases below a certain value. For an open cycle system, the gas vessel size and pressure should be higher than the total amount of gas which is used during operation.

2.5.5. Numerical Studies on Joule-Thomson Cryocoolers

There are many numerical studies reported in the literature analyzing the performance of a JT cryocooler. Several researchers have studied modeling of JT coefficient using different real gas models and determining temperature of the gas after expansion [50, 52, 56-59]. The first numerical model which focuses on modeling fluid flow and heat transfer of a JT cryocooler is built by Chou et al. [54]. They built a 1D, transient model of the cryocooler without any flow regulation. For heat transfer and friction coefficients, they used correlations suggested in the literature. The study also includes an experimental part to determine the cool down times of the cryocooler. The cool down times found from the numerical model are compared with experimental values. This study is further extended by Chien et al. by including the model of the flow regulation mechanism [60], and considering the vapor-liquid two phase coexistence of the gas within this mechanism [61].

Gupta and Atrey [62] built a numerical model of a JT cooler with a tube-in-tube type heat exchanger, which is used for liquefaction of the helium gas. The effects of heat leaks and axial conduction on the performance of the heat exchanger are studied. It is

concluded that as the working temperature decreases, the heat leaks increase, so they cannot be neglected when building a numerical model. In later studies, Gupta et al. analyzed the heat transfer coefficient [63] and the friction coefficient [64] correlations for the Helium liquefaction systems. They also performed experimental studies to validate their numerical models.

Xue et al. [65] built a 1D numerical model to study the steady state performance and losses of a cooler working with argon gas, in comparison with the experimental results. The shell side exit temperature calculated from the model and measured in the experiments are compared to validate the numerical model. It is found that increasing the inlet pressure decreases the effectiveness of the heat exchanger and increases availability losses of the heat exchanger. Ng et al. [11] further detailed the modeling of the thermo-physical properties of the working gas and the thermal conductivities of solids. They presented the temperature and pressure distributions along the heat exchanger length. Three different cases are analyzed with different tube side inlet pressures. Chua et al. [66] further improved this study by building a 3D model of the geometry to calculate the geometric parameters. They suggested defining the shell side inlet temperature as saturation temperature at the given pressure and included the change of enthalpy with pressure in the conservation of energy equation. The entropy generation and jet impingement boiling equations are also introduced. The results of the numerical model are validated with the experimental results given by Ng et al. [11].

2.5.6. Optimization Studies on Joule-Thomson Cryocoolers

The JT coolers have extreme working conditions, such as very low (cryogenic) temperatures and very high pressures (150 – 800 bar [55]). In addition, most of their practical applications require small dimensions, low cool down times, high operation times and high cooling capacities. Therefore, it is important to optimize the dimensions and working conditions of JT coolers with respect to the requirements of the application. There are several studies in the literature which uses numerical models

to compare the effects of the design parameters on some performance parameters of the JT coolers.

The earliest study in the literature, which compares the effects of different parameters is performed by Maytal [67]. Similarity functions are built using physical relations, to study the cool down time of the JT cryocooler. The effects of temperature, pressure and kind (nitrogen and argon) of the inlet gas on the cool down time are studied. It is concluded that the argon gas has a faster cool down characteristic compared with the nitrogen gas. Moreover, with argon gas the liquefaction may be achieved even when the temperature of the working fluid is still high, before the expansion. As a result, the size of the cryocooler can be smaller when operated with argon (in expense of the heat exchanger effectiveness). Maytal [68] further studied the effect of inlet pressure and kind of gas used (argon or nitrogen) on Q and the operation time for a JT cooler with constant dimensions, fed from a constant volume gas source. Through a thermodynamic analysis, he showed that Q increases with increasing inlet pressure. For different gases the peak occurs at different pressures (around 400 bar for nitrogen and 500 bar for argon). Moreover, argon has longer operation time than nitrogen when both are fed from a constant volume vessel with the same initial pressure. Thirdly, he studied the effects of inlet pressure, mass flow rate and length of the heat exchanger on Q and compactness of a JT cooler [55]. He did not build a physical model of the heat exchanger but analyzed the states of the cycle for an ideal cooler neglecting the conduction losses, friction losses and property variations along the heat exchanger. Similarity functions for the cooling power and compactness are defined. An optimization study has been performed by differentiating the similarity functions with the parameters to be optimized. The optimum values of the design parameters have been found to maximize the cooling power and the compactness. It is concluded that the highest cooling power is reached at lower heat exchanger efficiency values. An optimization study to maximize the heat exchanger efficiency or minimize the entropy generation does not result in maximum cooling power of the cryocooler.

Hong et al. [69] performed an experimental study to analyze the effect of inlet pressure and volume of the gas vessel on the cooldown time and the total gas consumption during cooldown. They found that because of the gas consumption during operation, vessels below a certain volume may fail to cool the target body. In a further study, they built a numerical model of JT cooler using the effectiveness-NTU method and studied the effects of the mass flow rate and the inlet pressure on the effectiveness and the cooling power of argon and nitrogen [70]. Through a similar study, they built a numerical model using Navier-Stokes equations together with heat transfer and friction correlations [71]. Using the model, the effect of inlet pressure and vessel volume on the cooldown time, gas consumption during cooldown and the pressure drop during operation for nitrogen and argon gases are studied. It is found that the inlet pressure does not affect the cool down time, however the inlet pressure and/or vessel volume should be above certain limits for cooling the target body. In their most recent study, Hong et al. [48] studied the effect of three different heat exchanger configuration on the cooler performance. The effectiveness-NTU method is applied. It is found that increasing the number of wraps (total length of the heat exchanger) increases the cooling power. For low cool down time, a configuration with two parallel tubes is more advantageous.

Gupta et al. [4] studied the effect of irriversibilities such as heat-in-leaks, longitudinal heat conduction through the separating wall of heat exchanger and the conduction through high temperature connecting tubes, on the performance of the tube-in-tube heat exchanger of a helium liquefaction system. A numerical model is built using Navier-Stokes equations and the effectiveness-NTU method. A second law analysis has been conducted in order to study the irriversibilities.

Tzabar et al. [72] have performed an experimental study together with a numerical model in order to determine the effect of krypton precooling and the mass flow rate on the cooldown time for a JT cooler working with pure argon gas. It is found that lower mass flow rates of argon can be used with precooling with krypton and lower cool down times can be achieved. However, if the total space available for the gas

vessels is constant, an additional krypton source causes lower operation time. In a recent study, Tzabar and Kaplansky [2] built a numerical model to analyze the cooldown of a detector-dewar-cooler assembly and performed an experimental study to validate the numerical model. The effect of different ambient temperatures, mass flow rates and vessel volumes on the cooldown periods are presented for argon gas with constant initial pressure.

Ardhapurkar and Atrey [73] built a 1D model to study the steady state characteristics of a JT cooler. Navier-Stokes equations together with heat transfer and friction correlations are solved. The thermo-physical properties of the working gas are extracted from a commercial software. The results are compared with the results presented by Ng et al. [11]. An area correction factor is suggested for the heat transfer area of the shell side flow, based on the differences with the reference study. The effects of working conditions, such as the inlet pressure and kind of the working fluid (nitrogen and argon) and design parameters, such as the mass flow rate, fin density, helical diameter and length of the heat exchanger on the total pressure drop, the effectiveness of the heat exchanger and the cooling power of the cooler are analyzed. Conclusions are derived through comparison of the graphs. Damle and Atrey [32] further improved the study by modeling the transient cooldown period of the JT cooler and included distributed JT effect throughout the heat exchanger. The inclusion of the distributed JT effect in comparison with the area correction factor suggested by Ardhapurkar and Atrey [73] are discussed. It is shown that higher tube side inlet pressure results in a lower cool down time. They further analyzed the effect of the vessel volume at constant pressure, and the vessel pressure at constant volume systems [10]. The effects of both parameter on the cooling power and the operation time are discussed through comparison of the graphs. It is concluded that for each pressure, when the reservoir capacity is below a limit, liquid cryogen temperature is not achieved. As a result, the cooler fails to cool the target down to the specified working temperature. When higher cooling power is required, the vessel pressure needs to be increased.

34

Liu et al. [74] performed an optimization study in order to minimize the entropy generation throughout a JT cooler. A numerical model is built solving Navier-Stokes equations together with the heat transfer and friction correlations. The numerical model is validated through results presented by Ng et al. [11]. The availability losses of JT cooler are calculated as the summation of the heat transfer losses and frictional losses. The minimum value of the total availability loss is determined with respect to the tube diameter, total length of the heat exchanger, fin density and shell diameter. The response surface methodology is used in order to determine the combined effect of all parameters on total availability loss and the optimum values of each parameter is determined.

2.5.7. A Critical Assessment of The Literature

There are some approaches and assumptions found in the literature for modeling the JT coolers, which need questioning and further improvement. First of all, there are some differences in modeling the momentum equation and the friction correlation used for the tube side pressure drop, which is also discussed by Can et al. [75]. Chou et al. [54] modeled the momentum equation using Darcy friction equation and derived the friction correlation from Timmerhaus and Flynn [12] accordingly. A similar approach is also used in some other studies [64, 70, 75]. On the other hand, it is seen that in several studies [10, 11, 32, 65, 66, 73, 74], even though the momentum equation is formed using the Fanning friction equation, the same friction correlation given by Chou et al. [54] is used. The coefficient of the friction correlation is four times larger in these studies, which causes severe differences in the results obtained.

Second, in most of the previous studies [11, 54, 65, 71, 73], the enthalpy is considered as a function of temperature at constant pressure, which is the ideal gas assumption. However, the gases used in JT cryocoolers cannot be considered as ideal gases, as ideal gas assumption neglects the change of temperature with pressure at constant enthalpy (the JT effect). In a real application, the temperature of argon gas which is initially at around 255 K and 500 bar, is below 135 K after isenthalpic expansion (JT

expansion) to 1 atm. The enthalpy should be equated as a function of both temperature and pressure in the conservation of energy equation, which is considered in some of the studies [10, 32, 55, 66].

The pressure drop calculation of the shell side flow is not presented in some of the studies [11, 54, 55, 65, 67, 68]. Assuming constant pressure at every node and not updating it using Navier-Stokes equations results in an error. In some of the studies, straight channel internal flow correlation is used for the shell side friction factor [10, 32, 66, 74]. The shell side flow is a highly complex flow, due to the geometry of the shell side of the heat exchanger. Assuming straight channels is an over-simplification and results in a lower pressure drop than expected. Moreover, the inconsistency of the momentum equation and the friction correlation discussed earlier for tube side flow correlation is also present for the friction correlation of shell side flow used in some of the studies [66, 74]. The coefficient of friction correlation given in these studies is four times larger than expected.

The calculation of the shell side cross section area is not clearly mentioned in most of the studies [11, 32, 54, 65, 70, 74]. Ardhapurkar and Atrey suggested using the projected area method [73]. Gupta et al. [63] stated that the free volume concept is better suited when the correlations given in Timmerhaus and Flynn [12] is used.

The inlet conditions of the shell side are measured in some studies [11, 54] and these measured values are used as boundary conditions [10, 11, 32, 65, 73, 74]. The measurements are done for certain geometries and working conditions. The boundary conditions are kept constant when the geometries and the working conditions are varied. This approach is not applicable as the inlet conditions of the shell side are subject to change for different geometries and working conditions. To be able to define the shell side flow inlet conditions in an optimization study, measured values at every different studied case are needed, which is practically not possible. Therefore, better definitions of the boundary conditions for the shell side flow are needed.

The radiation heat transfer occurs between the shield, whose temperature decreases down to the cryogenic temperatures, and the external cylinder covering the shield, whose temperature is always at the room temperature. In some earlier studies, this radiation was not considered [54]. In other studies [10, 32, 60, 66, 73] it is taken as a constant value. However, Woods et al. [76] showed that the emissivity of stainless steel changes considerably from room temperature to cryogenic temperatures. Assuming constant emissivity results in an error at the calculated radiation heat transfer. The emissivity should to be defined as a function of temperature.

There are several studies which analyzes the effects of the design parameters on some objectives [2, 10, 32, 60, 65, 66, 69, 70, 73]. Most of these studies only discusses the results obtained from the graphs, without following an optimization method. The effect of every design parameter on each objective is analyzed individually, without considering the combined effects. These studies do not suggest a different geometry or working conditions based on the presented results. In some earlier studies [55, 67, 68], Maytal formed similarity functions which he used for optimization purposes. However, simplified models are built in these studies where many important parameters such as heat losses, pressure drops, variation of thermophysical and transport properties with temperature, etc. are neglected.

The only study which incorporates an optimization method, known to the author of this study, is done by Liu et al. [74]. They used the response surface methodology to minimize the entropy generation within the system. However, Maytal suggested that the main objective of a JT cooler is to extract heat from a target body, therefore maximization of the cooling power is more important than minimization of the entropy generation [55]. He presented that higher cooling power values can be obtained with lower efficiency systems. Moreover, the selection criteria of the design parameters are not given. The fin parameters such as fin length and fin thickness are not considered. The helical diameter is analyzed in the optimization, where helical diameter is a function of the shell diameter which is determined by the dimensions of the target

body to be cooled. Therefore, an increase or decrease of the helical diameter cannot be considered when the application of the cooler is considered.

In the current study, the improvements listed above are conducted. The pressure correlations of both tube side and shell side are reconsidered. The enthalpy is equated as a function of both temperature and pressure within the conservation of energy equations of the gases. The exhaust conditions of the shell side flow, which are known to be atmospheric, are defined instead of inlet conditions which are not known for every different case. The emissivity of the shield is defined as a function of temperature. Finally, an optimization study is performed in which the objectives are selected with respect to the application considered in the current study, which is the IR sensor cooling. The specific cooling power (q) is maximized, which effects the operation time of the sensor and the shell side pressure drop is minimized which determines the working temperature, therefore the noise signal generated for the sensor.

CHAPTER 3

NUMERICAL MODEL OF THE HEAT EXCHANGER

To analyze the heat exchanger of a JT cooler, a numerical model needs to be built which calculates the performance parameters. The model is built from the Navier-Stokes equations for fluid flows and energy equations for solids bodies. It is seen in the literature that mostly 1D models are used, where the heat transfer and friction coefficients are calculated from correlations. In the following sections, first the geometry of the JT cooler is defined. To obtain a 1D model, the differential forms of conservation of momentum and energy equations are needed to be simplified using a number of assumptions. In the second section, the validities of these assumptions are questioned. The geometry, materials, working conditions and states of the gas are taken from a reference study [11]. Non-dimensional parameters are calculated for validation of the assumptions which are used in simplifications. Once the simplifications are validated, a numerical model of the heat exchanger is built using the final forms of the differential equations. The solution algorithm is verified by comparing the results achieved by the current model with those given in the reference study. Then a number of improvements are suggested and their effects on the results are studied.

3.1. Definition of The Geometry

The details of the geometry are presented schematically in Figure 2.8. The tube side flow is flow inside a helical capillary, which has a constant cross section area. The shell side flow cross section area is the area between the mandrel and the shield at any cross section along the heat exchanger length, which is unoccupied by the finned capillary and the fins. A portion of the shell side flow cross section area is shown in Figure 3.1.
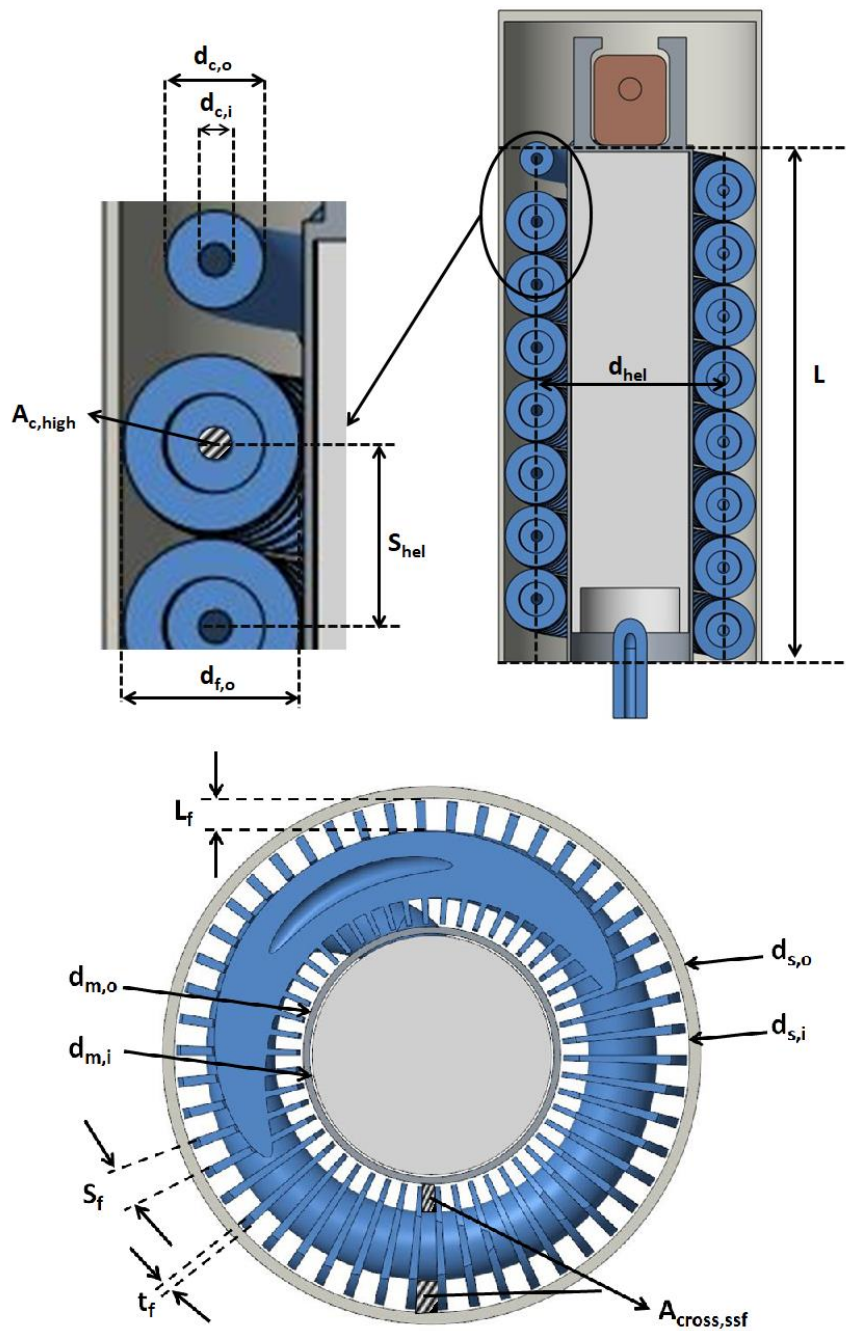
Figure 3.1. Dimensions of the JT cooler – not to scale

Total shell side flow area is the summation of the cross section areas between each two consecutive fins. The free volume concept, which is suggested by Gupta et al. [63], is used in the current study for the shell side flow cross section area. In the free

volume concept, the total free volume of the shell side flow is calculated by subtracting the space occupied by the capillary and the fins from the annulus between the mandrel and the shield. The Shell side cross section area is then calculated by dividing the total free volume to the length of the heat exchanger, as can be seen in Eqn. (1).

$$
\begin{aligned}
A_{cross,ssf} \\
= \left\{ \pi L \left(\frac{d_{s,i}^2}{4} - \frac{d_{m,o}^2}{4} \right) - \left[\pi L_c \frac{d_{c,o}^2}{4} + \pi t_f n_f \left(\frac{d_{f,o}^2}{4} - \frac{d_{c,o}^2}{4} \right) \right] \right\} / L
\end{aligned}
\tag{1}
$$

where $d_{s,i}$ is the inner diameter of the shield, $d_{m,o}$ is the outer diameter of the mandrel, L_c is the total length of the capillary, $d_{c,o}$ is the outer diameter of the capillary, t_f is the fin thickness, n_f is the number of fins, $d_{f,o}$ is the outer diameter of the fins, L is the length of the heat exchanger. The hydraulic diameter, which is required for calculations of shell side flow parameters, is calculated using:

$$
d_{hyd,ssf} = \frac{4 A_{cross,ssf}}{P_{w,ssf}}
\tag{2}
$$

where $P_{w,ssf}$ is the wetted perimeter of the shell side flow, which is the total wetted area divided by length, as given below.

$$
\begin{aligned}
P_{w,ssf} = \Bigg[\pi \, 2 \, n_f \left(\frac{d_{f,o}^2}{4} - \frac{d_{c,o}^2}{4} \right) + \pi \, d_{c,o} n_f (s_f - t_f) \\
+ L \left(\pi \, d_{s,i} - \pi t_f \frac{d_{hel}}{s_f} \right) + L \left(\pi \, d_{m,o} - \pi t_f \frac{d_{hel}}{s_f} \right) \Bigg] / L
\end{aligned}
\tag{3}
$$

where s_f is the helical pitch and d_{hel} is the helical diameter, which is the fictional diameter where the center of the finned capillary always lies on. Helical diameter is calculated as

$$d_{hel} = d_{m,o} + 2 \left(d_{c,o}/2 + L_f \right) \tag{4}$$

where L_f is the fin length. Number of fins, n_f, is the total number of fins along the finned capillary length, and can be calculated as

$$n_f = \frac{L_c}{s_f} \tag{5}$$

where, length of the finned capillary, L_c is calculated as

$$L_c = \left(\frac{L}{s_{hel}} \right) \sqrt{(\pi \, d_{hel})^2 + (s_{hel})^2} \tag{6}$$

where s_{hel} is the helical pitch. As the finned capillary is wounded without any gap between the helix, helical pitch is equal to the fin outer diameter, as can be seen from Figure 2.8. Helical pitch can be calculated as follows:

$$s_{hel} = d_{f,o} = d_{c,o} + 2 \, L_f \tag{7}$$

3.2. Validation of The Assumptions

To form a basis for the current study, the work of Ng et al. [11] is taken as a reference. The main reason for selecting this study is because the configuration suggested there is extensively used in the literature [10, 32, 73, 74] for verification and comparison purposes. Moreover, it is one of the few studies found in the literature presenting sufficient information, which are required to repeat the work done. Necessary information about geometry or working conditions are not presented in some of the studies. The details which are missing in the study of Ng et al. [11] are given in a subsequent study of the same working group [66]. In addition, even though the study

of Ng et al. [11] is basically a numerical study, there also exists some experimental data and comparison of numerical and experimental results.

The results presented in the study of Ng et al. [11] are only used to verify the solution algorithm. The verification is done by comparison of the temperature profiles found in the current study with those given by Ng et al. [11]. To obtain comparable results, equations and correlations given in the verification study are used while building the numerical model. Once the verification of the solution algorithm is finalized, the numerical model is improved by application of several modifications discussed in the current study.

The geometric parameters of the verification study may be seen in Table 3.1. Some of the geometric parameters which are not presented in the study of Ng et al. [11] (fin height, fin length, etc.) are taken from Chua et al. [66]. The hydraulic diameter calculated for the shell side flow using Eqn. (2) is 0.21 mm. The mass flow rate of the reference case is given as 13.93 SLPM, which corresponds to 0.395 g/s. Material of the finned capillary is copper, mandrel is monel and shield is stainless steel.

Table 3.1. *Heat exchanger dimensions of the reference study [11,66]*

Geometric Parameter	Abbreviation	Size
Length	L	50 [mm]
Finned capillary inside diameter	$d_{c,i}$	0.3 [mm]
Finned capillary outside diameter	$d_{c,o}$	0.5 [mm]
Fin thickness	t_f	0.1 [mm]
Fin length	L_f	0.25 [mm]
Mandrel inside diameter	$d_{m,i}$	2.3 [mm]
Mandrel outside diameter	$d_{m,o}$	2.5 [mm]
Shield inside diameter	$d_{s,i}$	4.5 [mm]
Shield outside diameter	$d_{s,o}$	4.8 [mm]
Helical pitch	s_{hel}	1 [mm]
External body diameter	d_{ext}	20 [mm]

Thermodynamic properties of the working fluid at each state according to the verification study is given in Table 3.2. State 3 is found from enthalpy of state 2 and pressure of state 4.

Table 3.2. *Thermophysical properties of the working fluid at each state for the verification study [11]*

Parameter	State 1	State 2	State 3	State 4	State 5
T [K]	291.5	187.5	110.4	110.4	282.6
P [bar]	179.1	67.06	1.73	1.73	1.55
ρ [kg/m^3]	314.42	232.68	-	7.76	2.64
μ [Pa.s] x 10^{-5}	2.92	1.95	-	0.91	2.16
c_p [kJ/kg.K]	0.76	1.08	-	0.57	0.52
k [W/m.K]	0.027	0.018	-	0.0072	0.017
Pr [-]	0.83	1.17	-	0.72	0.67
i [kJ/kg]	119.73	62.16	62.16	55.36	146.71
S [kJ/kg.K]	2.70	2.62	-	3.23	3.76

3.2.1. Validity of The Heat Transfer and Friction Correlations

To evaluate the validity of the heat transfer and friction coefficient correlations which are used, first the Reynolds number of the flows at each state are calculated. Reynolds number is calculated at both inlet and exit of the heat exchanger, because of high variations of the viscosity along the heat exchanger, due to large temperature differences. The tube side flow is an internal flow and $d_{c,i}$ is used for Reynolds number calculation. For the shell side flow, $d_{hyd,ssf}$ is used. The Reynolds numbers at each state may be found in Table 3.3.

Table 3.3. *Reynolds number of the flow at each state*

State number	Re
1	57356
2	85971
4	2496
5	1050

The correlations for the heat transfer and friction coefficients are taken from Timmerhaus and Flynn [12]. For the tube side flow, correlations suggested for the helix tubular pipes are used. The correlations are valid for gas flow without phase change, with Reynolds number > 10000. As can be seen from Table 3.3, the Reynolds number from state 1 to state 2 satisfies the requirement, therefore it is convenient to use the suggested correlations.

For the shell side flow, different correlations for the heat transfer and friction coefficient are used in the literature. In almost all of the studies, the heat transfer correlation suggested by Barron [17] for bank of inline tubes is used. When the sectional view along the heat exchanger length as given in Figure 2.8 is considered, it can be seen that the shell side flow area is similar to bank of inline tubes configuration with 1 tube in transverse direction and several tubes in longitudinal direction. The difference between the bank of inline tube geometry and the shell side geometry of JT cryocoolers is due to the radial fins of the capillary in JT coolers. However, effect of this difference between geometries is not discussed in the literature. Moreover, a more suitable correlation for the heat transfer coefficient of the shell side flow of a JT cryocooler is not suggested. Therefore, the correlation suggested for bank of inline tubes is used in the current study.

The correlation used for the friction coefficient of the shell side flow is not given in the reference study. In the later study [66], the straight tubular pipe correlation suggested by Timmerhaus and Flynn [12] is used. This correlation is not suitable for the current studied case. First, the geometry of the shell side flow is highly more complex compared with straight pipes. Unlike seen in Figure 3.1, the fins are not always aligned perfectly in the axial direction of the heat exchanger. The flow area at one helix may be followed by a fin at the consecutive helix. It is only possible to obtain perfectly aligned fins if the number of fins at one helix, i.e. the length of one helix divided by the helical pitch, is an integer. For the geometry analyzed in the current study, the number of fins per helix is calculated as 36.8, which means that the fins are not aligned along the heat exchanger length. Second, the validity range of the correlation is for Reynolds number larger than 10000, where according to the

verification study it varies from 2500 to 1000 in the shell side. A better correlation is suggested in the current study during the improvements done on the numerical model.

3.2.2. Analysis of Flow Development Lengths

In order to confirm that the flow is fully developed throughout the channel length, the developing length needs to be calculated. The tube side flow is turbulent at the entrance of the heat exchanger. For flow inside channels, the developing length calculation is given below for turbulent flows (Re > 2100) [77]:

$$L_e = 4.4 \, d_{c,i} \, Re^{1/6} \tag{8}$$

The entrance length of the tube side is calculated as 8.2 mm, where the total length of the finned capillary is 552 mm. The entrance length is less than 2% of the total length and can be neglected. The flow can be considered as fully developed and partial differential equations can be simplified accordingly. For the shell side, the flow of the gas around the finned capillary is studied. Therefore, the flow is considered as external flow and flow development is not analyzed.

3.2.3. Analysis of The Temperature Distribution of The Solid Bodies in Radial Direction

In order to comment whether it is required to calculate the temperature distribution of the solid bodies or they can be assumed lumped in the radial direction, the Biot Number needs to be calculated. Biot number is the ratio of the convection resistance to the conduction resistance. For a cylindrical system, conduction and convection resistances are defined as following [20]:

$$R_{cond} = \frac{\ln(d_{c,o}/d_{c,i})}{2 \, \pi \, k_{solid} \, L} \tag{9}$$

$$R_{conv} = \frac{1}{h \, A_w} = \frac{1}{h \, d_{c,i} \pi \, L} \tag{10}$$

Biot number is by definition R_{cond}/R_{conv}, therefore for the given case:

$$Bi = \frac{d_{c,i} \, h \, \ln(d_{c,o}/d_{c,i})}{2 \, k_{solid}} \tag{11}$$

A solid body may be assumed lumped in the radial direction if the Biot number is smaller than 0.1. In order to calculate the conduction resistances, the temperature dependent thermal conductivities of the solid bodies are calculated. For this purpose, the equations given in [11] are used. The finned capillary tube material is copper, the mandrel is monel and the shield is stainless steel for the reference case. The conductivities of these material are given in Table 3.4 as a function of temperature, in Kelvin.

Table 3.4. *Conductivities of solid bodies [11]*

Solid	Material	Conductivity
Finned capillary	Copper	$k_c = 0.0028 \, T_c^2 - 1.525 \, T_c + 608$
Mandrel	Monel	$k_m = 6.5169 \ln(T_m) - 14.76$
Shield	Stainless steel	$k_s = 5.0353 \ln(T_s) - 13.797$

Biot number calculated at the inlet and exit of the heat exchanger, for the finned capillary, mandrel and shield are given in Table 3.5.

Table 3.5. *Biot numbers of the solid bodies calculated at each end of the heat exchanger*

Solid	T at x = 0 [K]	Bi [-]	T at x = L [K]	Bi [-]
Capillary	292.5	0.0051	168.1	0.0071
Mandrel	282.6	0.0037	109	0.0079
Shield	282.6	0.0082	159	0.016

As can be seen from the Table 3.5, Biot numbers of all solid bodies remain below 0.1 throughout the heat exchanger length. All of the solid bodies can be taken as lumped in the radial direction.

3.2.4. Analysis of Viscous Dissipation

In order to analyze if the effect of viscous dissipation term needs to be considered within the energy equations of fluids, the Eckert number needs to be analyzed. Eckert number is defined as follows [20]:

$$Ec = \frac{V_x{}^2}{c_p\,\Delta T} \tag{12}$$

where V_x is the velocity of the flow in the axial direction, calculated as the mass flux divided by the density. The Eckert number is found to be 0.057 at the inlet and 0.015 at the exit of the tube side flow. The viscous dissipation term is important when Eckert number is almost equal to 1. Therefore, it is safe to neglect the viscous dissipation terms.

3.3. Governing Equations

In order to determine the steady state temperature and pressure profiles along the length of the heat exchanger, the conservation of momentum and energy equations are solved. The continuity equation is not solved but used to simplify other conservation equations. The solid bodies are assumed to be lumped in the radial and angular directions. As a result, the system is modeled as 1D. The viscous dissipation terms are neglected. The initial forms of the differential equations are given in Appendix A. The differential equations are simplified using the assumptions validated in section 3.2. The final forms of the conservation equations after these assumptions are given below.

3.3.1. Continuity Equation for Fluid Flows

The continuity equation in the flow direction may be expressed as

$$\frac{dV_x}{dx} = -\frac{G}{\rho^2}\frac{d\rho}{dx} \qquad (13)$$

where V_x is the velocity in the flow direction, G is the mass flux and ρ is the density.

3.3.2. Conservation of Momentum Equation for Fluid Flows

The conservation of momentum equation in the flow direction may be expressed as

$$\frac{dP}{dx} = \left[\frac{2\,f\,G^2}{\rho\,d}\right]\Big/\left[\frac{G^2}{\rho^2}\frac{d\rho}{dP}-1\right] \qquad (14)$$

where f is the Fanning friction coefficient, G is the mass flux, ρ is the density, d is the inner diameter of the capillary tube for tube side flow and it is the hydraulic diameter for the shell side flow. The tube side flow path is longer than the heat exchanger length due to the helical direction. The differential element along the heat exchanger length, dx, is multiplied by L_c/L for the tube side flow.

3.3.3. Conservation of Energy Equation for Fluid Flows

The conservation of energy equation for the tube side flow is:

$$A_{\text{cross, tsf}}\left[Gc_p\frac{dT}{dx} + \frac{G\,T}{\rho^2}\left(\frac{\partial s}{\partial P}\right)_T\frac{dP}{dx}\right]_{\text{tsf}} = P_{\text{w,ci}}[h_{tsf}\,(T_c - T_{\text{tsf}})] \qquad (15)$$

where h_{tsf} is the heat transfer coefficient for the tube side flow.

The conservation of energy equation of the shell side flow is:

$$\begin{aligned}
A_{\text{cross, ssf}}&\left[Gc_p\frac{dT}{dx} + \frac{G\,T}{\rho^2}\left(\frac{\partial s}{\partial P}\right)_T\frac{dP}{dx}\right]_{\text{ssf}} \\
&= P_{\text{w,co}}\big[h_{ssf}(T_c - T_{ssf})\big] + P_{\text{w,m}}\big[h_{ssf}(T_m - T_{ssf})\big] \\
&\quad + P_{\text{w,s}}\big[h_{ssf}(T_s - T_{ssf})\big]
\end{aligned} \qquad (16)$$

where h_{ssf} is the heat transfer coefficient for the shell side flow. In all of the numerical studies found in JT heat exchanger literature, the same heat transfer coefficient is used between the shell side flow and capillary, mandrel, shield. The correlation is suggested for the heat transfer between the shell side flow and the capillary due to the similarities between the geometries. However, the validity of using the same correlation for heat transfer between the shell side flow and mandrel/shield should be questioned. Different heat transfer correlations are investigated in the current study which are valid for internal flows, annulus flows, etc. However, a correlation suitable for the geometry and Reynolds range of the current study was not procured. Therefore, same correlation is used for both three heat transfer coefficients as done in the literature.

The term which represents the change of enthalpy with pressure, $\frac{G\,T}{\rho^2}\left(\frac{\partial s}{\partial P}\right)_T\frac{dP}{dx}$, is not present in the study of Ng et al. [11]. During the verification of the numerical model, this term is removed from the Eqns. (15) and (16). It is included within the numerical model during the model improvements section.

3.3.4. Energy Equation for Solid Bodies

The energy equation of the finned capillary is:

$$k_c\,A_{\text{cross, c}}\frac{d^2 T_c}{dx^2} = P_{\text{w,ci}}h_{tsf}\left(T_{tsf} - T_c\right) + P_{\text{w,co}}h_{ssf}\left(T_{ssf} - T_c\right) \tag{17}$$

where k_c is the conductivity of the finned capillary. To calculate the wetted perimeter of the finned capillary external surface, it is assumed that the fin temperature is equal to the capillary temperature and does not vary along the fin length. This assumption requires analysis of the fin efficiency. The fin efficiency is controlled using reference [20] for annular fins of rectangular profile. It is found that the fin efficiency is almost 100% along the heat exchanger length. Therefore, it is valid to assume that the temperature along the fin length is does not vary.

The energy equation for the mandrel is:

$$k_\text{m}\, A_\text{cross,m}\, \frac{d^2 T_\text{m}}{dx^2} = P_\text{w,m} h_\text{ssf} \left(T_{ssf} - T_\text{m} \right) \tag{18}$$

where k_m is the conductivity of the mandrel.

Finally, the energy equation of the shield is:

$$
\begin{aligned}
k_\text{s}\, A_\text{cross,s}\, \frac{d^2 T_\text{s}}{dx^2} &= P_\text{w,s} h_{ssf} \left(T_{ssf} - T_\text{s} \right) \\
&+ P_\text{w,so}\, \sigma \left(T_\text{amb}{}^4 - T_\text{s}{}^4 \right) \left[\frac{1}{\varepsilon_\text{s}} + \frac{(1 - \varepsilon_\text{ext})}{\varepsilon_\text{ext}} \frac{A_\text{s}}{A_\text{ext}} \right]^{-1}
\end{aligned}
\tag{19}
$$

where k_s is the conductivity of the shield.

The shield has radiation interaction with the external body covering the shield. The emissivity of the external body is given as 0.08 and the shield is given as 0.08 by Chua et al. [66]. The conductivities of solids are given in Table 3.4 as a function of solid temperature, in Kelvin. The shield temperature varies from room temperature at the hot end of the heat exchanger, to a cryogenic temperature at the cold end. Defining the emissivity of the shield as a function of temperature is discussed in the model improvements section.

It can be seen from Eqns. (17), (18) and (19) that the second derivative of thermal conductivity terms are not considered within the energy equations of solids. This is because when an order of magnitude analysis is performed, the second derivative of conductivities as given in Table 3.4 are 3 order of magnitudes smaller than the second derivatives of the temperature terms. Therefore, even though the thermal conductivities are recalculated at every node with the temperature of the solid bodies, the second derivatives are neglected from the energy equations.

3.3.5. Tube Side Flow Friction Correlation

For the tube side flow, it is stated in [11] that the correlation given by Timmerhaus and Flynn [12] for flow inside helical tubular pipes is used. The correlation is as follows.

$$\frac{\Delta P}{\Delta L_{tsf}} = 0.092 \, G^2 \left[1 + 3.5 \left(\frac{D_{\mathrm{i}}}{D_{\mathrm{hel}}} \right) \right] / [Re^{0.2} D_{\mathrm{i}} \, \rho] \tag{20}$$

When equation (20) is incorporated into equation (14), the friction factor for the tube side flow is obtained as

$$f_{tsf} = 0.046 \, Re_{tsf}^{-0.2} \left(1 + 3.5 \, \frac{d_{\mathrm{c,i}}}{d_{\mathrm{hel}}} \right) \tag{21}$$

However, the friction correlation given in [11] for the tube side flow is as follows.

$$f_{\mathrm{tsf}} = 0.184 \, Re_{\mathrm{tsf}}^{-0.2} \left(1 + 3.5 \, \frac{d_{\mathrm{c,i}}}{d_{\mathrm{hel}}} \right) \tag{22}$$

Comparing equation (21) with equation (22), it is seen that there is a difference by a factor of four. This difference can be traced back to the study of Chou et al. [54]. The momentum equation is derived using the Darcy friction factor in [54]. As a result, the friction correlation given is four times larger than equation (21), which is derived using Fanning friction factor. In some later studies [10, 11, 32, 66, 73, 74] even though the momentum equation is derived using the Fanning friction factor, the correlation given in [54] is used. As a result, the pressure drop is calculated as four times larger than the expected value. References [64, 70] are the ones that avoided this mistake.

The correlation given in Eqn. (22) is used in the verification study. The correlation given in (21) is incorporated within the numerical model during model improvements.

3.3.6. Shell Side Flow Friction Correlation

The friction correlation used in the study of Ng et al. [11] is not given. In the study of Chua et al. [66] the following correlation for the shell side flow is used.

$$f_{ssf} = 0.184 \, Re_{ssf}^{-0.2} \tag{23}$$

Similar to the discussion given in section 3.3.5 about the tube side flow friction correlation, the correlation given in (23) is also four times larger than the value suggested by Timmerhaus and Flynn [12]. During the verification, Eqn. (23) is used for friction coefficient of the shell side flow. A different correlation is suggested and utilized in the model improvements section.

3.3.7. Heat Transfer Correlations

For the tube side flow, the heat transfer correlation for flow inside helical tubular pipes given by Timmerhaus and Flynn [12] is used. The correlation is as follows:

$$h_{tsf} = 0.023 \left(c_p G Re^{-0.2} Pr^{2/3} \right)_{tsf} \left(1 + 3.5 \, \frac{d_{c,i}}{d_{hel}} \right) \tag{24}$$

For the shell side flow, the heat transfer correlation for bank of inline tubes given by Timmerhaus and Flynn [12] is used. The correlation is given as follows:

$$h_{ssf} = 0.26 \left(c_p G Re^{-0.4} Pr^{2/3} \right)_{ssf} \tag{25}$$

3.3.8. Thermophysical Properties of The Working Gas

The temperature and pressure of the working gas changes along the heat exchanger, considerably. The gases used in JT cooling applications are specifically selected from gases which show real gas effects, as temperature decrease in an isenthalpic process

cannot be seen in a gas which shows ideal gas behavior. Assuming ideal gas law results in a large error, especially for the tube side flow where the gas is in supercritical phase. The compressibility factor of the tube side flow may vary from approximately 0.94 at the inlet of the heat exchanger to 0.57 at the exit. In order to prevent this error, equations given in literature for real gas behavior of argon are used. Due to the large variation of the temperature and pressure along the length, in the current analyzed case specific heat of the tube side flow changes from 0.76 kJ/kg.K to 1.54 kJ/kg.K, Pr changes from 0.83 to 1.61, friction coefficient changes from 0.0067 to 0.0073 and heat transfer coefficient changes from 15685 W/m^2.K to 22164 W/m^2.K. Similarly, for the tube side flow specific heat changes from 0.4555 kJ/kg.K to 0.5219 kJ/kg.K, Pr changes from 0.5794 to 0.6654, friction coefficient changes from 0.0963 to 0.1184 and heat transfer coefficient changes from 399 W/m^2.K to 629 W/m^2.K. The changes are large and nonlinear, therefore these parameters cannot be taken as constant, average values along the heat exchanger length and should be calculated at every node.

For calculation of enthalpy, entropy, specific heat and density, the equations given by Lemmon and Jacobsen [13] are used. The derivatives, such as $\partial s/\partial P$ or $\partial \rho/\partial P$ are also derived using these equations. For transport properties such as the viscosity and the thermal conductivity, equations given by Stewart and Jacobsen [14] are used. The equations are valid from triple the point of argon (83.8 K, 0.69 bar) till 1200 K and 1000 MPa. The calculation procedure of the thermophysical properties are described in Appendix B. The constant pressure lines shown on the temperature-entropy diagram of argon generated by the code written in this study can be seen in Figure 3.2. The thermophysical properties of argon gas calculated using the code written in the current study are compared with the values given in the reference studies [13] and [14]. The values calculated are in good agreement with the values presented in the references.
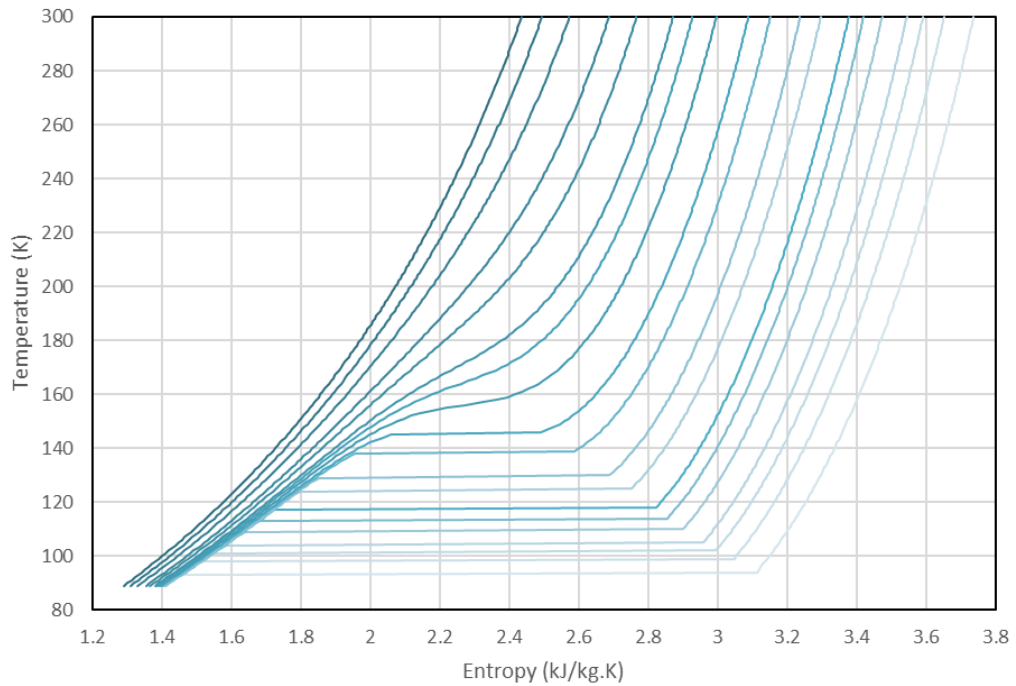
Figure 3.2. Temperature – entropy diagram of argon, showing constant pressure lines

3.4. Solution Method

Final forms of the differential Eqns. (14 – 19) are discretized using the finite difference method on a uniform one-dimensional mesh. The node number is selected after a mesh independence study. First order space derivatives of the momentum and energy equations of the gas medium are discretized using upwind differencing by paying attention to the flow direction. Second order derivatives are discretized using central differencing. All 7 differential equations are discretized into a single linear algebraic equation system. The system is nonlinear due to the dependency of the transport and thermophysical properties on the unknowns. Solution is obtained iteratively using Picard linearization, where the properties at the current iteration are evaluated using the values of the previous iteration. Convergence is declared when the difference between the calculated values for the unknowns of two consecutive iterations drop below 10^{-5}, which is typically achieved in less than 25 iterations. Flowchart of the developed code is shown in Figure 3.3.
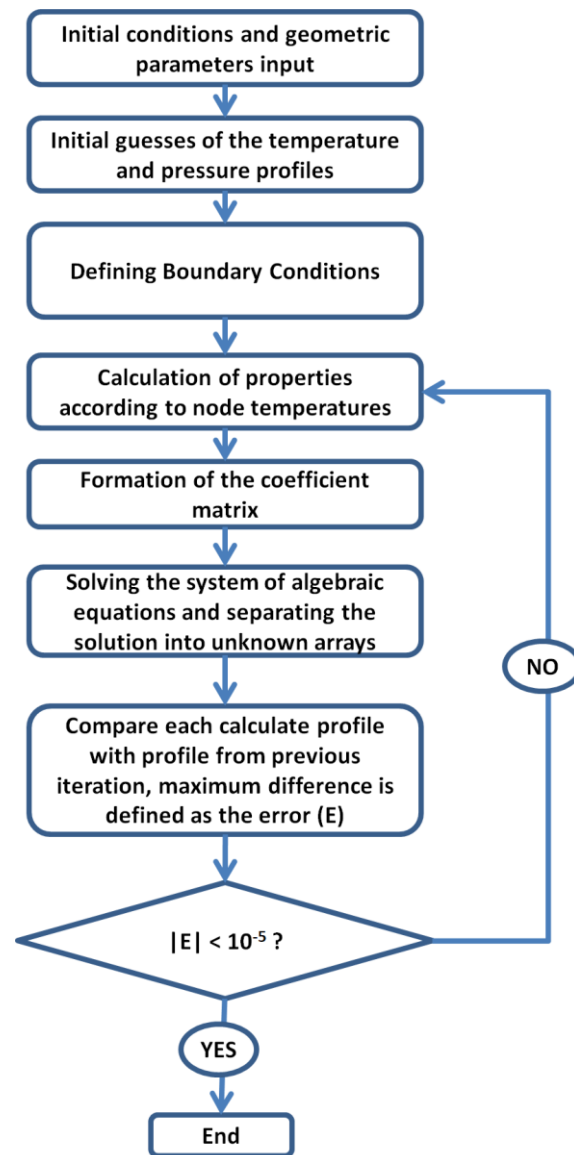
Figure 3.3. Flowchart of the developed code

To determine the number of nodes to be used, a mesh independence study is performed. For this purpose, Q and the shell side flow pressure drop are calculated with different number of meshes. The results of the mesh independence study can be seen in Figure 3.4. The model built gives diverging results when number of nodes is smaller than 176, so it is not possible to make a distinction between number nodes around 100 with number of nodes around 2000. When 200 nodes and 2000 nodes are compared, the difference between the shell side pressures drop is less than 0.1% and

Q is less than 2%. When 500 and 2000 nodes are compared, the difference between Q is 0.5%, which is numerically sufficient. Therefore, number of nodes is specified as 500 in the current study.
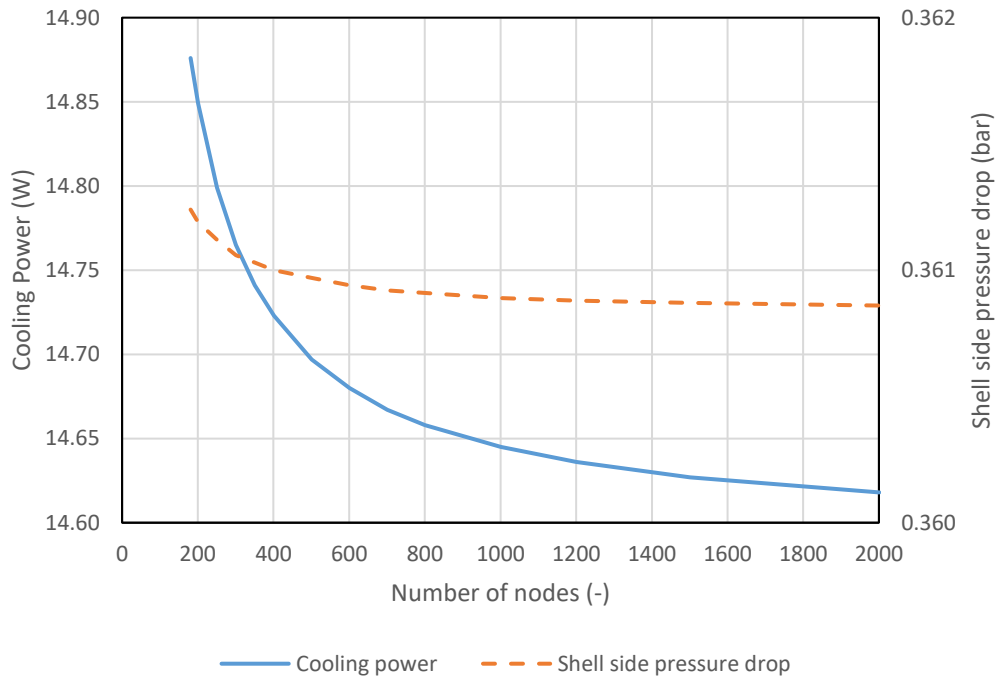
Figure 3.4. Change of Q and the shell side pressure drop due to the change of number of nodes

There are different boundary conditions suggested in the literature for the solid bodies. Xue et al. [65] suggested constant temperature at the hot end of the heat exchanger, which is equal to the tube side inlet temperature, and adiabatic condition at the cold end. The reference study [11] and some other studies which analyzed the same case [10, 32, 73] suggested adiabatic boundary condition at both ends of the heat exchanger. The rest of the numerical studies did not inform which boundary conditions are used. Insulating the solid bodies at the hot end of the heat exchanger is possible to minimize the heat gain from the ambient into the heat exchanger. Adiabatic boundary condition at the hot end of the heat exchanger is an applicable boundary condition and also used in this study as the first boundary condition. However, application of

adiabatic boundary conditions at the cold end results in diverging solutions. Alternatively, for the second boundary condition the solid temperatures are taken constant at the hot end of the heat exchanger. The shield and mandrel temperatures are equal to the shell side flow temperature. For the finned capillary, the heat transfer between it and the tube side flow is taken equal to the heat transfer between the finned capillary and the shell side flow. The capillary temperature is calculated from energy balance.

For the tube side flow, inlet pressure and temperature are taken as known in the reference study [11]. For the shell side flow, the inlet pressure and temperature are measured for the case studied and defined as boundary conditions by Ng et al. [11]. The inlet pressure is given as 1.73 bar and the inlet temperature is given as 110.36 K. The same boundary conditions are applied during the verification. As discussed in section 2.5.7, most of the studies in the literature used these boundary conditions for the shell side flow inlet. However, these experimentally measured results are valid only for a certain configuration and subject to change in an optimization study where the geometry and working conditions vary. The shell side flow is exhausted to the atmosphere at the hot end at a subsonic speed, so the exit pressure can be taken as atmospheric pressure. The inlet pressure of the shell side is calculated using the pressure drop of the shell side flow. This approach is similar to the one used by Hong et. al [70]. This procedure is more physical than the one used in many of the reference studies, but it puts more emphasis on the correct prediction of the shell side pressure drop, which depends on the f_{ssf} correlation used.

The inlet of the shell side flow is assumed to be at saturated vapor state, as discussed in section 2.5.3. Moreover, the inlet temperature is subject to change with changing inlet pressure in an optimization study. The verification is performed using the measured inlet temperature and pressure of the shell side, as done in the study of Ng et. al [11]. After the verification, the model is improved by including calculation of the inlet temperature as saturation temperature at the calculated inlet pressure.

3.5. Verification of the Developed Code

The verification of the code is achieved by comparing the results obtained with the numerical results presented in the reference study [11]. In order to obtain comparable results, same equations are solved. The tube side friction correlation given in Eqn. (22) and the shell side friction correlation given in (23) are used. The shell side inlet conditions are defined as the measured values given by Ng et al. [11]. The term representing the change of enthalpy with pressure is neglected. The comparison of the calculated temperature distributions along the heat exchanger length for both the tube and shell side flows with those given by Ng et al. [11] can be seen in Figure 3.5. The results are in good agreement. The exit temperature of the shell side flow is calculated as 284.60 K, which was given as 282.85 K in [11], with less than 2 K difference.
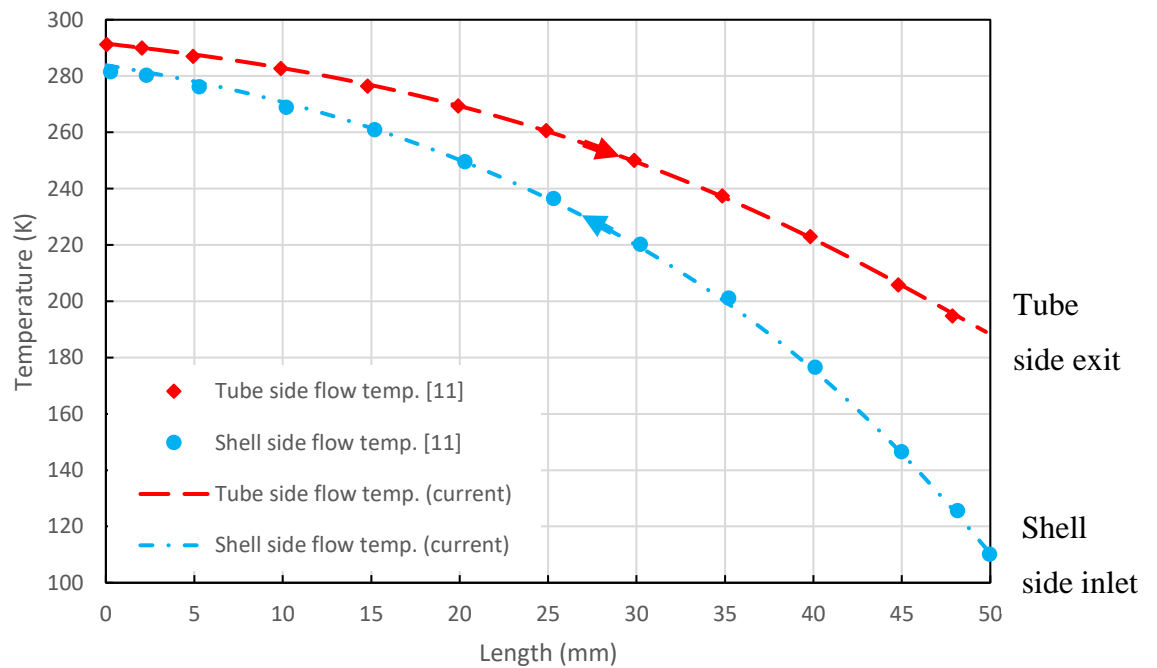
Figure 3.5. Comparison of the temperature profiles along the heat exchanger length calculated in the current study, in comparison with the results presented by Ng et al. [11]

When temperature profiles of the solid bodies calculated with the numerical study provided by Ng et al. [11] is analyzed, there seems to be an oscillation of the shield

and mandrel temperatures around the shell side flow temperature curve. Both temperatures are lower than the shell side flow temperature at the hot inlet and both end up with a higher temperature at the cold inlet; therefore, they cross the shell side flow temperature profile. A similar behavior of shield and mandrel temperatures is also seen in the results presented by Chou et al. [54]. The numerical model built in the current study also gave oscillating temperature profiles, as can be seen in Figure 3.6. The oscillations are physically incorrect and is a result of a numerical error. It is possible to increase the wavelength of the oscillations and finally obtain a profile without oscillations by decreasing the number of nodes used. However as presented in Figure 3.4, decreasing number of nodes results in a large error in the performance parameters analyzed and therefore unfavorable for the current study. Temperature profiles of the solid bodies are not used in the current analysis and do not change the results obtained in the optimization section. However, the source of the numerical error which causes the oscillations needs further investigation and correction.
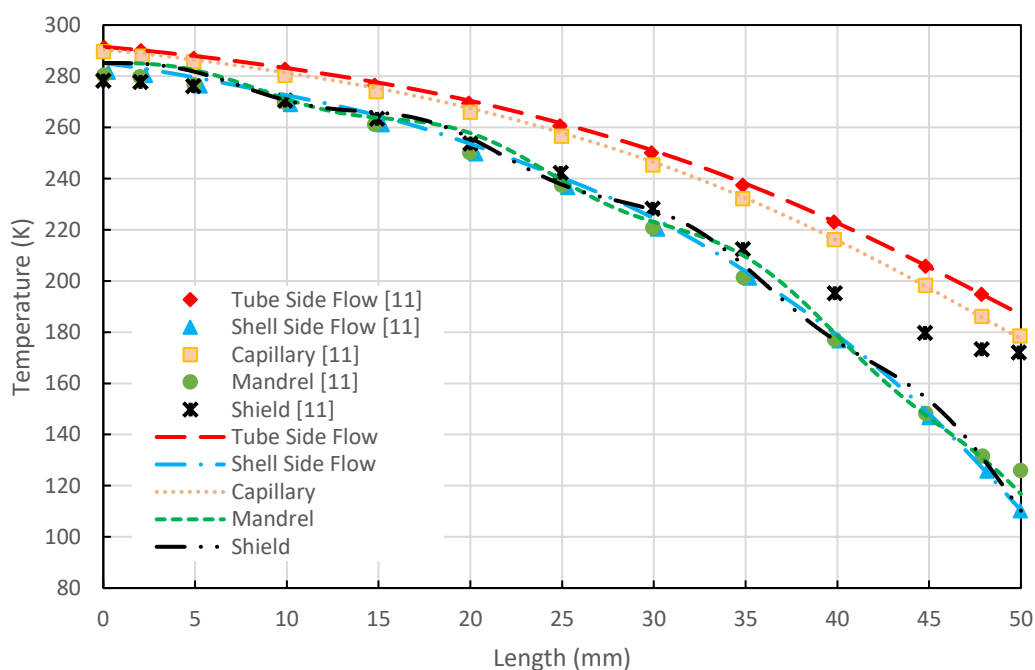
Figure 3.6. Temperature profiles of the solid bodies along the heat exchanger length calculated in the current study, in comparison with the results presented by Ng et al. [11]

3.6. Numerical Model Improvements

After testing the model with the reference study, the Q of the cryocooler is calculated using the states given by Ng et al. [11], as -0.096 W. This indicates that the enthalpy of the shell side inlet is lower than the enthalpy of the tube side exit, which is not physical. In [66], it is reported that [11] exhibits significant thermodynamic inconsistency. Therefore, the model built using the equations, correlations and boundary conditions according to the study of Ng et al [11] needs to be corrected and improved. For this purpose, the following modifications, some of which are also discussed in the previous sections, are applied to the numerical model.

Modification 1: For the tube side flow friction correlation, Eqn. (22) was used during the verification, as given by Ng et al. [11]. As discussed in Section 3.3.5, Eqn. (21) is the friction correlation which is consistent with the momentum equation (14). Therefore, the tube side flow friction correlation is changed to Eqn. (21).

Modification 2: The enthalpy was equated as a function of temperature only in the study of Ng et al. [11] and the change of enthalpy with pressure was neglected. However, the thermophysical properties of argon are obtained from equations which take the real gas effects into account. Considering the real gas effects for the thermophysical properties but developing the conservation of energy equation based on the ideal gas assumption results in an inconsistency. The term which determines this effect, $\frac{G\,T}{\rho^2}\left(\frac{\partial s}{\partial P}\right)_T \frac{dP}{dx}$, is added to the conservation of energy equations of both tube and shell side flows, namely Eqns. (15) and (16).

Modification 3: For the shell side flow friction correlation, Eqn. (23) was used in the verification study, which is the correlation given Chua et al. [66]. In several earlier studies [10, 32, 66, 74], the shell side flow was taken as flow inside straight channels, formed by the mandrel, shield, capillary tube and the fins. However, the shell side flow path cannot be simplified as straight channels, as discussed in section 3.2.1.

A better correlation, suggested in this study for the first time in JT cooler heat exchanger analysis is the correlation suggested for the Collins tubing, where gas flows inside an annulus which is filled with helically wounded fins. The difference between

61

the Collins tubing and the shell side geometry of a JT cooler heat exchanger is that the helical capillary tube is not present in the Collins tubing. Collins tubing correlation is given for flow in annulus without phase change (single phase gas flow), with $400 <$ Re < 10000. The Reynolds number of the shell side flow is within acceptable limits for the Collins tubing correlation. The following correlation given by Timmerhaus and Flynn [12] for Collins tubing is suggested for the shell side flow friction correlation.

$$\frac{\Delta P}{\Delta L}_{ssf} = 0.952 \ G^2 \ /[Re^{0.2} d_{\mathrm{hyd}} \ \rho] \tag{26}$$

Combining Eqn.s (14) and (26), the following Fanning friction factor is used in the current study.

$$f_{ssf} = 0.476 \ Re^{-0.2} \tag{27}$$

Modification 4: The inlet pressure of the shell side flow is defined as a constant input pressure, which is a measured value in most of the studies [10, 11, 32, 65, 73, 74]. This approach is not applicable in an optimization study, as it requires measuring the shell side inlet pressure for each working condition and geometry that is studied. A better approach, which is applied in some of the studies [2, 70] is to define the exhaust pressure as atmospheric pressure and calculate the inlet pressure through the pressure drop of the shell side along the heat exchanger length. It is valid to assume that the exit pressure is atmospheric, as the Mach number of the shell side flow varies between 0.057 to 0.006 along the heat exchanger. With this modification, a new inlet pressure is calculated with changing geometry and working conditions.

Modification 5: Similar to the discussion presented in modif. 4, the inlet temperature of the shell side is defined as a constant, measured temperature in most of the studies, which is only valid for the specific geometry and working conditions of the reference study [11]. As discussed in Section 2.5.3, the inlet temperature of the shell side is

defined as the saturation temperature at the calculated inlet pressure. This definition allows variation of the shell side inlet temperature for every different case analyzed in an optimization study. The shell side inlet temperature also determines the working temperature of the system which is an important parameter, defining the performance of the detector in IR imaging applications.

Modification 6: The emissivity of the shield, which is stainless steel, is taken constant as given by Chua et al. [66]. Woods et al. [75] showed that emissivity of stainless steel changes considerably at cryogenic temperatures and should be taken as a function of temperature. The change of emissivity of stainless steel as a function of temperature is presented in Figure 3.7.
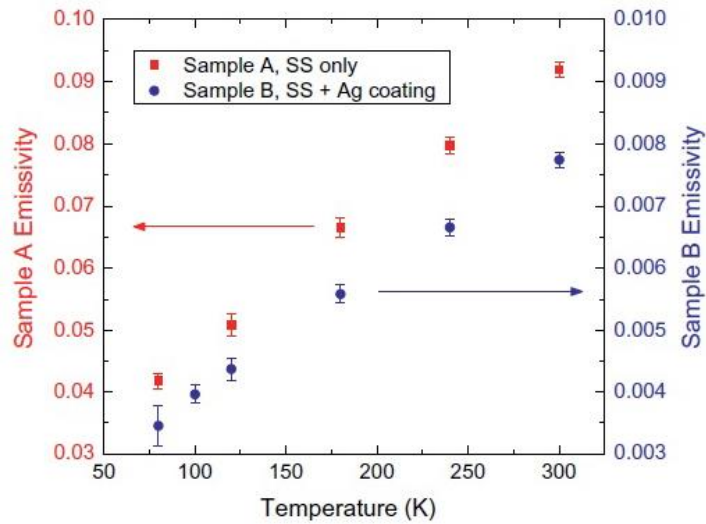
Figure 3.7. Emissivity of stainless steel as a function of temperature [76]

Curve fitting to the data given in Figure 3.7, the following linear correlation is used for the emissivity of the shield as a function of temperature.

$$\varepsilon_s = 0.00023\, T_s + 0.024 \qquad (28)$$

3.6.1. Effects of Model Improvements on Results

The model improvements are analyzed through the effects on Q, the tube side pressure drop and the shell side pressure drop. To meet a Q requirement is generally the primary objective of a cooler system, and suggested as one of the most important performance parameters of JT coolers by Maytal [55]. The tube side pressure drop is one of the mostly affected parameters from the suggested modifications, due to the wrong correlations used before. It is important to control the tube side pressure drop, as too high pressure drop results in a diverging solution. The shell side pressure drop on the other hand affects the working temperature of the target body, therefore an important performance parameter. The importance of each performance parameter are further discussed in the optimization study.

The 1st and the 2nd modifications affect the calculated Q and the tube side pressure drop values the most, as shown in Table 3.6. They have minor effect on the shell side pressure drop. Correcting only the friction coefficient of the tube side flow (Modif. 1), it is possible to get a positive Q value, which is thermodynamically meaningful. Further considering pressure dependency of enthalpy (Modif. 2) increases the cooling load by 37% and decreases the tube side pressure drop by 6%. Therefore, it is vital to use the correct friction factor definition and to consider real gas effects on enthalpy. The change in the shell side pressure drop correlation increases the cooling load by 9% and it results in a shell side pressure drop which is 2.7 times larger. The combined effect of modifications 4 and 5 results in an increase of Q by 6.8%, decrease of tube side pressure drop by 4.3% and increase of shell side pressure drop by 28%. Shell side pressure drop is an important performance parameter for a JT cooler, therefore it is important to define shell side boundary conditions correctly. An important advantage of using modifications 3 and 4 is, they allow to work with different configurations where the inlet state of the shell side flow is not known experimentally. After all the modifications are applied, the shell side flow exit temperature is calculated as 270 K. The temperature profiles along the heat exchanger length presented in [11] are found through a numerical study. The only experimental result presented is the exhaust temperature of the shell side flow. The final temperature profiles obtained after all suggested improvements are applied cannot be compared with numerical results

presented in [11]. Only the exhaust temperature of shell side flow is compared with the experimental value presented in [11].

Table 3.6. *Effects of model modifications on the performance parameters of the heat exchanger*

Case	Q [W]	Tube side pressure drop [bar]	Shell side pressure drop [bar]
Reference study [11]	-0.096	103.22	0.108
Modif. 1	9.21	20.08	0.111
Modif. 1 & 2	12.64	18.87	0.106
Modif. 1, 2 & 3	13.76	18.40	0.283
All modifications	14.70	17.61	0.361

The states of the thermodynamic cycle calculated with the enhanced model and the control case is given in Figure 3.8 on a temperature-entropy diagram. States 1 and 2 are the inlet and the exit states of the tube side flow, respectively. The gas goes through isenthalpic expansion from state 2 to 3. The transitions from state 2 to state 3 shown on Figure 3.8 are derived from constant enthalpy lines. State 3 is the liquid-gas mixture formed at the cold end. The mixture extracts heat from the target body from state 3 to state 4. As discussed above and can be seen in Figure 3.8, state 3 and state 4 of the control case are quite close to each other. In fact, enthalpy of state 3 is slightly higher than that of state 4 for the control case, which results in a negative Q. Liquefaction does not occur in the control case under the given conditions. State 4 is the inlet state of the shell side flow. In a real system, state 4 may be in liquid-mixture region if some amount of liquid escapes into the shell side flow, or it may be in superheated region if the latent heat of vaporization is not enough to extract the heat generated at the target body. However, in this study state 4 is assumed to be in saturated vapor state at the cold end pressure.

Modification 1 resulted in a lower pressure drop at tube side flow. The effect of this modification on states of the cycle is the shift of state 2 to the left, as can be seen in Figure 3.8. State 3 is not calculated through the numerical model but derived from

65

state 2, so modification 1 also resulted in a shift of state 3 to the left (i.e. lower enthalpy). Modification 2 is not directly distinct in Figure 3.8. Each point on the line from state 1 to state 2 shifted to a lower enthalpy point due to modification 2, as a result state 2 is at a lower enthalpy. This also resulted in an increase of enthalpy difference between states 3 and 4. Modification 3 resulted in a shift of every point between states 4 and 5 to the right (i.e. to a lower pressure value). Modification 4 directly effects state 5. Previously, state 5 was being calculated in the code. Due to modification 4, it is now defined at the atmospheric pressure. This shifted of state 5 to the right. Moreover, it also effected state 4. Pressure of state 4 was defined at a constant pressure before, but now it is being calculated. This resulted in a shift of state 4 to the right, to a lower pressure value. Modification 5 is about the definition of state 4. It resulted in a shift of state 4 along with state 5 down, to lower temperatures.
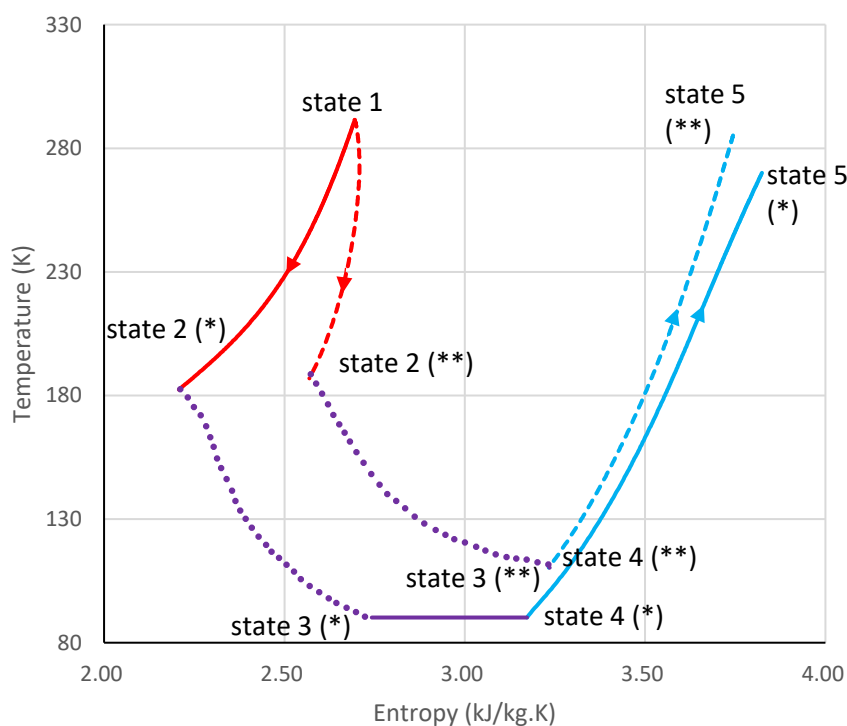
Figure 3.8. States of the cycle calculated by the improved model (*) and by the model of the reference study [11] (**)

66

3.6.2. Validation of The Previous Assumptions Using the Improved Model

After the states of the problem are calculated using the enhanced numerical model, the validity of the assumptions made during simplification of equations should be re-questioned. The non-dimensional parameters calculated using the states given in [11] and those obtained by the enhanced model are given in Table 3.7. It is seen that similar values are obtained, therefore previous discussions presented in section 3.2 are valid. All of the assumptions made are still applicable, the enhanced model does not need further changes.

Table 3.7. *non-dimensional numbers calculated for the validation of the assumptions made during simplification of the equations*

State no	State 1		State 2		State 4		State 5	
	[44]	Current	[44]	Current	[44]	Current	[44]	Current
Re [-]	57356	55306	85971	35762	2496	2948	1050	986
L_e [mm]	8.2 (1.5%)	8.2 (1.5%)	-	-	-	-	-	-
Bi_c [-]	0.0051	0.0050	0.0071	0.0066	-	-	-	-
Bi_m [-]	-	-	-	-	0.0037	0.0030	0.0079	0.0027
Bi_s [-]	-	-	-	-	0.0082	0.0068	0.016	0.0071
Ec [-]	0.057	0.11	0.015	0.0044	-	-	-	-

3.6.3. Thermodynamic Analysis of the Cycle

A thermodynamic analysis of the cycle is performed using the results obtained with the improved model. The effectiveness of a heat exchanger is defined as the ratio of the heat transfer rate to the maximum possible heat transfer rate [20] for the side which has lower specific heat. The maximum possible heat transfer rate is defined as an ideal case where the heat exchanger length is infinitely long. In the current case studied, the maximum possible heat transfer rate is the enthalpy increase of shell side flow from the inlet state to an ideal exhaust state where the temperature is equal to the inlet

temperature of the tube side flow. The heat exchanger effectiveness is calculated as 89.56%.

In order to perform second law analysis of the system, the availabilities of each state needs to be calculated. Availability of each step are calculated with respect to the atmospheric dead state, which is equal to the ideal exhaust of the shell side flow, state 5*. The availability of any state, E_x, is calculated as follows.

$$E_x = \dot{m} \left[(i_x - i_{5*}) - T_{5*}(s_x - s_{5*}) \right] \tag{29}$$

The availability of state 1, which is the input in the current case is calculated as 117.69 W. The availability of state 2 is 128.49 W, which corresponds to an availability increase of 10.8 W. The availability of state 4 is 36.02 W and the availability of state 5 is 0.16 W, which corresponds to an availability decrease of 35.86 W. The ratio of the availability increase of tube side flow to the availability decrease of shell side flow gives the second law efficiency of the heat exchanger, which is calculated as 30.12% for the current case. The availability of state 5 is a potential which is loosed, also called as the flow loss. The availability of state 3 is calculated as 68.81 W. Therefore, the availability loss occurring due to the JT expansion process, i.e. the irreversibility (I) is 59.68 W. The second law efficiency of the complete cycle can be defined as the ratio of output obtained from the system, which is the cooling power in the current analysis, to the input given to the system, which is the availability of state 1. The second law efficiency is calculated as 12.49%. The results of the thermodynamic analysis are summarized in Table 3.8.

Table 3.8. *Results of the thermodynamic analysis*

E_1	117.69	[W]
E_2	128.49	[W]
E_3	68.81	[W]
E_4	36.02	[W]
E_5	0.16	[W]
ΔE_{tsf}	10.80	[W]
ΔE_{ssf}	35.86	[W]
η_{hex}	30.12%	[-]
η_{2nd}	12.49%	[-]
I_{JT}	59.68	[W]
I_{hex}	25.06	[W]

CHAPTER 4

OPTIMIZATION OF THE CRYOCOOLER GEOMETRY

After the numerical model is built and verified, it is first used to analyze the effect of possible design parameters on the selected objectives. The sensitivity of objectives on the design parameters are determined. The parameters that do not affect the objectives considerably are eliminated and so number of objectives which are analyzed in the optimization are decreased. The results of the sensitivity analysis are also used to determine suitable initial values of design parameters for the optimization study, which is named as pre-optimization. Once the design parameters and their initial values are decided, a result cloud is obtained by using full factorial method. The results which are out of specified design constraints are filtered from the result cloud. An optimization function is built which includes both of the objectives. The maximum value of the optimization function is searched within the result cloud obtained, through a grid search method. The geometry which is determined by the maximum value of the optimization function is used as an initial value for a second iteration of optimization. From comparison of the results achieved in both iterations, a final, optimum geometry is suggested according to the objectives.

4.1. Optimization Method

There are several different optimization methods found in the literature which are used for heat exchanger analysis. Genetic algorithms [13, 78-80], Artificial Bee Colony (ABC)[81], weighted sum, weighted product, Keeney-Raiffa [82], graphical analysis, mixed integer nonlinear programming, simulated annealing, tube count tables [79] are some of the optimization methods reported in the literature for analyzing heat exchangers. Liu et al. [74] performed an optimization study for a JT cooler using response surface methodology.

In the current study, a multi-objective optimization is performed using a stochastic method [83]. A solution cloud is obtained using full factorial method. The design parameters are varied within specified ranges, at different number of levels. In full

factorial method, the values of objectives are obtained at every possible combination of the design parameters, therefore it is a brute force technique. The total number of runs is equal to $L_1. L_2. L_3 ... L_k$, where L denotes number of levels each design parameter is analyzed and k denotes the number of design parameters. The total number of runs increases exponentially with increasing number of design parameters and levels. There are some several other Design of Experiments techniques which can be used to obtain a solution cloud, such as Latin Square, Fractional Factorial, Central Composite, etc. [83] The advantage of these methods is that total number of runs are decreased, therefore the optimization time is decreased. The advantage of full factorial method, all of the interactions between design parameters are considered, preventing any missing information about the system characteristic. The results of full factorial analysis can be interpolated to form response surfaces [83].

In the current study the number of design parameters which are analyzed is decreased through the sensitivity analysis. Moreover, the initial values of design parameters are changed from the values suggested in the reference study to values which better suits the objectives of the current study. Therefore, the number of levels through which the design parameters are varied, is also decreased. The total number of runs which is needed by full factorial method is decreased due to these two preliminary analysis. In addition, the model run time is acceptable, where results can be obtained with an average of 23 seconds in the current study. Even without eliminating the insensitive design parameters and decreasing the number of levels analyzed, a result cloud can be created in about one day, where around 3000 different case is analyzed. With the suggested simplifications, the result cloud is obtained in about 5 hours with 729 cases studied. In cases where finalizing the optimization is expected to last much longer and obtaining results at every combination of design parameter is not applicable, one of the other Design of Experiments approaches can be used where total number of runs are decreased.

In order to perform the optimization, first the result cloud is filtered according to the constraints. Then the results obtained for each objective are normalized using Euclidian approach [84]. In normalization using Euclidian approach, the result cloud of each objective is divided by the root mean square of the results. Alternatively, if

there exists a reference value for the parameter to be optimized (ideal value, maximum or minimum allowable value, etc.), the result cloud can also be divided by this reference value, which is called as the linear optimization. If a reference value cannot be defined, Euclidian approach is a suitable method to normalize the results. A final method for normalization is Fuzzy approach, where maximum value of a parameter is set at 1, minimum value is set at 0 and all of the results are normalized with respect to these maximum and minimum values, between 0 and 1. This method is used in parameters where the change of the parameter is important (temperature, enthalpy, entropy, etc.).

The two objectives which are studied in the current study are contradicting, therefore a change which results in a desired outcome with respect to one of the objectives may affect the other objective in an unfavorable manner. Because of this, a pareto optimum solution is searched [83]. Pareto optimum solution is obtained when a further change of a design parameter does not have a positive effect on one objective without having a negative effect on the other objectives.

The normalized objectives are brought together using weighted sum method [82] to build an optimization function. The weights assigned to the objectives demonstrates which objective is more important. Weighted sum is selected as it is the best known method. An alternative is weighted product method, where the values of different objectives are multiplied. Weighted product eliminates the requirement of normalization of the objectives. However, it results in similar significance of objectives on the optimization function. This can be an advantage or disadvantage, depending on the application. As the relative significance of objectives cannot be defined in the current study mathematically, the simpler approach, which is weighted sum, is selected. Some other methods for building an optimization function are Keeney-Raiffa, distance to a reference goal, ε-constraint, etc. [82] Finally, a grid search method [85] is used, where the maximum value of the generated optimization function is searched within the result cloud.

4.2. Objectives

There are various objectives studied in the JT cooler literature, such as Q [10, 48, 55, 66, 68, 70, 73], effectiveness of the heat exchanger [65, 66, 70, 73], shell side pressure drop [48, 70, 73], tube side pressure drop [48, 70, 73], entropy generation and losses in the system [65], cool down time [10, 32, 54, 60, 67-69], operation time [10, 69], etc. In this study, the objectives are selected in relation with requirements of cooling an IR imaging system.

Entropy generation minimization (EGM) is selected as an objective in several optimization studies [13, 74, 78]. However as discussed in [55], primary purpose of a cooler is not to operate with higher efficiency. Therefore, EGM is not selected as an objective in this study.

Minimizing the total volume of the cooler is a candidate of an objective. The dimensions of the cooler may be limited by the dimensions of the platform (i.e. external dimensions of the thermal camera, etc.), or they may affect the performance of the platform (i.e. if the cooler is used on a moving platform, the balance of the platform and limits of the motion may be affected). Maytal defined an objective to minimize the length of a JT cooler, called as compactness [55] and minimized it through similarity functions in an idealized cryocooler. In this study, only the performance parameters of an IR sensor are considered. The details which do not affect the performance of IR imaging but related with the platform, such as dimensional limitations, weight limitations, etc. are not addressed. Therefore, minimization of the cooler volume is not selected as an objective.

In an open cycle operation, the gas is fed from a constant volume gas vessel and used gas is exhausted to the atmosphere. Therefore, the operation time of the system is limited and determined by the volume and initial pressure of the vessel, mass flow rate of the cooler and the minimum pressure which results in cooling. During the operation, the vessel pressure decreases and as a result the mass flow rate decreases. Both decrease of inlet pressure and mass flow rate cause a decrease of Q. Due to this decrease, Q generated by the JT cooler is not adequate to meet the cooling requirement of the sensor at a certain time, called as the operation time, and the operation of the

sensor is terminated. The operation time is a candidate of an objective in open cycle JT applications. However, calculation of operation time requires additional information about limitations of gas vessel volume and pressure. These limitations are derived from platform requirements which are not related with the performance of IR imaging, such as the free allowable space, the allowable weight, strength of the vessel, etc. As the platform is not directly addressed in this study, the operation time is not selected as an objective in the current study.

The tube side pressure drop is selected as an objective in some studies. Within the analysis of model improvements, effects of modifications on the tube side pressure drop is also studied. This is because the tube side pressure drop is highly affected by the modifications due to the friction correlation mistake. However, the tube side pressure drop is not directly related with a performance parameter. Therefore, it is not selected as an objective in this study.

The primary function of a cooler system is to extract heat from a target body. Maytal suggested that performance parameters of a JT cooler, such as Q are strong candidates of objectives for an optimization study [55]. On the other hand, usually Q is strictly defined by the application and the cooler is generally designed to meet this Q requirement. Q above the system requirement does not bring additional advantage to the system. However, when it is below the requirement, it causes the system temperature to increase and, for IR imaging application, termination of the operation. Therefore, Q is used as a constraint in the current study.

An important objective, which is suggested and analyzed in the literature for the first time in this study, is q, which is Q per mass flow rate, can be maximized through optimizing the geometry of a JT cryocooler. As Q requirement of the JT cooler is predetermined, by maximization of q the flow rate of the system can be decreased. Decreasing the mass flow rate provides an increase of operation time for a constant gas source. Therefore, maximization of q by optimization of the geometry is selected as an objective in the current study.

The working temperature which is the temperature of the target body at steady state, is another important performance parameter in systems where cryocoolers are

required. In IR imaging systems, the system performance is directly influenced by the working temperature. The dark current, which is a measure of the noise generated within the system, increases with increased system temperature. The quality of the image is quantified by the signal to noise ratio. Increased noise may result in an undetectable signal. Using an idealized empirical correlation for Mercury-Cadmium-Telluride type detectors of the company Teledyne, operating at temperatures above 77 K [21], the change of dark current due to the temperature may be found in Figure 4.1. As can be seen, a decrease of working temperature from 98 K to 92 K results in a decrease of dark current by an order of magnitude. As it is important to decrease the noise so that the signal becomes detectable, it is important to minimize the working temperature. Similar correlations between working temperature and system performance exists in applications where cryocoolers are required. In type II superconductors, the magnetic field increases with decreasing temperature, between two temperature limits [17]. In an ideal system where argon is used, if the pressure drop at shell side is neglected, under normal circumstances the minimum working temperature is 87.2 K which is the liquefaction temperature of argon at 1 bar. Shell side pressure drop results in a higher liquefaction temperature at the cold chamber. To decrease the working temperature, the shell side flow pressure drop should be minimized. Therefore, minimization of the shell side pressure drop is selected to be another optimization parameter.
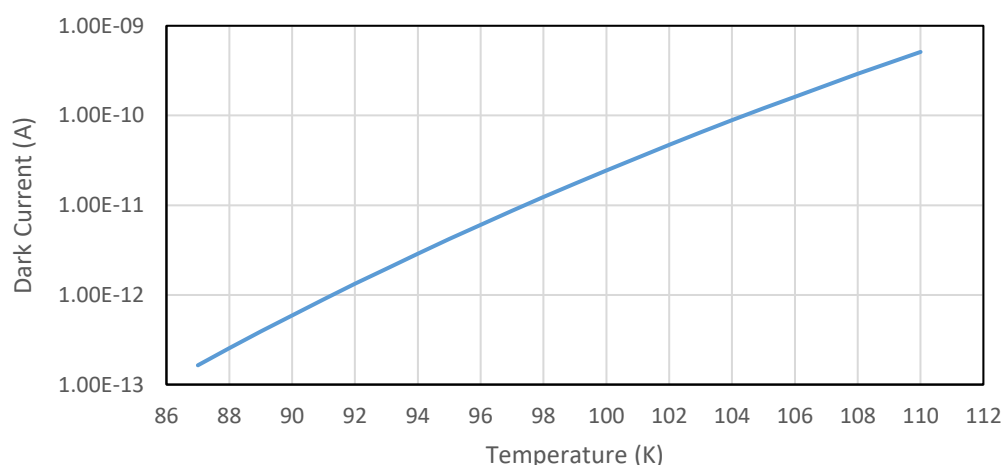
Figure 4.1. Change of the dark current with temperature, for an idealized MCT detector of Teledyne company [21]

4.3. Sensitivity Analysis

In order to design a JT cryocooler with certain requirements, the effect of each design parameter on the performance of the system needs to be known. To see the effect of design parameters on the selected performance parameters, a sensitivity analysis is done. The relative impacts of six design parameters on two objectives are evaluated systematically. The design parameters investigated in the current study are heat exchanger length, fin pitch, fin length, fin thickness, capillary inner diameter and capillary wall thickness. Some of the geometric parameters are not considered as optimization parameters. Shield diameter is one of these parameters, which is determined by the dimensions of the target body to be cooled, and therefore should not be changed in an optimization. In IR imaging applications, the shield diameter is determined with respect to the size of the detector. The detector may have a pixel format of 64 x 64, 1040 x 1040, 2048 x 2048, etc. with a minimum pixel size of approximately 18 µm [21]. The corresponding minimum shield diameters for these formats are 1.7 mm, 26.5 mm and 52.2 mm, respectively. The mandrel diameter is not a parameter which can be changed freely. It is calculated from shield diameter and fin outer diameter. Therefore, mandrel diameter is also not selected as a design parameter.

The effect of inlet pressure on Q is presented in several studies [10, 11, 32, 54, 55, 60, 65-71, 73, 74]. The effect on inlet pressure on Q is nonmonotonic due to the change of JT coefficient with pressure. There exists a maximum pressure, above which increasing the inlet pressure decreases q. It is discussed in [55] that for an idealized JT cooler where losses due to friction and heat transfer are neglected, maximum Q is reached at 532 bar for argon. It is evident that increasing the inlet pressure results in increased Q. On the other hand, the vessel pressure decreases with time in an open cycle operation. If the geometry and working conditions are optimized with inlet pressure which gives maximum Q, decrease in inlet pressure results in an inadequate Q and termination of the operation. Therefore, the operation time of the cooler is limited. When the cooler geometry is optimized for a certain inlet pressure, Q and operation time can always be increased by increasing the inlet pressure of the vessel. Analyzing the inlet pressure does not provide additional information to the literature,

therefore is not conducted in this study. The tube side inlet pressure suggested in [11] is used in the current study.

Flow rate is not considered as a possible design parameter in this study. As Q brings a constraint and q is an objective which is maximized, the flow rate is decreased through the analysis of these two parameters. However, it is not possible to directly calculate the final flow rate by Q/q. q is studied in the sensitivity analysis using the mass flow rate given in the reference study [11]. Changing mass flow rate effects both of the objectives. Direct division of Q constraint by the maximized q yields a lower mass flow rate than expected value. This decreases q and thus result in a lower Q than the constraint value. The final mass flow rate can be either found by iteration, or by analyzing the effect of mass flow rate on q. Therefore, even though the possible design parameters are selected as the geometric parameters, a similar sensitivity analysis is also be conducted to see the effect of mass flow rate on the objectives.

Considered intervals of each possible design parameter are provided in Table 4.1. As the cooler suggested in [11] is presented as a functional system that is used in experiments, the current sensitivity analysis considers the values of parameters given in [11] as base values and changes them within a practically applicable range. Each possible design parameter is varied individually over a specified range (approximately between half to twice of the values given in[11]) by keeping the others constant to understand the isolated effect of each design parameter on the objectives. The minimum fin pitch is selected such that the fin tips at mandrel side do not touch each other. The minimum capillary diameter is selected according to the pressure drop at the tube side flow. Any further decrease of capillary diameter causes pressure drop equal to or larger than the inlet pressure of the tube side flow.

Table 4.1. *Possible design parameters*

Design Parameters	Min value	Base value [11]	Max value
Heat exchanger length [mm]	30	50	100
Capillary internal diameter [mm]	0.22	0.30	0.50
Capillary wall thickness [mm]	0.05	0.10	0.20
Fin pitch [mm]	0.18	0.30	0.50
Fin length [mm]	0.10	0.25	0.50
Fin thickness [mm]	0.05	0.10	0.20

To compare the relative effect of each possible design parameter on objectives in a single plot, parameters are normalized using their base values. In normalization, the value of the design parameter is divided by the value given in the reference study. This is performed so that the effect of changing each parameter can be shown in a single plot. This can only be performed by nondimensionalization of the design parameters. Figure 4.2 and Figure 4.3 show the effects of each design parameter on q and the shell side pressure drop, respectively.
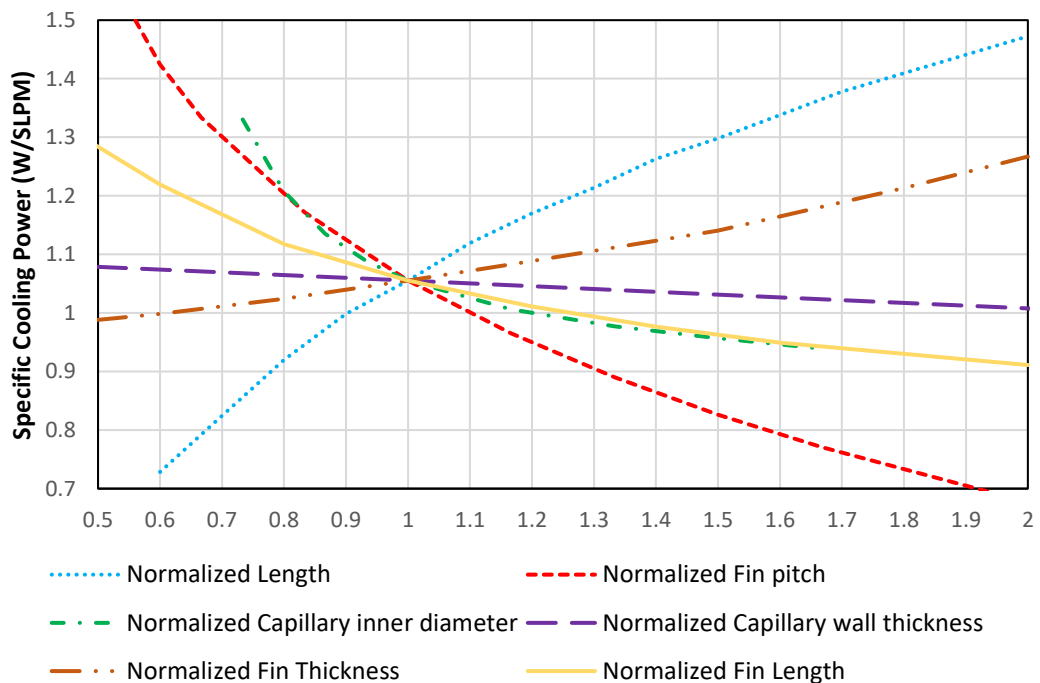
Figure 4.2. Isolated effect of possible design parameters on the specific cooling power
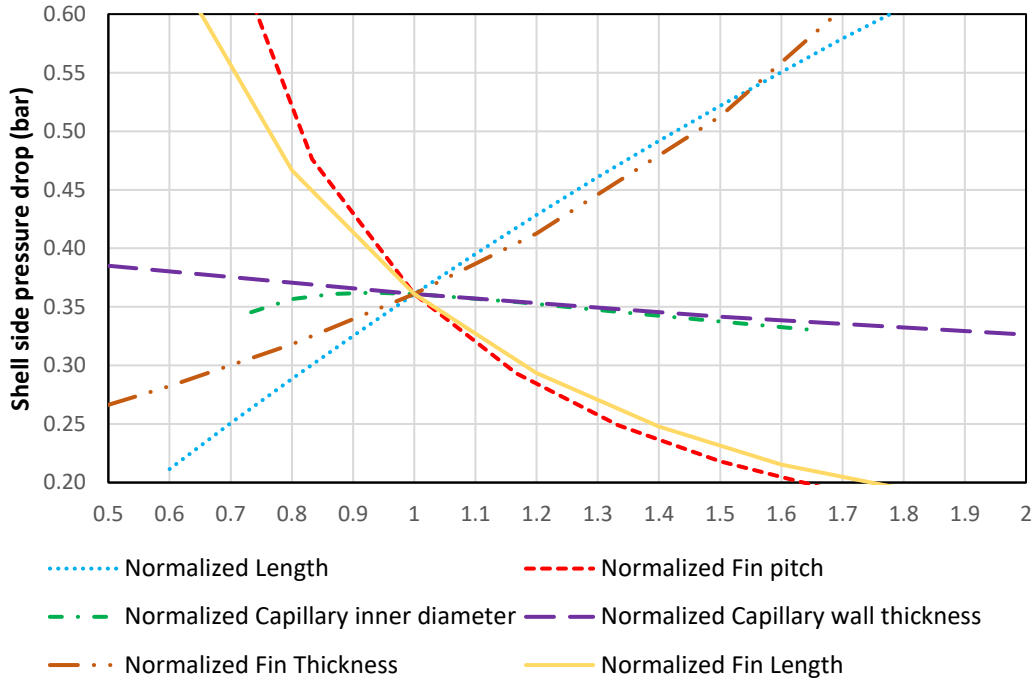
Figure 4.3. Isolated effect of possible design parameters on the shell side flow pressure drop

The objectives in the current study are to maximization of q and minimization of the shell side pressure drop. When considered separately, it can be seen from Figure 4.2 that to increase q, length of the cooler should be increased and capillary internal diameter should be decreased. Decrease of fin pitch, increase of fin thickness and decrease of fin length also cause an increase in q. To decrease shell side pressure drop, length should be decreased as can be seen from Figure 4.3. The change of shell side pressure drop with length is nearly linear. Increase in fin pitch, fin length and decrease in fin thickness also causes a decrease in shell side pressure drop.

The results of Figure 4.2 and Figure 4.3, showing the effect of changing each possible design parameter and the mass flow rate on objectives are summarized in Table 4.3. Increasing q and decreasing shell side pressure drop are highlighted with blue as these are the desired results. Similarly, decreasing q and increasing shell side pressure drop are highlighted with red as these are the undesired results.

Table 4.2. *Change of objectives due to changing possible design parameters and the mass flow rate*

Parameter	Change	Specific Cooling Power	Shell side pressure drop
L	-30%	-22%	-30%
	+30%	+15%	+28%
$d_{c,i}$	-25%	+23%	-3%
	+30%	-7%	-3%
t_c	-30%	+<1.5%	+4%
	+30%	-<1.5%	-3%
s_f	-30%	+25%	+95%
	+30%	-10%	-30%
w_f	-30%	+11%	+52%
	+30%	-6%	-25%
t_f	-30%	-4%	-17%
	+30%	+5%	+23%
m	-30%	-6%	-38%
	+30%	+6.5%	+42%

Analyzing Table 4.3 first of all it can be seen that the effect of capillary thickness on both objectives are negligible when compared with other parameters. Therefore, capillary thickness is kept constant at the value given in the reference study as 0.1 mm and is not considered as an optimization parameter.

Capillary inner diameter does not have a significant effect on the shell side pressure drop. As decreasing capillary diameter results in an increased q, the smallest possible capillary inner diameter may be selected in a design procedure. The limit of capillary inner diameter is specified by the tube side pressure drop. Decreasing the capillary inner diameter too much causes an increased tube side pressure drop. If the tube side pressure drop becomes equal to or larger than the tube side inlet pressure throughout the analysis, the result diverges. However, the flow rate is changed in the pre-optimization study as a result of change in q. Flow rate also effects the tube side pressure drop. When the flow rate is changed, the minimum allowable capillary diameter is also change. Therefore, the capillary inner diameter should be varied

during the optimization study and not kept constant as the minimum value suggested by the pre-optimization study.

Changing length, fin pitch, fin length and fin thickness have transverse effects on two objectives. The final values of these design parameters are determined through a coupled analysis. Decreasing fin pitch results in the highest increase in q. However, the effect of decreasing fin pitch also results in the highest increase in shell side pressure drop. On the other hand, increasing fin pitch also results in the highest decrease in the shell side pressure drop within the possible design parameters, together with decreasing length. The effect of length on shell side pressure drop is linear but fin pitch is exponential. Therefore, to decrease the shell side pressure drop, first the fin pitch should be increased. Due to the transverse effects on both objectives, fin pitch is selected as a design parameter and varied in the optimization study.

The effects of changing the length on both objectives are quite high, in both increasing and decreasing directions. It is not possible to directly comment on whether the length should be increased or decreased. Therefore, length is selected as a design parameter and varied in the optimization study.

Decreasing the fin length causes a high increase of q. However, within the possible design parameters, it results in the second highest increase in shell side pressure drop. On the other hand, increasing the fin length results in a high decrease of shell side pressure drop and a low decrease of q. The optimum value of the fin length is expected to be higher than the value given in the reference study. Fin length is selected as a design parameter and varied in the optimization study.

The effect of fin thickness on q is low. However, it effects the shell side pressure drop considerably in both increasing and decreasing directions. A lower fin thickness may be advantageous, depending on the combined effects of all design parameters. Fin thickness is selected as a design parameter and varied in the optimization study.

Through the sensitivity analysis, capillary diameter, length, fin pitch, fin length and fin thickness are selected as design parameters. Capillary wall thickness is not considered. To meet the constraint requirements, a pre-optimization study is

82

performed in the following section. During the optimization, the design parameters are varied within certain limits and the optimum geometry is searched throughout the result matrix obtained. The pre-optimization study is useful in defining better initial values of design parameters, which drives most of the results within the constraint limits.

4.4. Sample Pre-Optimization

Using Figure 4.2 and Figure 4.3, a pre-optimization study can be conducted by considering the quantitative effect of each design parameter on the objectives. For this purpose, the effects of variable changes on the objectives are assumed as non-interacting. In non-interacting cases, the effect of design parameter "A" on objective "X" does not change when design parameter "B" is changed. The difference between non-interacting parameters and interacting parameters are shown in Figure 4.4. As can be seen from the figure, non-interaction assumption leads to a certain error, if the design parameters are interacting. However, in the sensitivity analysis done at section 4.3, each design parameter is varied individually, while other parameters are kept constant. It is not possible to determine interactions in such an analysis. Therefore, the results obtained in the current section, which uses non-interacting assumption, are not necessarily the final values. The approach presented is not intended to determine an optimum geometry. The combined (interacting) effects of variable changes are analyzed in the optimization study presented in the next section. The geometric values suggested with no-interaction are used to determine better initial values for the optimization study. This approach reduces the ranges of each design parameter in the optimization study. As a result, the computation time required for the optimization is decreased.
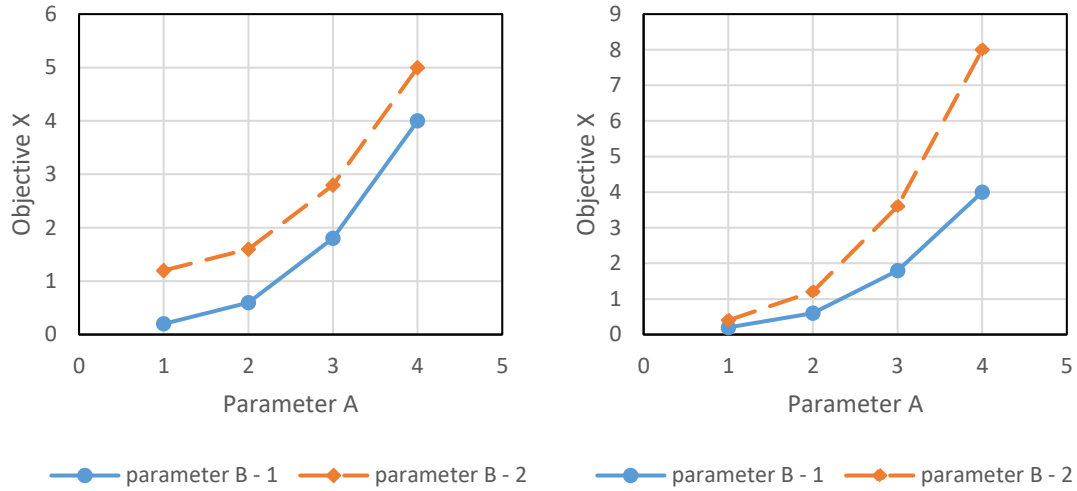
Figure 4.4. Effect of non-interacting parameters "A" and "B" on the objective "X" (on left) and interacting parameters "A" and "B" on the objective "X" (on right)

As given in Table 3.6, Q of the reference study is calculated as 14.7 W with 13.93 SLPM flow rate, which corresponds to q of 1.06 W/SLPM. In the studies which analyze the same geometry with the current study [10, 66, 73], Q values evaluated ranges mostly between 6 to 8 W. In the current study, an updated case is considered where Q limit of the IR imaging system is minimum 7.5 W.

For the working temperature, Tzabar et al. [72] studied a system, which operates with argon as the working gas, where the temperature of the system is 88 K. Similarly, Maytal et al. also mentioned a system operating with pure argon, with a working temperature of 88 K [9]. Therefore, the working temperature constraint is selected as below 88 K in the current study. The saturation pressure of argon which corresponds to 88 K saturation temperature is 1.091 bar. Therefore, the shell side pressure drop constraint in the current study is maximum 0.091 bar. The shell side pressure drop, when the geometry and working conditions given in the reference study are considered, is calculated as 0.361 bar as can be seen in Table 3.6, which corresponds to a working temperature of 90.2 K. The shell side pressure drop should be decreased by at least 74.8% to meet the constraint. As discussed in section 4.3, the tube side flow inlet pressure given in the reference study is used, which is 180 bar.

In the following study, the cooler geometry is altered using the sensitivity analysis given in section 4.3 so that Q and working temperature stays in the defined constraints. Q already fits the constraint, therefore the priority is given to decreasing the shell side pressure drop. Maximization of q allows decreasing of mass flow rate, which also decreases the shell side pressure drop considerably, as given in Table 4.2. When the current geometry is considered, a decrease of mass flow rate by 40% results in a decrease of q by almost 10% and a decrease of shell side pressure drop by almost 52%. This shows that without considering the flow rate, the shell side pressure drop may be still out of allowable limit when only changes in the geometry is considered.

Due to the no-interaction assumption in the pre-optimization, as described above, q and shell side pressure drop values have up to 10% deviation from the values calculated using the numerical model as presented in Table 4.3. This deviation is eliminated during the optimization study where the interacting effects are considered.

As discussed in section 4.3, it is advantageous to use the smallest capillary diameter which results in increased q and a slight decrease of the shell side pressure drop. The minimum capillary inner diameter analyzed in sensitivity study which does not cause diverging results is 0.22 mm. q is increased by 26% and shell side pressure drop is decreased by 4% with the change of the capillary diameter.

Among the design parameters which have transverse effects on both objectives, the parameter which provides highest decrease in the shell side pressure drop with considerably lower decrease of q is increasing the fin pitch, as discussed during sensitivity analysis. Increasing fin pitch from 0.3 mm to 0.4 mm results in a decrease of the shell side pressure drop by 31% and a decrease of q by 16%. A further decrease of fin pitch by 0.05 mm results in an additional decrease of shell side pressure drop by less than 9% and an additional decrease of q by almost 6%. It is not beneficial to further increase fin pitch above 0.4 mm. Therefore, the initial value of the fin pitch suggested for the optimization study is 0.4 mm. The combined effects of change in capillary diameter and fin pitch are increase in q by a factor of 6% and a decrease of the shell side pressure drop by 34%.

In the sensitivity analysis, it was stated that the optimum fin length value is expected to be higher than the fin length suggested in the reference study. So, the fin length should be decreased. The effect of fin length on both objectives is quite similar with the effect of fin pitch. An increase of fin length from 0.25 mm to 0.35 mm results in a decrease of shell side pressure drop by 31% and a decrease of q by less than 7.5%. A further increase of fin length by 0.05 mm results in an additional decrease of shell side pressure drop by 9% and an additional decrease of q by almost 3%. Further increasing fin length above 0.35 mm is not beneficial. Therefore, the initial value of the fin length suggested for the optimization study is 0.35 mm. The combined effects discussed above on the objectives are decrease of the q by 2% and a decrease of the shell side pressure drop by 54%.

As suggested above, the mass flow rate is decreased according to the value of q and Q constraint. Q obtained with the changes discussed above is still above the defined limit. A decrease of mass flow rate to 8 SLPM, which corresponds to a decrease of 43% results in a decrease of q by 11%. The combined effect causes a decrease in Q by 49%, which corresponds to Q equal to 7.51 W. The effect of decreasing mass flow rate to 8 SLPM on the shell side pressure drop is a decrease by 56%. Together with the changes done on the geometry, this corresponds to a total decrease of shell side pressure drop by 80%. The shell side pressure drop is calculated as 0.072 bar.

It was stated in Section 4.3 that whether the length should be increased or decreased from the value given in the reference study is not evident directly. As final Q calculated is close to the defined limit, a further decrease of length results in violation of Q constraint. The value of the length should either be kept same with the reference study, for the initial value of the optimization study or it should be increased. When the changes in the geometry suggested above are considered, it can be seen that the combined effects on the shell side pressure drop is consistent with the selected objective, which is the minimization of shell side pressure drop. In order that total changes suggested in the geometry supports both objectives, it is more beneficial to increase the initial value of length for the optimization study, without violating the shell side pressure drop constraint. As can be seen from Figure 4.2, the effect of increasing length results in an increase of q, however with a decreasing slope. On the

other hand, increasing length causes a linear increase of the shell side pressure drop. Increasing length from 50 mm to 55 mm results in a 6% increase of q and a 9% increase of the shell side pressure drop. A further increase of length by 5 mm results in a 4% increase of q with an additional 9% increase of the shell side pressure drop. Therefore, 55 mm is suggested as the initial value of the length for the optimization study.

When the fin thickness is considered, it is not beneficial to increase the value suggested in the reference study, as this results in a too little increase in q in exchange of a high increase in shell side pressure drop. On the other hand, decreasing fin thickness causes a decrease in both q and the shell side pressure drop. Q obtained is already close to the minimum allowed limit. A further decrease of q results in Q smaller than the minimum limit. In addition, the shell side pressure drop is already within the constraint limits, therefore the fin thickness should also be not decreased. In the optimization, the value suggested in the reference study is used as the initial value of the fin thickness.

The geometry suggested in the current study, in comparison with the geometry suggested in [11] is given in Table 4.3. With the no-interaction assumption, the changes in the geometry resulted in an increase of q by 4% and decrease of shell side pressure drop by 59%. The decrease of mass flow rate results in a further decrease of q by 11% and a decrease of the shell side pressure drop by 43%. The final q is estimated in the pre-optimization as 0.98 W/SLPM and the shell side pressure drop is estimated as 0.084 bar. q and the shell side pressure drop calculated using the numerical model are 0.94 W/SLPM and 0.074 bar, respectively. The values of the constraints are presented in Table 4.4 in comparison with the limiting values. The difference between values calculated from the pre-optimization and using the model is due to the no-interaction assumption. As the constraint values are within defined limits, the design parameters obtained from the pre-optimization study can be used in the optimization as initial values.

Table 4.3. *Design parameters of the JT cooler suggested as initial values for the optimization study*

Design Parameters	Suggested in [11]	Suggested in current
Length [mm]	50	55
Capillary inner diameter [mm]	0.30	0.22
Fin pitch [mm]	0.3	0.4
Fin length [mm]	0.25	0.35
Fin thickness [mm]	0.1	0.1

Table 4.4. *Values of constraints calculated in the pre-optimization and model*

Constraint	Calculated from the pre-optimization	Calculated using the model	Design limit
Q [W]	8.12	7.53	≥ 7.50
Working Temp. [K]	87.94	87.85	≤ 88

The geometry suggested with the pre-optimization study results in a lower working temperature compared with the geometry given in the reference study. This results in a shift of states 3 and 4 downwards direction when compared with the temperature – entropy graph presented in Figure 3.8. The enthalpy of state 2 found with the optimized geometry is slightly higher than the enthalpy found with the reference geometry. Moreover, enthalpy of state 4 is lower, as the working temperature is lower. Therefore, the specific cooling power is lower for the pre-optimization study. This is an expected result, due to the changes applied in order to decrease the shell side pressure drop below maximum allowable limit. The temperature – entropy graph obtained with the pre-optimized geometry is given in Figure 4.5.
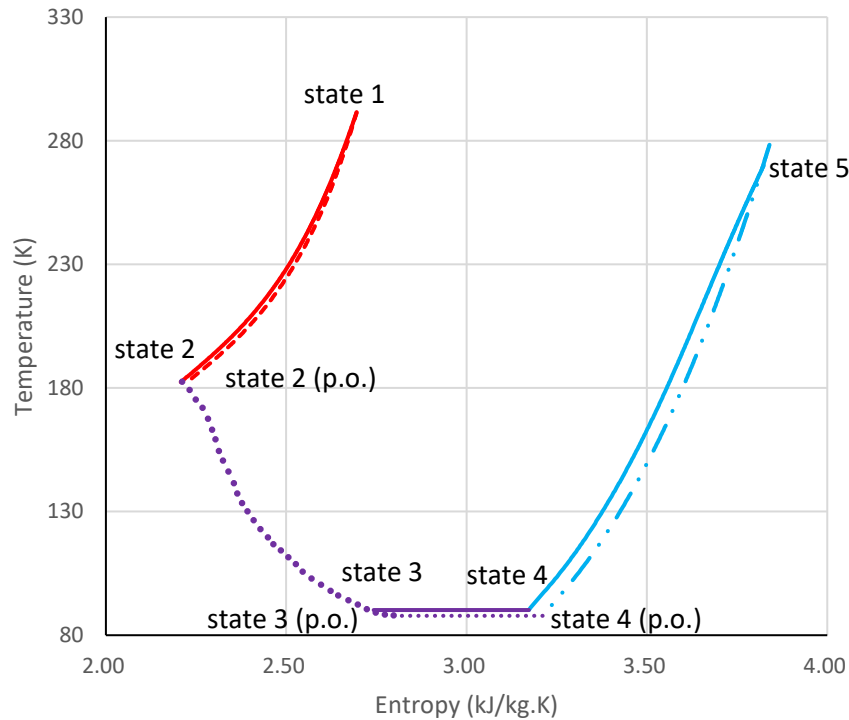
Figure 4.5. States of the cycle calculated with the geometry given in the reference study [11] and with the geometry suggested in the pre-optimization (denoted with p.o.)

A final optimization is conducted using the values suggested in Table 4.3 as initial values to find optimum values of the design parameters with respect to the defined objectives. The interactions of design parameters are considered during optimization.

4.5. Optimization Results

Once the most affecting design parameters and better initial values for every design parameter are determined, they are varied between pre-set minimum and maximum values. The initial values suggested in the pre-optimization are used as a base values. Each design parameter is varied in three levels, where the second and third values are selected a delta smaller and larger than the initial values. The values of design parameters at each level is listed in Table 4.5.

Table 4.5. *Ranges of the design parameters and flow rate analyzed in the optimization study*

Design Parameter	Min. value	Base value	Max. Value
Length [mm]	50	55	60
Capillary inner diameter [mm]	0.20	0.22	0.24
Fin pitch [mm]	0.35	0.40	0.45
Fin length [mm]	0.30	0.35	0.40
Fin thickness [mm]	0.08	0.10	0.12
Flow rate [SLPM]	7.0	7.5	8.0

The results are obtained using the numerical model with a full factorial method, where every possible combination of the design parameters and flow rate are analyzed. Total number of runs performed according to Table 4.5 is 729. Unlike the pre-optimization study, non-interacting assumption of the design parameters is not needed for the results obtained. As the numerical model is used for generating the result cloud, interacting effects of design parameters are considered, which fully reflects the system characteristic without any loss of information about the reaction of the objectives to changes made on the design parameters. The results obtained with the full factorial is presented in Figure 4.6, in comparison with the constraints. Those that fall inside the white region on the upper-left corner meet the constraints defined in section 4.4. The cases which end up with Q below 7.5 W and/or a working temperature above 88 K are filtered out and not considered during the optimization. As discussed before, the working temperature is directly related with the shell side pressure drop constraint. 88 K limit shown in Figure 4.6 corresponds to 0.091 bar maximum allowable shell side pressure drop.
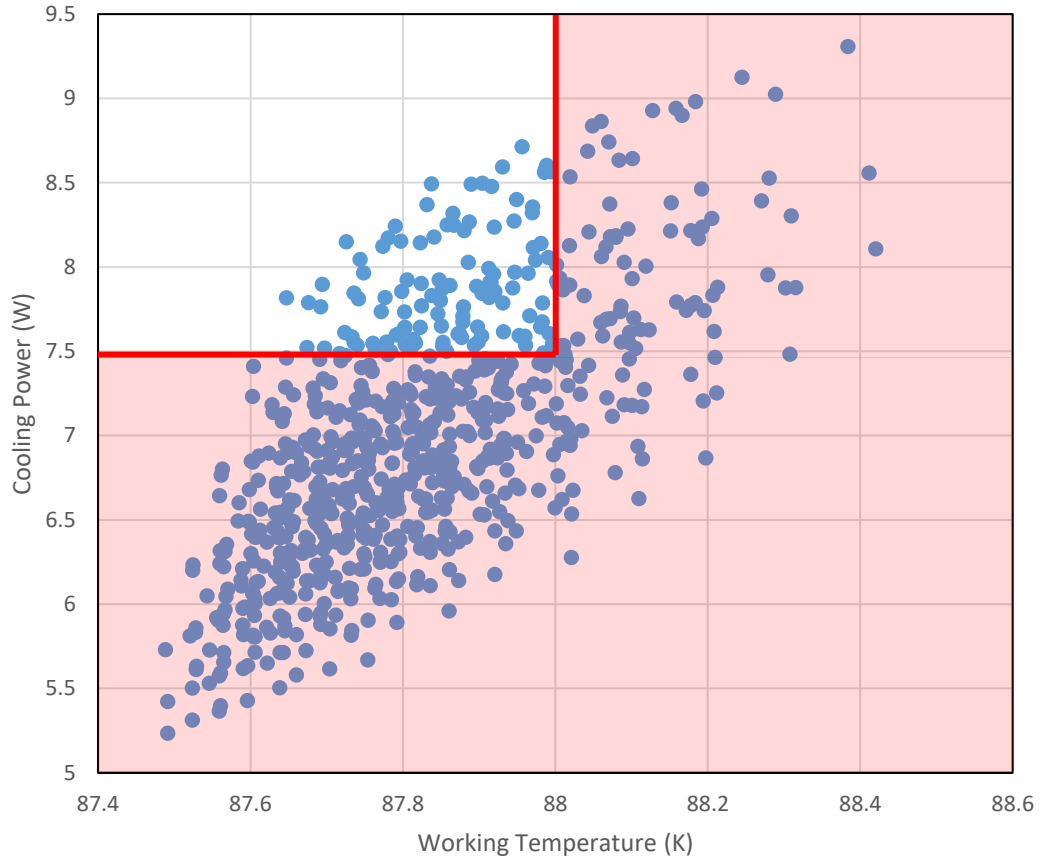
Figure 4.6. Result cloud obtained using full factorial, in comparison with the constraints

The two objectives are brought together using weighted sum method [82], in order to obtain the optimization function as

$$\varphi = w_1 \, (q)_{norm} + w_2 \left(-\Delta P_{ssf}\right)_{norm} \qquad (30)$$

where φ is the optimization function, w denotes the weights of the objectives and norm indicates that the results are normalized. The normalized shell side pressure drop has a negative sign in front because the objective is to minimize it and q is positive as the objective is to maximize it. The normalization is performed using Euclidian approach [84] as following.

$$q_{i,norm} = \frac{q_i}{\sqrt{\sum_{j=1}^{m}(q_j)^2 \big/ m}} \qquad (31)$$

where i is any q value obtained from one of the runs and m is the total number of runs, which is 729 in the current study. The weights of the objectives are determined according to the relative importance of each objective. The summation of weights must be equal to 1. The application considered in the current study, which is the IR sensor cooling, does not necessitate a relative importance of one of the objectives over the other. Therefore, the weights of both objectives are selected as 0.5 in the current analysis for case A. The effect of changing the weights is also discussed for another case, case B. The calculated optimization functions scattered according to their flow rate values, which are filtered due to the constraints can be seen in Figure 4.7.
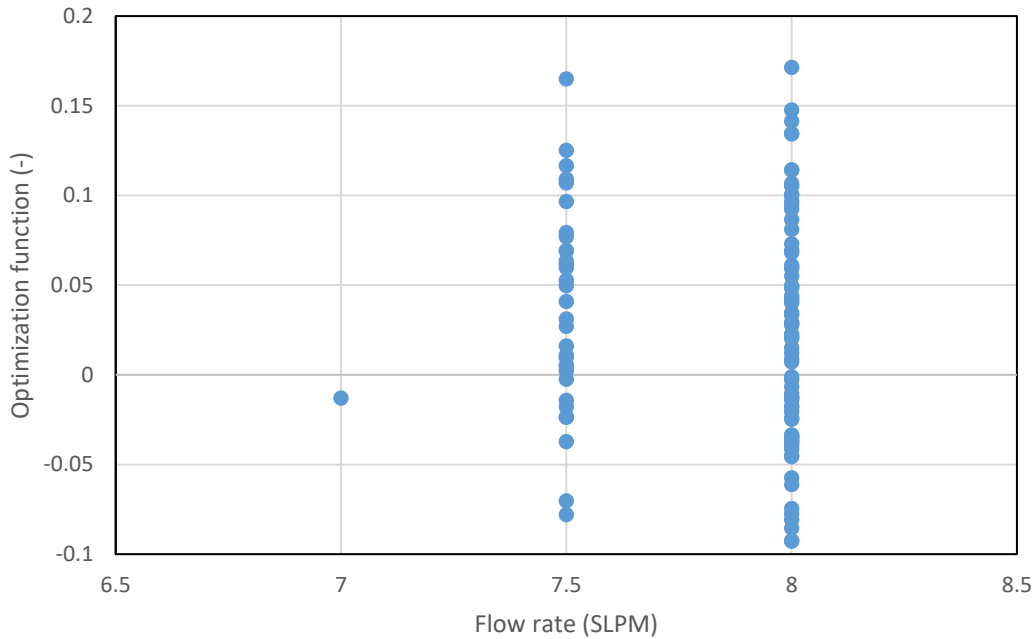
Figure 4.7. Filtered optimization functions scattered according to the flow rate values for case A

Only one geometry provided a result which is within constraints when the flow rate is 7 SLPM, in which the optimization function is lower than the results obtained with

7.5 SLPM and 8 SLPM. The details of the maximum optimization functions for each flow rate are summarized in Table 4.6, where the values of optimization function, objectives and design parameters are listed. As can be seen, the maximum value of the optimization function for 7.5 SLPM is very close to that for 8 SLPM, with a practically negligible difference. As discussed in section 4.2, operating the cooler with a lower mass flow rate is advantageous. As the value of the optimization function do not differ, the geometry suggested for 7.5 SLPM is a more preffered geometry and suggested as the optimum geometry in this study.

Table 4.6. *Maximum value of the optimization function at each flow rate, corresponding objective values and design parameters for case A*

	7 SLPM	7.5 SLPM	8 SLPM
φ [-]	-0.01	0.17	0.17
q [W/SLPM]	1.08	1.00	0.98
ΔP_{ssf} [bar]	0.087	0.055	0.052
L [mm]	60	60	60
d_{ci} [mm]	0.2	0.2	0.2
s_f [mm]	0.35	0.4	0.45
L_f [mm]	0.3	0.4	0.4
t_f [mm]	0.08	0.08	0.08

Even though the weights of the objectives are given as equal in case A, the relative effect of objectives on the optimization function are not the same. The scatter of the optimization function values with respect to the normalized q is given in Figure 4.8 and the scatter of the optimization function with respect to the normalized shell side pressure drop is given in Figure 4.9. When these two graphs are compared, it can be seen that higher values of optimization function are obtained with lower values of the shell side pressure drop in case A. On the other hand, a similar behavior cannot be seen for q, the maximum value of the optimization function is not close to the higher values of q, just on the contrary it is closer to lower values. The maximum value of normalized q does not even correspond to a high value of the optimization function.

The trend seen in Figure 4.9 is not present in Figure 4.8, where the data are scattered more arbitrarily. When analyzed in detail, it can be seen that the normalized results obtained for q varies from 1 to 1.17 with a difference of 0.17. On the other hand, the normalized results obtained for the shell side pressure drop varies from 0.7 to almost 1.3 with a difference of nearly 0.6. This shows that the effect of design parameters on q is lower, q values obtained with different combinations of design parameters are similar. On the other hand, the effect of design parameters on the shell side pressure drop is higher. Much smaller shell side pressure drop values can be achieved with changing the geometry. Therefore, when the relative importance of both objectives is equal, the optimization function tends to decrease the shell side pressure drop where a high gain could be achieved, instead of increasing q, where the gain is not significant.
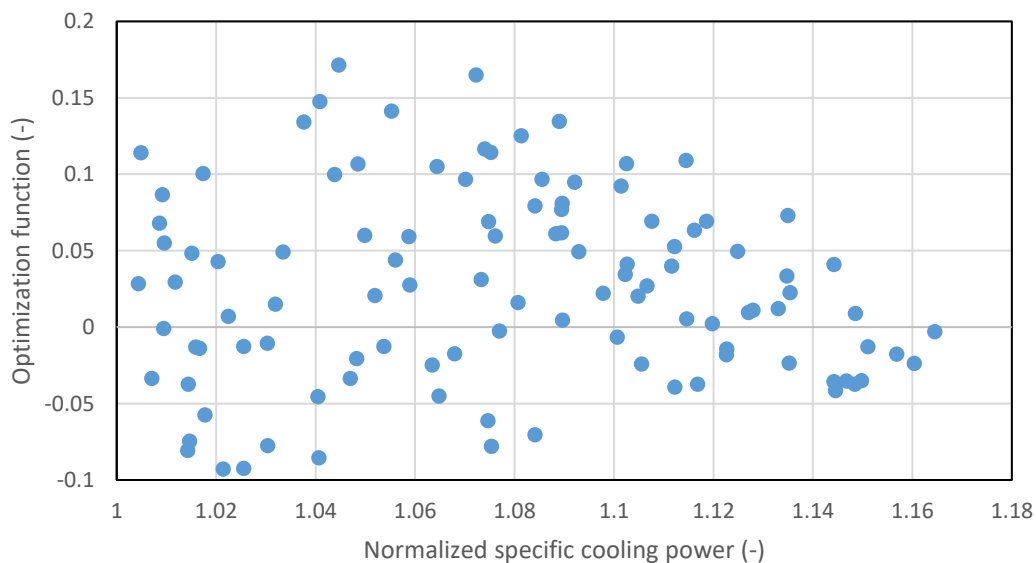
Figure 4.8. Scatter of the opt. func. with respect to the norm. q for case A
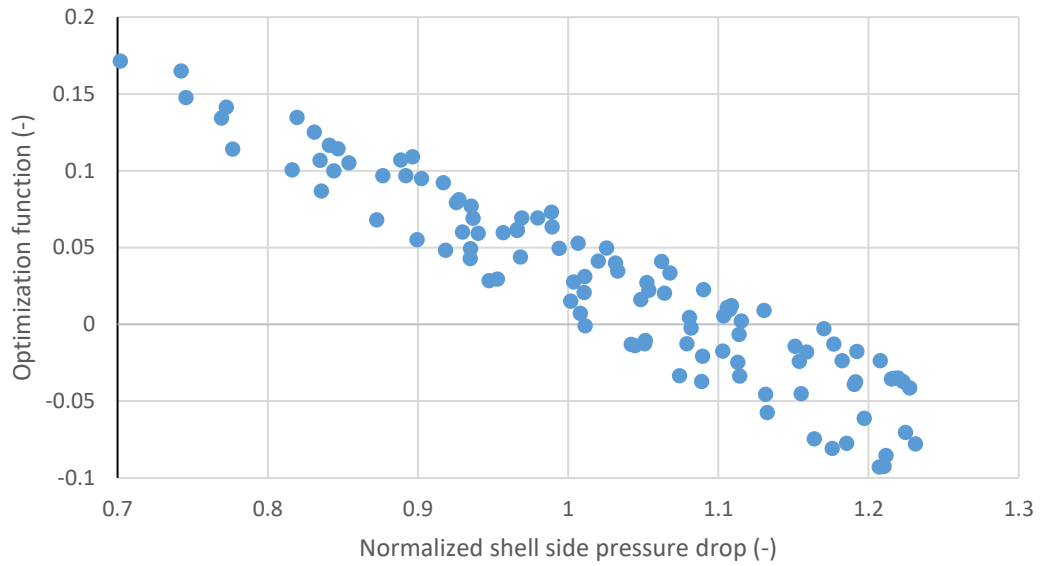
Figure 4.9. Scatter of the opt. func. with respect to the norm. shell side pressure drop for case A

When a case where the relative importance of the shell side pressure drop is higher is analyzed, it is seen that the results obtained are differ from those presented for case A. This is an expected result. As discussed above, the effect of shell side pressure drop on the final optimization function is already higher than the effect of specific cooling power. For a different case, where the relative importance of q is higher than shell side pressure drop, a different geometry is expected to be found as the optimum geometry. Therefore, a second case, case B is considered, where the weight of normalized q is 0.8 and the shell side pressure drop is 0.2. The resulting scatters of optimization function with the normalized objectives are presented in Figure 4.10 and Figure 4.11. It can be seen that both of the scattered graphs follow certain trends for case B, where higher values of optimization function are obtained for higher values of q and lower values of the shell side pressure drop.
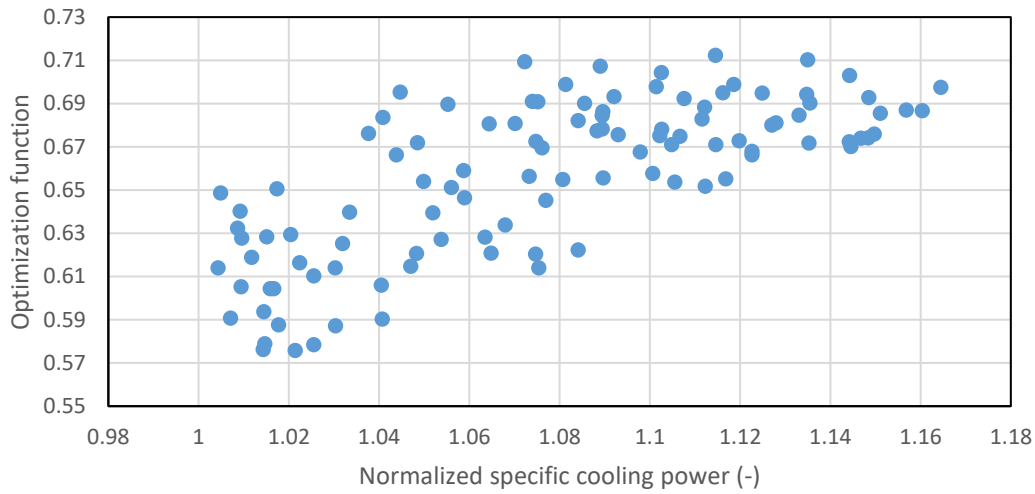
Figure 4.10. Scatter of the opt. func. with respect to the norm. q for case B
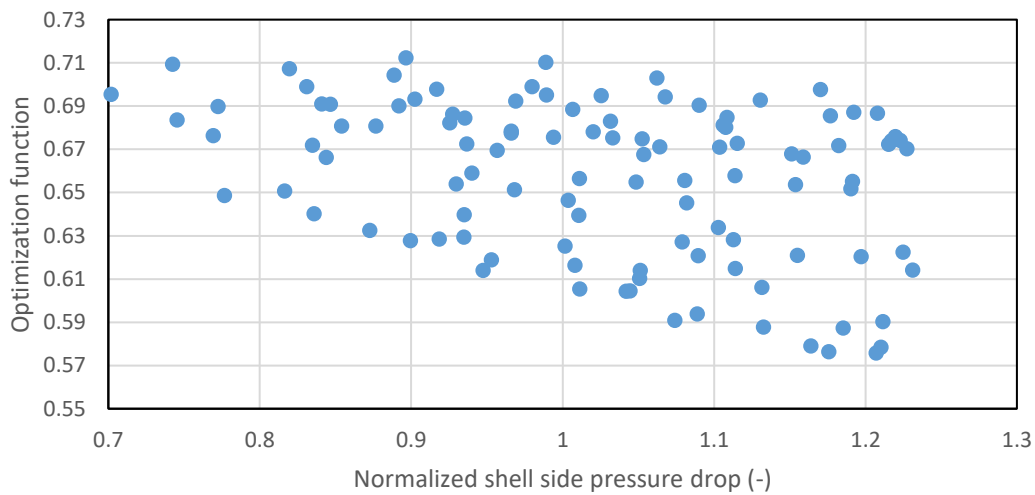
Figure 4.11. Scatter of the opt. funct. with respect to the norm. shell side pressure drop for case B

At each flow rate, Table 4.7 lists the values of the objectives and design parameters which lead to the maximum values of the optimization function for case B. As can be seen, almost the same geometry is suggested for all three flow rates. The maximum value of the optimization function is achieved at 7.5 and 8 SLPM flow rate. Since operating with lower mass flow rates is preferred, the parameter set obtained at 7.5 SLPM can be considered as the optimum.

Table 4.7. *Maximum value of the optimization function at each flow rate, corresponding objective values and design parameters for case B*

	7 SLPM	7.5 SLPM	8 SLPM
φ [-]	0.69	0.71	0.71
q [W/SLPM]	1.08	1.04	1.06
ΔP_{ssf} [bar]	0.087	0.066	0.073
L [mm]	60	60	60
d_{ci} [mm]	0.2	0.2	0.2
s_f [mm]	0.35	0.35	0.35
L_f [mm]	0.3	0.4	0.4
t_f [mm]	0.08	0.08	0.08

The comparison of the geometries suggested throughout this study are summarized in Table 4.8. As can be seen, the values suggested for some of the design parameters, such as the length, capillary inner diameter and fin thickness are found out to be in the limit of the range studied.

Table 4.8. *Design parameters and flow rate suggested throughout the optimization study and the corresponding values of the objectives*

Parameter	Suggested in [11]	Suggested in pre-opt.	Suggested in opt. case A	Suggested in opt. case B
L [mm]	50	55	60	60
$d_{c,i}$ [mm]	0.30	0.22	0.20	0.20
s_f [mm]	0.30	0.40	0.40	0.35
L_f [mm]	0.25	0.35	0.40	0.40
t_f [mm]	0.10	0.10	0.08	0.08
m [SLPM]	13.9	8	7.5	7.5
Weight of ΔP_{ssf} [-]	-	-	0.5	0.2
Weight of q [-]	-	-	0.5	0.8
q [W]	1.06	0.94	1.00	1.04
$\Delta P_{ssf\,[bar]}$	0.361	0.074	0.055	0.066

A second iteration of the optimization study, in which the ranges are updated similar to a genetic algorithm method, is useful in reaching a conclusion about the optimum geometry. The updated values are determined according to the geometry suggested for case A, where the weights of the objectives are equal. The updated ranges of the design parameters which are used in the second iteration of the optimization study are presented in Table 4.9. The fin pitch and flow rate ranges are kept the same with those in the first iteration.

Table 4.9. *Updated ranges of the design parameters which are used in the second iteration*

Design Parameter	Min. value	Base value	Max. Value
Length [mm]	50	55	60
Capillary inner diameter [mm]	0.20	0.22	0.24
Fin pitch [mm]	0.35	0.40	0.45
Fin length [mm]	0.30	0.35	0.40
Fin thickness [mm]	0.08	0.10	0.12
Flow rate [SLPM]	7.0	7.5	8.0

The result cloud obtained for the second iteration is given in Figure 4.12 in comparison with the constraints. The scaling of Figure 4.12 is selected as the same with the scaling of Figure 4.6 for better comparison of the graphs. Comparing Figure 4.6 and Figure 4.12, it can be seen that the number of combinations which give results out of the constraint limits have decreased with the update of the ranges. Especially, the number of parameters which are larger than the maximum working temperature constraint are decreased drastically. This is a consequence of the discussion which pointed out that when the weight functions are selected as equal, the effect of the shell side pressure drop objective on the optimization function is higher. Therefore, when the ranges in the second iteration are determined according to the geometry suggested with balanced weight functions, the results obtained are more in favor of the shell side pressure drop objective.
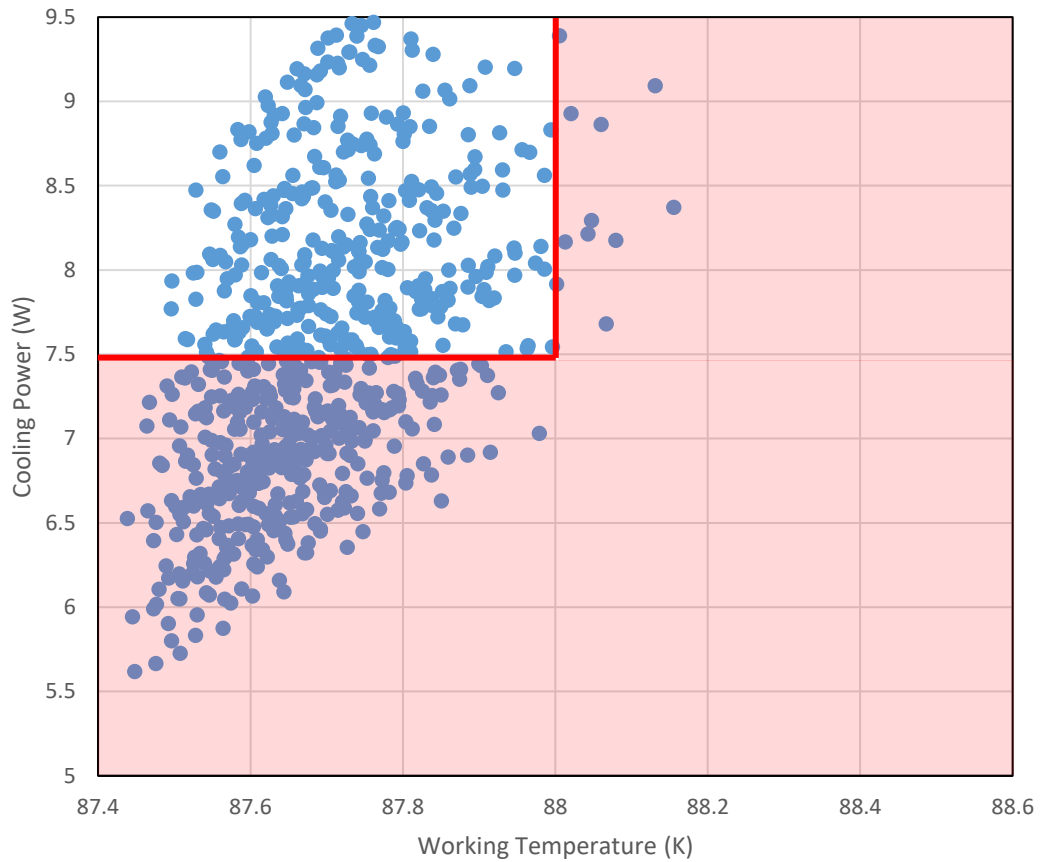
Figure 4.12. Result cloud obtained using full factorial, in comparison with the constraints for the second iteration

The effect of updating the ranges on the scatter plots of normalized objectives versus optimization functions are also similar. The plot of normalized shell side pressure drop with respect to the optimization function is almost the same for case A and case B, where the data points are randomly distributed without any increasing or decreasing characteristic. The scatter plot of the normalized q versus optimization function for case A is similar with Figure 4.8 and for case B is similar with Figure 4.10. Unlike the results obtained in the first iteration, the number of combinations which yield solutions within the constraints are increased for 7 SLPM. Moreover, the value of the optimization function that is obtained with 7 SLPM has also become comparable with those obtained with 7.5 SLPM and 8 SLPM, unlike the results presented in Figure 4.7. The results obtained for each case is summarized in Table 4.10 and Table 4.11.

Table 4.10. *Maximum value of the optimization function at each flow rate, corresponding objective values and design parameters for case A*

	7 SLPM		7.5 SLPM		8 SLPM	
	1st iter	2nd iter	1st iter	2nd iter	1st iter	2nd iter
φ [-]	-0.01	0.19	0.17	0.21	0.17	0.19
q [W/SLPM]	1.08	1.08	1.00	1.04	0.98	0.99
ΔP_{ssf} [bar]	0.087	0.040	0.055	0.035	0.052	0.035
L [mm]	60	65	60	60	60	55
d_{ci} [mm]	0.2	0.18	0.2	0.18	0.2	0.18
s_f [mm]	0.35	0.4	0.4	0.45	0.45	0.45
L_f [mm]	0.3	0.45	0.4	0.45	0.4	0.45
t_f [mm]	0.08	0.06	0.08	0.06	0.08	0.06

Table 4.11. *Maximum value of the optimization function at each flow rate, corresponding objective values and design parameters for case B*

	7 SLPM		7.5 SLPM		8 SLPM	
	1st iter	2nd iter	1st iter	2nd iter	1st iter	2nd iter
φ [-]	0.69	0.72	0.71	0.72	0.71	0.73
q [W/SLPM]	1.08	1.13	1.04	1.12	1.06	1.22
ΔP_{ssf} [bar]	0.087	0.050	0.066	0.047	0.073	0.067
L [mm]	60	60	60	60	60	65
d_{ci} [mm]	0.2	0.18	0.2	0.18	0.2	0.18
s_f [mm]	0.35	0.35	0.35	0.40	0.35	0.40
L_f [mm]	0.3	0.40	0.4	0.40	0.4	0.35
t_f [mm]	0.08	0.06	0.08	0.06	0.08	0.06

The comparison of the second iteration with the first one shows that the smallest possible capillary diameter and fin thickness results in the highest performance of the cooler. The fin thickness may be further decreased theoretically. However, it is limited by the production capabilities. Therefore, 60 μm thickness is considered as a lower limit. The minimum capillary diameter is determined by the tube side pressure drop as well as production capabilities. The minimum allowable capillary diameter is taken

as 0.18 mm. When the length of the heat exchanger is considered, 60 mm is found to be the optimum value. 65 mm length results in an increased shell side pressure drop and as a result decreases the optimization function. The fin parameters highly depend on the relative importance of the objectives. The final comparison of the results obtained for each case within the optimization study are summarized in Table 4.12. Considering case A with balanced weights of the objectives, the final flow rate suggested is decreased by 46% and the shell side pressure drop is decreased by 90%.

Table 4.12. *Design parameters and flow rate suggested throughout the optimization study and the corresponding values of the objectives*

Parameter	Reference study [11]	Pre-opt.	Opt. case A, 1st iter	Opt. case A, 2nd iter	Opt. case B, 1st iter	Opt. case B, 2nd iter
L [mm]	50	55	60	60	60	60
$d_{c,i}$ [mm]	0.30	0.22	0.20	0.18	0.20	0.18
s_f [mm]	0.30	0.40	0.40	0.45	0.35	0.35
L_f [mm]	0.25	0.35	0.40	0.45	0.40	0.40
t_f [mm]	0.10	0.10	0.08	0.06	0.08	0.06
m [SLPM]	13.9	8	7.5	7.5	7.5	7
Weight of ΔP_{ssf} [-]	-	-	0.5	0.5	0.2	0.2
Weight of q [-]	-	-	0.5	0.5	0.8	0.8
q [W/SLPM]	1.06	0.94	1.00	1.04	1.04	1.13
$\Delta P_{ssf\,[bar]}$	0.361	0.074	0.055	0.035	0.066	0.050

Even though maximization of specific cooling power is an objective, the final value obtained with the optimum geometry is lower than the initial value calculated using the reference geometry [11], as given in Table 4.12. This is because the shell side pressure drop calculated with the reference geometry is higher than the constraint. The geometry changes applied to decrease the shell side pressure drop resulted in a lower specific cooling power. In addition, the flow rate is decreased, which also caused the specific cooling power to decrease. The optimization procedure resulted in a both higher specific cooling power and lower shell side pressure drop, as can be seen from Table 4.12.

The enthalpy of state 2 calculated with the optimum geometry is very close to the enthalpy of state 2 found with the reference geometry. Temperatures of states 3 and 4 are lower due to the decreased shell side pressure drop. Enthalpy of state 4 calculated with the optimum geometry is slightly lower than the enthalpy of state 4 found with the reference geometry. The temperature – entropy chart calculated using the optimum geometry, in comparison with the reference geometry is given in Figure 4.13.
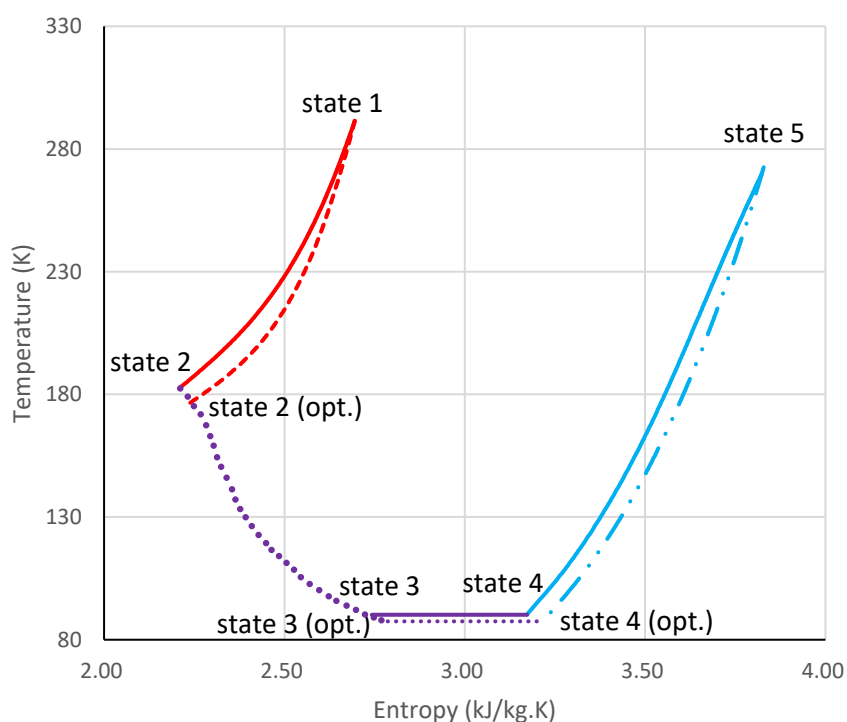

Figure 4.13. States of the cycle calculated with the geometry given in the reference study [11] and with the geometry suggested in the optimization (denoted with opt.)

CHAPTER 5

CONCLUSION

5.1. Summary and Conclusion

A JT cryocooler is analyzed in this study through a 1D numerical model built. The simplified one-dimensional, steady state forms of linear momentum and energy conservation equations are discretized using finite difference method and solved numerically. The developed model is first tested against similar numerical studies available in the literature, with results being in good agreement. Then the model is enhanced with several modifications. The commonly made mistake of using a tube side friction correlation that is not consistent with the corresponding momentum equation is corrected, resulting in 81% decrease in the tube side flow pressure drop. The correction also allowed to get a positive and meaningful cooling load. As the second modification, the effect of pressure change on the enthalpy is included in the energy equations of the working fluid. This modification resulted in 6% decrease in tube side flow pressure drop and 33% increase in cooling load. Collins tubing correlation is employed for the first time for the calculation of shell side flow friction coefficient due to geometric similarities. This resulted in an increase of Q by 8.9% and shell side flow pressure drop increase by 167%. The inlet pressure and temperature of the shell side flow are redefined so that an optimization study can be carried out as desired without being constrained with the limited number of experimentally studied configurations available in the literature. In addition, the temperature dependence of shield emissivity is considered.

After all modifications are applied and the numerical model of the heat exchanger is finalized, an optimization study performed. The objectives of the optimization function are selected as maximization of q and minimization of the shell side pressure drop. According to the application area, constraints of the optimization are specified. The first constraint is to have the final value of Q above 7.5 W. The second constraint is to have a working temperature below 88 K, which corresponds to a shell side pressure drop of 0.091 bar. This value is reported as the working temperature of a JT cooler which is operated with argon [9]. With maximization of q, the flow rate can be

decreased while Q constraint is still satisfied. This allows to operate the JT cooler for a longer time when fed from a constant gas source.

To see the effects of each design parameter on the selected objectives, a sensitivity analysis is performed. The effect of selected six design parameters, which are heat exchanger length, finned capillary inner diameter, finned capillary wall thickness, fin pitch, fin length and fin height, on objectives are studied by performing controlled numerical tests. The results of these numerical tests are normalized with the geometry given in the reference study and presented in graphs showing relative effects of each design parameter on an objective, by assuming the design parameters are not interacting. These graphs are used in a pre-optimization study where better initial values of each design parameter are determined for the optimization. It is shown that the objectives are not highly sensitive to the capillary wall thickness, therefore this parameter can be eliminated during the optimization. By determining better initial values, the need to vary the design parameters in higher levels and larger ranges is ceased. Therefore, the process time of the optimization study is decreased. The geometry suggested with the pre-optimization study is obtained by non-interacting assumption, so a final optimization step is required which considers the interacting effects of the design parameters.

To perform the optimization, first the ranges and number of levels through which the design parameters are varied, are determined. Using the numerical model built, a result cloud is obtained using full factorial method, for every possible combination of the design parameters and flow rate. Second, an optimization function is built using the two objectives. Relative importance of each objective is defined by weights. Two different cases are studied which have different weights. In the first case the weights of both objectives are equal. In the second case, q has a higher importance and as a result higher weight over the shell side pressure drop. The objectives are normalized using Euclidian approach to be used within the optimization function. Once the value of the optimization function is calculated for every combination across the result cloud, the maximum value is determined using grid search method. The geometry for the maximum value of the optimization function is reused as an initial value for a

second optimization iteration. The results obtained from the first iteration and second iteration are compared and the optimum geometry is determined.

From the final geometry suggested in the current study, the shell side pressure drop is decreased by 90% and the flow rate is decreased by 46%. The operation time is expected to increase by almost 2 times. The numerical model built in this study and the optimization procedure suggested is capable of optimizing the cooler geometry with respect to selected objectives and for different cases where relative importance of each objective is different.

5.2. Future Work

There are some aspects of the study which can be further improved in future studies. These studies are listed below.

- Mostly bank of inline tubes correlation is used for heat transfer correlation of the shell side flow, which is also the case in the current study. Moreover, different shell side friction correlations are used in literature and suggested in the current study. A detailed analysis specifically for the shell side of the JT cryocoolers investigated in the current study, should be performed to develop shell side friction and heat transfer correlations, which comprises both numerical and experimental studies.

- In the current study, forward differencing and backward differencing equations are implemented as boundary conditions at hot end and cold end of the heat exchanger, as an alternative to the boundary conditions discussed in section 3.4. This approach is suggested because it is physically more meaningful. However, it resulted in a diverging solution at high mesh numbers and only allowed low mesh numbers. Moreover, the results obtained with both approaches are quite similar with insignificant deviations. The divergence of the model is probably due to a numerical problem. The cause of this numerical problem may be further analyzed and solved.

- As discussed before, the cooldown time of the JT cooler is a significant advantage and therefore, an important objective. To analyze the cooldown time, the time dependent terms shall be considered within the differential

equations. The model can be further developed by adding time dependent terms and redefining the boundary conditions.

- It is seen in literature that most of the recent studies are on gas mixtures and applications where gas mixtures are used. By building a new code for thermophysical properties of gas mixtures, the numerical model and optimization model built in the current study can be used for an application where gas mixture is used.

- In the current study, objectives are selected according to the cooler system and the analysis is done considering the details of the heat exchanger. The code can be further extended to include platform level parameters and analyze platform level objectives.

REFERENCES

[1] H. S. Cao, A. V. Mudaliar, J. H. Derking, P. P. P. M. Lerou, H. J. Holland, D. R. Zalewski, S. Vanapalli, H. J. M. ter Brake. *Design and optimization of a two-stage 28 K Joule-Thomson microcooler.* Cryogenics 52 (2012)

[2] N. Tzabar, A. Kaplansky. *A numerical cool-down analysis for Dewar-detector assemblies cooled with JT cryocoolers.* International Journal of Refrigeration 44, (2014)

[3] M.D. Atrey. *Thermodynamic analysis of Collins helium liquefaction cycle.* Cryogenics 38 (1998)

[4] P.K. Gupta, P.K. Kush, A. Tiwari. *Second law analysis of counter flow cryogenic heat exchangers in presence of ambient heat-in-leak and longitudinal conduction through wall.* International Journal of Heat and Mass Transfer 50 (2007)

[5] P.M. Ardhapurkar, A. Sridharan, M.D. Atrey. *Experimental investigation on temperature profile and pressure drop in two-phase heat exchanger for mixed refrigerant Joule-Thomson cryocooler.* Applied Thermal Engineering 66 (2014)

[6] E. D. Marquardt, R. Radebaugh, J. Dobak. *A cryogenic catheter for treating heart arrhythmia.* Advances in Cryogenic Engineering 43 (1998)

[7] L. Jin, C. Lee, S. Baek, S. Jeong. *Design og high-efficiency Joule-Thomson cycles for high-temperature superconductor power cable cooling.* Cryogenics 93 (2018)

[8] R. Levenduski, R. Scarlotti. *Joule-Thomson cryocooler for space applications.* Cryogenics 36 (1996)

[9] B.Z. Maytal, J.M. Pfotenhauer. *Miniature Joule-Thomson Cryocooling – Principles and Practice.* Springer, New York (2013)

[10] R.M. Damle, M.D. Atrey. *The cool-down behavior of a miniature Joule-Thomson (J-T) cryocooler with distributed J-T effect and finite reservoir capacity.* Cryogenics 71 (2015)

[11] K.C. Ng, H. Xue, J.B. Wang. *Experimental and numerical study on a miniature JT cooler for steady-state characteristics.* Int Journal of Heat and Mass Transfer 45 (2002)

[12] K.D. Timmerhaus, T.M. Flynn. *Cryogenic Process Engineering.* Plenum Press, New York, USA (1989)

[13] E. W. Lemmon, R. T. Jacobsen. *Viscosity and thermal conductivity equations for nitrogen, oxygen, argon and air.* International Journal of Thermophysics 25 (2004)

[14] R. B. Stewart, R. T. Jacobsen. *Thermodynamic properties of argon from the triple point to 1200 K with pressure to 1000 MPa.* Journal of Physics and Chemistry Reference Data 18 (1989)

[15]   D. L. Shumaker, J. T. Wood, C. R. Thacker. *Infrared Imaging Systems Analysis.* ERIM Series in Infrared & Electro-Optics, Environmental Research Instittute of Michigan (1993)

[16]   G. Kastberger, R. Stachl. *Infrared imaging technology and biological applications.* Behavior Research Methods, Instruments & Computers 35 (2003)

[17]   R. F. Barron. Cryogenic Systems. Oxford University Press, New York (1985)

[18]   M. F. Modest. *Radiative Heat Transfer.* Academis Press (2013)

[19]   A. Rogalski. *Progress in focal plane array technologies.* Progress in Quantum Electronics 36 (2012)

[20]   F. P. Incropera, D. P. Dewitt, T. L. Bergman, A. S. Lavine. *Fundamentals of Heat and Mass Transfer.* John Wiley and Sons (2007)

[21]   A. Rogalski. *Infrared Detectors.* CRC Press, USA (2011)

[22]   S.C. Stotlar. *Electro-Optics Handbook, Second Edition, Chapter 17: Infrared Detectors.* McGraw-Hill (2000)

[23]   R. Radebaugh. *Cryocoolers: the state of the art and recent developments.* J. Phys.: Condens. Matter 21 (2009)

[24]   S.B. Campana. *The Infrared & Electro-Optical Systems Handbook, Volume 5: Passive Electro-Optical Systems.* Infrared Information Analysis Center, Environmental Research Institute of Michigan (1993)

[25]   G. Walker, E.R. Bingham. *Low-Capacity Cryogenic Refrigeration.* Oxford University Press, New York (1994)

[26]   W.V. Hassenzahl, D.W. Hazelton, B.K. Johnson, P. Komarek, M. Noe, C.T. Reis. *Electric Power Applications of Superconductivity.* Proceedings of the IEEE, Vol. 92 (2004)

[27]   M. Kanoglu, I. Dincer, Rosen MA. *Performance analysis of gas liquefaction cycles.* Int J Energy Res 32 (2008)

[28]   J.C. Pacio, C.A. Dorao. *A Review on Heat Exchanger Thermal Hydraulic Models for Cryogenic Applications.* Cryogenics 51 (2011)

[29]   S. Kakac, H. Liu. *Heat Exchangers: Selection, Rating and Thermal Design.* CRC Press, New York (2002)

[30]   G. Walker. *Cryocoolers Part 2: Applications.* Plenum Press, New York (1983)

[31]   X. G. Hao, S. H. Yao, T. Schilling. *Design and experimental investigation of the high efficienct 1.5 W/4.2 K pneumatic-drive g-m cryocooler.* Cryogenics 70 (2015)

[32]   R.M. Damle, M.D. Atrey. *Transient simulation of a miniature Joule-Thomson (J-T) cryocooler with and without the distributed J-T effect.* Cryogenics 65 (2015)

[33]   R. Radebaugh. *Refrigeration for Superconductors*. Proceedings of the IEEE, Vol 92, No 10 (2004)

[34]   J.P. Kelley. *Applications of Cryogenic Technology, Volume 10*. Plenum Press, New York (1991)

[35]   H.M. Chang, K.H. Gwak. *New Application of Plate-Fin Heat Exchanger with Regenerative Cryocoolers*. Cryogenics 70 (2015)

[36]   R.S. Bhatia, S.T. Chase, W.C. Jones, B.G. Keating, A.E. Lange, P.V. Mason, B.J. Philhour, G. Sirbi. *Closed cycle cooling of infrared detectors to 250 mK*. Cryogenics 42 (2002)

[37]   G. Venkatarathnam, S. Sarangi. *Matrix heat exchangers and their application in cryogenic systems*. Cryogenics 30 (1990)

[38]   M.J. Nilles, M.E. Calkins, M.L. Dingus, J.B. Hendricks. *Heat Transfer and Flow Friction in Perforated Plate Heat Exchangers*. Experimental Thermal and Fluid Science 10 (1995)

[39]   P. Ramesh, G. Venkatarathnam. *Transient response of perforated plate matrix heat exchangers*. Cryogenics 38 (1998)

[40]   G. Venkatarathnam. *Effectiveness-NTU relationship in perforated plate matrix heat exchangers*. Cryogenics 36 (1996)

[41]   Z. Jianqin, L. Shaopeng. *Numerical studies of an eccentric tube-in-tube helically coiled heat exchanger for IHEP-ADS helium purification system*. Chinese Physics C (2014)

[42]   Y. Zhou, J. Yu, X. Chen. *Thermodynamic optimization analysis of a tube-in-tube helically coiled heat exchanger for Joule-Thomson refrigerators*. International Journal of Thermal Sciences 58 (2012)

[43]   G. Hwang, S. Jeong. *Pressure loss effect on recuperative heat exchanger and its thermal performance*. Cryogenics 50 (2010)

[44]   J. Guichard, A. Cottereau, D. Chazot. *Cryogenic characterization of low cost Joule-Thomson coolers*. Proceedings of SPIE Vol 4130 (2000)

[45]   J.R. Lines. *Helically Coiled Heat Exchangers Offer Advantages*. Graham Manufacturing Co. Inc. (1998)

[46]   J. Mitrovic. *Heat Exchangers: Basic Design Applications*. Intech (2012)

[47]   V. Kumar, S. Saini, M. Sharma, K.D.P. Nigam. *Pressure drop and heat transfer study in tube-in-tube helical heat exchanger*. Chemical Engineering Science 61 (2006)

[48]   Y.J. Hong, S.J. Park, Y.D. Choi. *Effect of Heat Exchanger Configuration on the Performance of Joule-Thomson Refrigerators*. Cryocoolers 16 (2011)

[49]   R.G. Hansen. *Current and Projected State of Joule-Thomson Cooling Technology*. Proceedings of SPIE Vol. 2746 (1996)

[50]   A. Charnley, G.L. Isles, J.R. Townley. *The direct measurement of the isothermal Joule-Thomson coefficient for gases.* Proceedings of the Royal Society of London. Series A, Mathematical and Physical Sciences, Vol. 218 (1953)

[51]   A. Jaques. *Thermophysical Properties of Argon.* Fermilab D0 EN-3740.512-EN-142 (1988)

[52]   D.W. McClure. *The Joule-Thomson Coefficient – A Molecular Interpretation.* Am. J. Phys. 39 (1971)

[53]   R.T. Jacobsen, S.G. Penoncello, E.W. Lemmon. *Thermodynamic Properties of Cryogenic Fluids.* Springer Science, New York (1997)

[54]   F.C. Chou, C.F. Pai, S.B. Chien, J.S. Chen. *Preliminary Experimental and Numerical Study of Transient Characteristics for a JT Cryocooler.* Cryogenics 35, (1994)

[55]   B.Z. Maytal. *Maximizing production rates of the Linde-Hampson machine.* Cryogenics 46 (2006)

[56]   F. C. Chou, S. M. Wu, C. F. Pai. *Prediction of final temperature following Joule-Thomson expansion of nitrogen gas.* Cryogenics 33 (1993)

[57]   H. Saygın, A. Şişman. *Joule-Thomson coefficients of quantum ideal-gases.* Applied Energy 70 (2001)

[58]   B. Z. Maytal. *Post-isenthalpic expansion temperature.* Cryogenics 35 (1995)

[59]   B. Z. Maytal, A. Shavit. *On the Joule-Thomson integral inversion curves of quantum gases.* Cryogenics 37 (1997)

[60]   S.B. Chien, L.T. Chen, F.C. Chou. *A study on the transient characteristics of a self-regulating Joule-Thomson cryocooler.* Cryogenics 36 (1996)

[61]   S.B. Chien, L.T. Chen. *Two-phase coexistence analysis of the bellows control mechanism for a J-T cryocooler.* Cryogenics 39 (1999)

[62]   P. Gupta, M.D. Atrey. *Performance evaluation of counter flow heat exchangers considering the effect of heat in leak and longitudinal conduction for low-temperature applications.* Cryogenics 40 (2000)

[63]   P.K. Gupta, P.K. Kush, A. Tiwari. *Experimental research on heat transfer coefficients for cryogenic cross-counter-flow coiled finned-tube heat exchangers.* Int. Journal of Refrigeration 32 (2009)

[64]   P. K. Gupta, P. K. Kush, A. Tiwari. *Experimental studies on pressure drop characteristics of cryogenic cross-counter flow coiled finned-tube heat exchangers.* Cryogenics 50 (2010)

[65]   H. Xue, K. C. Ng, J.B. Wang. *Performance evaluation of the recuperative heat exchanger in a miniature JT cooler.* Applied Thermal Engineering 21 (2001)

[66]   H.T. Chua, X.L. Wang, K.C. Ng. *A numerical study of the Hampson-type miniature Joule-Thomson cryocooler.* Int. J. of Heat and Mass Transfer 49 (2006)

[67]   B. Maytal. *Cool-down periods similarity for a fast Joule-Thomson cryocooler.* Cryogenics 32 (1992)

[68]   B.Z. Maytal. *Performance of ideal flow regulated Joule-Thomson cryocooler.* Cryogenics 34 (1994)

[69]   Y.J. Hong, S.J. Park, H.B. Kim, Y.D. Choi. *The cool-down characteristics of a miniature Joule-Thomson refrigerator.* Cryogenics 46 (2006)

[70]   Y.J. Hong, S.J. Park, Y.D. Choi. *A Numerical Study of the Performance of a Heat Exchanger for a Miniature Joule-Thomson Refrigerator.* Cryocoolers 15 (2009)

[71]   Y.J. Hong, S.J. Park, Y.D. Choi. *A numerical study on operating characteristics of a miniature Joule-Thomson refrigerator.* Superconductivity and Cryogenics 12 (2010)

[72]   N. Tzabar, I. Lifshiz, A. Kaplansky. *Fast Cool-down J-T Cryocooler to 88 K.* Advances in Cryogenic Engineering: Transactions of the Cryogenic Engineering Conference Vol. 53 (2008)

[73]   P.M Ardhapurkar, M.D. Atrey. *Performance optimization of a miniature Joule-Thomson cryocooler using numerical model.* Cryogenics 63 (2014)

[74]   Y. Liu, L. Liu, L. Liang, X. Liu, J. Li. *Thermodynamic optimization of the recuperative heat exchanger for Joule-Thomson cryocoolers using response surface methodology.* Int. J. of Refrigeration 60 (2015)

[75]   F. Can, A. B. Erdoğmuş, M. Baki, M. K. Aktaş. *Cooling characterization of conceptual Joule-Thomson cryogenic cooler.* International Conference of Cryogenics and Refrigeration Technology, 22-25 June 2016, Bucharest, Romania

[76]   S. I. Woods, T. M. Jung, D. R. Sears, J. Yu. *Emissivity of silver and stainless steel from 80 K to 300 K: Application to ITER thermal shields.* Cryogenics 60 (2014)

[77]   B. R. Munson, D. F. Young, T. J. Okiishi, W. W. Huebsch. *Fundamentals of Fluid Mechanics.* John Wiley and Sons Inc (2009)

[78]   V. Glazar, M. Percic, G. Marunic, B. Frankovic. *A comparative study of evolutionary and search algorithms for optimization of heat exchanger with microchannel coil.* Transactions of Famena XL – Special issue I (2016)

[79]   A. L. H. Costa, E. M. Queiroz. *Design optimization of shell-and-tube heat exchangers.* Applied Thermal Engineering 28 (2008)

[80]   M. Mishra, P. K. Das, S. Sarangi. *Second law based optimization of crossflow plate-fin heat exchanger design using genetic algorithm.* Applied Thermal Engineering 29 (2009)

[81]   A. Hadidi. *Biogeography-Based Optimization Algorithm for Optimization of Heat Exchangers.* In: J. Valadi, P. Siarry (eds) Applications of Metaheuristics in Process Engineering. Springer, Cham

[82]   H. R. E. H. Bouchekara, A. Kedous-Lebouc, J. P. Yonnet, C. Chillet. *Multiobjective optimization of AMR system.* International Journal of Refrigeration 37 (2014)

[83]   M. Cavazzuti. *Optimization Methods: From Theory to Design.* Springer (2013)

[84]   R. Kumar, S. C. Kaushik, R. Kumar, R. Hans. *Multi-objective thermodynamic optimization of an irreversible regenerative Brayton cycle using evolutionary algorithm and decision making.* Ain Shams Eng J (2015)

[85]   G. Türkakar, T. Okutucu-Özyurt. *Dimensional optimization of microchannel heat sinks with multiple heat sources.* International J of Thermal Sciences 62 (2012)

APPENDICES

APPENDIX A

DERIVATION OF DIFFERENTIAL EQUATIONS

The problem is analyzed through infinitesimal volume elements. Both tube side and shell side flows are studied in cylindrical coordinates. Conservation of mass, momentum and energy equations are written for the infinitesimal volume element, which are integrated in r and Θ directions. Through the assumptions validated before, the equations are simplified into 1D equations. The simplified equations are solved at each element in x direction to find the temperature, pressure and velocity distribution of the tube and shell side flows. V_x, V_r, V_Θ denote the velocity in x, r and Θ directions, respectively.

Continuity equation:

$$
\begin{aligned}
\rho\, V_x\, r\, \partial\theta\, \partial r + \rho\, V_r\, r\, \partial\theta\, \partial x &+ \rho\, V_\theta\, \partial r\, \partial x - \frac{\partial\, (\rho\, r\, \partial\theta\, \partial r\, \partial x)}{\partial t} \\
&= \left[\rho\, V_x\, r\, \partial\theta\, \partial r + \frac{\partial\, (\rho\, V_x\, r\, \partial\theta\, \partial r)}{\partial x}\, \partial x \right] \\
&+ \left[\rho\, V_r\, r\, \partial\theta\, \partial x + \frac{\partial(\rho\, V_r\, r\, \partial\theta\, \partial x)}{\partial r}\, \partial r \right] \\
&+ \left[\rho\, V_\theta\, \partial r\, \partial x + \frac{\partial(\rho\, V_\theta\, \partial r\, \partial x)}{\partial\theta}\, \partial\theta \right]
\end{aligned}
\tag{A.1}
$$

Simplifying (A.1),

$$-\frac{\partial}{\partial t}(\rho)\, r\, (\partial\theta\,\partial r\,\partial x)$$

$$= \frac{\partial}{\partial x}(\rho\, V_x)\, r\, (\partial\theta\,\partial x\,\partial r) + \frac{\partial}{\partial r}(\rho\, V_r\, r)(\partial\theta\,\partial x\,\partial r) \qquad \text{(A.2)}$$

$$+ \frac{\partial}{\partial\theta}(\rho\, V_\theta)(\partial\theta\,\partial x\,\partial r)$$

$$-\frac{\partial\rho}{\partial t}\, r = \frac{\partial(\rho\, V_x)}{\partial x}\, r + \frac{\partial(\rho\, V_r)}{\partial r}\, r + (\rho\, V_r) + \frac{\partial(\rho\, V_\theta)}{\partial\theta} \qquad \text{(A.3)}$$

Momentum equation in *x* direction:

$$\rho\, V_x\, r\, \partial\theta\,\partial r\, V_x + \rho\, V_r\, r\, \partial\theta\,\partial x\, V_x + \rho\, V_\theta\, \partial r\, \partial x\, V_x$$

$$+ \left[\sigma_{xx}\, r\, \partial\theta\,\partial r + \frac{\partial(\sigma_{xx}\, r\, \partial\theta\,\partial r)}{\partial x}\, \partial x\right]$$

$$+ \left[\tau_{\theta x}\, \partial x\, \partial r + \frac{\partial(\tau_{\theta x}\, \partial x\,\partial r)}{\partial\theta}\, \partial\theta\right]$$

$$+ \left[\tau_{rx}\, r\, \partial\theta\,\partial x + \frac{\partial(\tau_{rx}\, r\, \partial\theta\,\partial x)}{\partial r}\, \partial r\right] - \frac{\partial\,(\rho\, V_x\, r\, \partial\theta\,\partial r\,\partial x)}{\partial t}$$

$$= \left[\rho\, V_x\, r\, \partial\theta\,\partial r\, V_x + \frac{\partial\,(\rho\, V_x\, r\, \partial\theta\,\partial r\, V_x)}{\partial x}\, \partial x\right] \qquad \text{(A.4)}$$

$$+ \left[\rho\, V_r\, r\, \partial\theta\,\partial x\, V_x + \frac{\partial(\rho\, V_r\, r\, \partial\theta\,\partial x\, V_x)}{\partial r}\, \partial r\right]$$

$$+ \left[\rho\, V_\theta\, \partial r\, \partial x\, V_x + \frac{\partial(\rho\, V_\theta\, \partial r\,\partial x\, V_x)}{\partial\theta}\, \partial\theta\right] + \sigma_{xx}\, r\, \partial\theta\,\partial r$$

$$+ \tau_{rx}\, r\, \partial\theta\,\partial x + \tau_{\theta x}\, \partial r\, \partial x - \rho\, f_x\, r\, \partial r\, \partial\theta\,\partial x$$

Simplifying (A.4),

$$\frac{\partial}{\partial x}(\sigma_{xx})\, r\, \partial\theta\,\partial r\,\partial x + \frac{\partial}{\partial\theta}(\tau_{\theta x})\, \partial x\,\partial r\,\partial\theta + \frac{\partial}{\partial r}(\tau_{rx}\, r)\, \partial\theta\,\partial x\,\partial r$$

$$- \frac{\partial}{\partial t}\,(\rho\, V_x\, r\, \partial\theta\,\partial r\,\partial x) \qquad \text{(A.5)}$$

$$= \frac{\partial}{\partial x}(\rho\, V_x{}^2)r\, \partial\theta\,\partial r\,\partial x + \frac{\partial}{\partial r}(\rho\, V_r\, r\, V_x)\, \partial\theta\,\partial x\,\partial r$$

$$+ \frac{\partial}{\partial\theta}(\rho\, V_\theta\, V_x)\, \partial r\,\partial x\,\partial\theta - \rho\, f_x\, r\, \partial r\,\partial\theta\,\partial x$$

The model is studied at steady state. The time derivatives are zero.

Continuity equation:

$$\frac{\partial(\rho\,V_x)}{\partial x} + \frac{\partial(\rho\,V_r)}{\partial r} + \frac{(\rho\,V_r)}{r} + \frac{\partial(\rho\,V_\theta)}{r\,\partial\theta} = 0 \tag{A.6}$$

Momentum equation:

$$\begin{aligned}
\frac{\partial}{\partial x}(\sigma_{xx})\,r\,\partial\theta\,\partial r\,\partial x &+ \frac{\partial}{\partial\theta}(\tau_{\theta x})\,\partial x\,\partial r\,\partial\theta + \frac{\partial}{\partial r}(\tau_{rx})\,r\,\partial\theta\,\partial x\,\partial r \\
&+ \tau_{rx}\,\partial\theta\,\partial x\,\partial r \\
&= \frac{\partial}{\partial x}(\rho\,V_x{}^2)\,r\,\partial\theta\,\partial r\,\partial x + \frac{\partial}{\partial r}(\rho\,V_r\,V_x)\,r\,\partial\theta\,\partial x\,\partial r \\
&+ \rho\,V_r\,V_x\,\partial\theta\,\partial x\,\partial r + \frac{\partial}{\partial\theta}(\rho\,V_\theta\,V_x)\,\partial r\,\partial x\,\partial\theta - \rho\,f_x\,r\,\partial r\,\partial\theta\,\partial x
\end{aligned} \tag{A.7}$$

The terms on the right-hand side of equation (A.7) are differentiated as follows:

$$\frac{\partial(\rho\,V_x{}^2)}{\partial x} = V_x\frac{\partial(\rho\,V_x)}{\partial x} + \rho\,V_x\frac{\partial V_x}{\partial x} \tag{A.8}$$

$$\frac{\partial(\rho\,V_r\,V_x)}{\partial r} = V_x\frac{\partial(\rho\,V_r)}{\partial r} + \rho\,V_r\frac{\partial(V_x)}{\partial r} \tag{A.9}$$

$$\frac{\partial(\rho\,V_\theta\,V_x)}{\partial\theta} = V_x\frac{\partial(\rho\,V_\theta)}{\partial\theta} + \rho\,V_\theta\frac{\partial(V_x)}{\partial\theta} \tag{A.10}$$

By using (A.8), (A.9), (A.10) inside (A.7), the right hand side of (A.7) becomes:

$$\begin{aligned}
V_x&\left[\frac{\partial(\rho\,V_x)}{\partial x} + \frac{\partial(\rho\,V_r)}{\partial r} + \frac{\rho\,V_r}{r} + \frac{\partial(\rho\,V_\theta)}{r\,\partial\theta}\right] r\,\partial\theta\,\partial r\,\partial x \\
&+ \rho\left(V_x\frac{\partial V_x}{\partial x} + V_r\frac{\partial V_x}{\partial r} + V_\theta\frac{\partial V_x}{r\,\partial\theta}\right) r\,\partial\theta\,\partial r\,\partial x
\end{aligned} \tag{A.11}$$

The first bracket of (A.11) is zero due to the continuity equation. The momentum equation becomes:

$$\begin{aligned}
\rho&\left(V_x\frac{\partial V_x}{\partial x} + V_r\frac{\partial V_x}{\partial r} + \frac{V_\theta}{r}\frac{\partial V_x}{\partial\theta}\right) r\,\partial\theta\,\partial r\,\partial x \\
&= \left(\frac{\partial\sigma_{xx}}{\partial x} + \frac{\partial\tau_{\theta x}}{r\,\partial\theta}\,\partial x\,\partial r\,\partial\theta + \frac{\partial\tau_{rx}}{\partial r} + \frac{\tau_{rx}}{r} + \rho\,f_x\right) r\,\partial\theta\,\partial x\,\partial r
\end{aligned} \tag{A.12}$$

The velocities of both the shell side and the tube side flows are taken as average values at any cross section.

$$\frac{\partial}{\partial r} = \frac{\partial}{\partial \theta} = 0 \qquad \text{(A.13)}$$

Finals forms of continuity equation (A.6) and momentum equation (A.12) becomes:

$$\frac{\partial(\rho\, V_x)}{\partial x} + \frac{(\rho\, V_r)}{r} = 0 \qquad \text{(A.14)}$$

$$\rho V_x \frac{\partial V_x}{\partial x} r\, \partial\theta\, \partial r\, \partial x = \left(\frac{\partial \sigma_{xx}}{\partial x} + \frac{\tau_{rx}}{r} + \rho\, f_x\right) r\, \partial\theta\, \partial x\, \partial r \qquad \text{(A.15)}$$

Integration equation (A.15) in r and Θ directions, from 0 to R (tube radius) and from 0 to 2π, respectively, momentum equation becomes:

$$\int_o^R \int_0^{2\pi} \rho\, V_x\, \frac{\partial V_x}{\partial x}\, r\, \partial r\, \partial\theta\, \partial x = \int_o^R \int_0^{2\pi} \left(\frac{\partial \sigma_{xx}}{\partial x} r + \tau_{rx} + \rho\, f_x r\right) \partial r\, \partial\theta\, \partial x \qquad \text{(A.16)}$$

$$\rho\, V_x\, \frac{\partial V_x}{\partial x}\, \frac{R^2}{2}\, 2\pi\, \partial x = \frac{\partial \sigma_{xx}}{\partial x}\, \frac{R^2}{2}\, 2\pi\, \partial x + \tau_{rx} R\, 2\pi\, \partial x + \rho\, f_x\, \frac{R^2}{2}\, 2\pi\, \partial x \qquad \text{(A.17)}$$

$$\rho\, V_x\, \frac{\partial V_x}{\partial x} = \frac{\partial \sigma_{xx}}{\partial x} + 2\frac{\tau_{rx}}{R} + \rho\, f_x \qquad \text{(A.18)}$$

Mass flux, G is defined as $G = \rho\, V_x$. For a system lumped in Θ and r directions, the only shear stress is at walls of the pipe and the only stress caused along x direction is due to the pressure.

$$\tau_{rx} = -\tau_w = -\frac{f\, \rho\, V_x^2}{2} \qquad \text{(A.19)}$$

$$\sigma_{xx} = -P \tag{A.20}$$

Where f is the Fanning friction factor. Placing (A.19) and (A.20) into (A.18), momentum equation becomes:

$$-\frac{\partial P}{\partial x} = G \frac{\partial V_x}{\partial x} + \frac{2 f \rho V_x^2}{d} - \rho f_x \tag{A.21}$$

Where d is the inner diameter of the finned capillary for tube side flow and hydraulic diameter for shell side flow. As the gas flow occurs only along the heat exchanger length, $V_r = V_\theta = 0$. The final form of the continuity equation is:

$$\frac{d(\rho V_x)}{dx} = V_x \frac{d\rho}{dx} + \rho \frac{dV_x}{dx} = 0 \tag{A.22}$$

$$\frac{dV_x}{dx} = -\frac{V_x}{\rho} \frac{d\rho}{dx} \tag{A.23}$$

$$\frac{dV_x}{dx} = -\frac{G}{\rho^2} \frac{d\rho}{dx} \tag{A.24}$$

Integrating (A.24) into (A.21), final form of the momentum equation becomes:

$$-\frac{dP}{dx} = -\frac{G^2}{\rho^2} \frac{d\rho}{dx} + \frac{2 f G^2}{\rho d} - \rho f_x \tag{A.25}$$

$$\frac{dP}{dx} = -\left(\frac{2 f G^2}{\rho d} - \rho f_x\right) + \frac{G^2}{\rho^2} \frac{d\rho}{dP} \frac{dP}{dx} \tag{A.26}$$

$$\frac{dP}{dx} = \left(\frac{2 f G^2}{\rho d} - \rho f_x\right) \Big/ \left(\frac{G^2}{\rho^2} \frac{d\rho}{dP} - 1\right) \tag{A.27}$$

For energy equation, the total energy, *TE*, is defined as follows:

$$TE = e + \frac{1}{2}(V_x{}^2 + V_r{}^2 + V_\theta{}^2)$$ (A.28)

Where e denotes the mass specific internal energy, $U/\dot{m}$. The energy balance is written such that:

$$\sum \dot{m}_\iota\,(TE) + \dot{Q} = \frac{dE_{cv}}{dt} + \sum \dot{m}_e\,(TE) + \dot{W}$$ (A.29)

Subscript "i" denotes mass inlet, "e" denotes exit, "cv" the control volume. The heat and work balances are written accordingly:

$$\dot{Q} = -\left[\frac{\partial(r\,\ddot{q}_r)}{\partial r} + \frac{\partial \ddot{q}_\theta}{\partial \theta} + \frac{\partial(r\,\ddot{q}_x)}{\partial x}\right]\partial r\,\partial\theta\,\partial x$$ (A.30)

$$\dot{W} = -\left[\frac{\partial(\sigma_{xx}\,V_x\,r)}{\partial x} + \frac{\partial(\sigma_{rr}\,V_r\,r)}{\partial r} + \frac{\partial(\sigma_{\theta\theta}\,V_\theta)}{\partial\theta} + \frac{\partial(\tau_{rx}\,V_r\,r)}{\partial x} + \frac{\partial(\tau_{rx}\,V_x\,r)}{\partial r}\right.$$
$$\left. + \frac{\partial(\tau_{\theta x}\,V_\theta\,r)}{\partial x} + \frac{\partial(\tau_{\theta x}\,V_x)}{\partial\theta} + \frac{\partial(\tau_{r\theta}\,V_\theta\,r)}{\partial r} + \frac{\partial(\tau_{r\theta}\,V_r)}{\partial\theta}\right]\partial r\,\partial x\,\partial\theta$$ (A.31)

Simplifying (A.31) using momentum and continuity equations, assuming steady state, energy equation becomes:

$$-\left[\frac{\partial(r\,\ddot{q}_r)}{\partial r} + \frac{\partial \ddot{q}_\theta}{\partial \theta} + \frac{\partial(r\,\ddot{q}_x)}{\partial x}\right]\partial r\,\partial\theta\,\partial x$$
$$= \rho\left[V_r\,\frac{\partial(r\,e)}{\partial r} + V_\theta\,\frac{\partial e}{\partial\theta} + V_x\,\frac{\partial(r\,e)}{\partial x}\right]\partial r\,\partial\theta\,\partial x$$
$$-\left[\sigma_{xx}\,\frac{\partial(V_x\,r)}{\partial x} + \sigma_{rr}\,\frac{\partial(V_r\,r)}{\partial r} + \sigma_{\theta\theta}\,\frac{\partial(V_\theta)}{\partial\theta} + \tau_{rx}\,\frac{\partial(V_r\,r)}{\partial x}\right.$$
$$+ \tau_{rx}\,\frac{\partial(V_x\,r)}{\partial r} + \tau_{\theta x}\,\frac{\partial(V_\theta\,r)}{\partial x} + \tau_{\theta x}\,\frac{\partial V_x}{\partial\theta} + \tau_{r\theta}\,\frac{\partial(V_\theta\,r)}{\partial r}$$
$$\left. + \tau_{r\theta}\,\frac{\partial V_r}{\partial\theta}\right]\partial r\,\partial x\,\partial\theta$$ (A.32)

Assuming that the flow properties are averaged at any cross section and there is only a flow in x direction:

$$\frac{\partial}{\partial r} = \frac{\partial}{\partial \theta} = 0 \ , V_r = \ V_\theta = 0$$

(A.32) takes the form:

$$\left(\ddot{q}_r + r\frac{\partial \ddot{q}_x}{\partial x}\right)\partial r \ \partial \theta \ \partial x = \rho \ V_x \ r\frac{\partial e}{\partial x} \ \partial r \ \partial \theta \ \partial x \ - \left(\sigma_{xx} \ r \ \frac{\partial V_x}{\partial x} + \tau_{rx}V_x\right)\partial r \ \partial x \ \partial \theta \qquad \text{(A.33)}$$

Integrating (A.33) in r and Θ directions from 0 to R and 0 to 2π respectively, energy equation becomes:

$$\ddot{q}_r 2\pi \ R + \frac{d\ddot{q}_x}{dx}R^2\pi = \rho \ V_x \ \frac{de}{dx} \ R^2\pi \ - \sigma_{xx} \ \frac{dV_x}{dx} \ R^2\pi + \tau_{rx}V_x \ 2\pi \ R \qquad \text{(A.34)}$$

The equation of enthalpy in terms of internal energy can be rewritten as follows:

$$i = e + Pv \qquad \text{(A.35)}$$

$$e = i - \frac{P}{\rho} \qquad \text{(A.36)}$$

$$\frac{de}{dx} = \frac{di}{dx} - \frac{1}{\rho}\frac{dP}{dx} + \frac{P}{\rho^2}\frac{d\rho}{dx} \qquad \text{(A.37)}$$

Rewriting (A.34) with (A.37):

$$\ddot{q}_r 2\pi \ R + \frac{d\ddot{q}_x}{dx}R^2\pi$$
$$= G \ R^2\pi \left(\frac{di}{dx} - \frac{1}{\rho}\frac{dP}{dx} + \frac{P}{\rho^2}\frac{d\rho}{dx}\right) + P \ R^2\pi \frac{dV_x}{dx} - \frac{f \ \rho \ V_x{}^2}{2}V_x \ 2\pi \ R \qquad \text{(A.38)}$$

$$\ddot{q}_r 2\pi \ R + \frac{d\ddot{q}_x}{dx}R^2\pi = \pi R^2 \left(G \ \frac{di}{dx} - V_x\frac{dP}{dx}\right) - f \ \rho \ V_x{}^3 \ \pi \ R \qquad \text{(A.39)}$$

For a pure substance:

$$di = \left(\frac{\partial i}{\partial T}\right)_P dT + \left(\frac{\partial i}{\partial P}\right)_T dP \qquad \text{(A.40)}$$

$$\left(\frac{\partial i}{\partial T}\right)_P = c_p \qquad \text{(A.41)}$$

$$di = T\,ds + v\,dP \;\rightarrow\; \left(\frac{\partial i}{\partial P}\right)_T = T\left(\frac{\partial s}{\partial P}\right)_T + \frac{1}{\rho}\left(\frac{\partial P}{\partial P}\right)_T \qquad \text{(A.42)}$$

$$di = c_P dT + T\left(\frac{\partial s}{\partial P}\right)_T dP + \frac{1}{\rho}\,dP \qquad \text{(A.43)}$$

Combining (A.39) and (A.43):

$$\dot{q}_r 2\pi R + \frac{d\ddot{q}_x}{dx}\pi R^2$$
$$= \pi R^2 \left[G c_P \frac{dT}{dx} + G\,T\left(\frac{\partial s}{\partial P}\right)_T \frac{dP}{dx} + \frac{G}{\rho}\frac{dP}{dx} - V_x \frac{dP}{dx}\right] - f\,\rho\,V_x^{\,3}\,\pi R \qquad \text{(A.44)}$$

$$2\pi R\left(\dot{q}_r + \frac{f\,\rho\,V_x^{\,3}}{2}\right) = \pi R^2\left[-\frac{d\ddot{q}_x}{dx} + G c_P \frac{dT}{dx} + G\,T\left(\frac{\partial s}{\partial P}\right)_T \frac{dP}{dx}\right] \qquad \text{(A.45)}$$

Axial conduction within the fluid, $\dot{q}_x$, and viscous dissipation term are neglected. Heat transfer in radial direction is the convection with solid bodies. Final form of the energy equation can be rewritten as:

$$A_{cross,fluid}\left[G c_P \frac{dT}{dx} + G\,T\left(\frac{\partial s}{\partial P}\right)_T \frac{dP}{dx}\right] = P_{w,solid}\left[h\left(T_w - T_{fluid}\right)\right] \qquad \text{(A.46)}$$

CALCULATION OF THERMOPHYSICAL AND TRANSPORT PROPERTIES OF ARGON

To determine the thermophysical properties of argon, the study of Stewart et al. [14] and for transport properties such as viscosity and conductivity, the study of Lemmon et al. [13] are used.

In the study of Stewart, an equation for calculation of Helmholtz energy is given. The Helmholtz energy is divided into two parts, which are contribution of ideal gas and contribution of compressibility of the real gas.

$$a(\rho, T) = a^o(\rho, T) + \bar{a}(\rho, T) \qquad (A.47)$$

Contribution of ideal gas is calculated through the reference values given in the article.

$$a^o = \frac{H_0{}^o \tau}{R\, T_c} - \frac{S_0{}^o}{R} - 1 + \ln \frac{\delta\, \tau_0}{\delta_0\, \tau} - \frac{\tau}{R} \int_{\tau_0}^{\tau} \frac{c_p{}^o}{\tau^2} d\tau + \frac{1}{R} \int_{\tau_0}^{\tau} \frac{c_p{}^o}{\tau} d\tau \qquad (A.48)$$

Where parameters with subscript "0" are given in reference conditions, which is at 298.15 K temperature and 0.101325 MPa pressure. τ and δ are non-dimensional temperature and density, which are calculated as $\tau = T_c/T$ and $\delta = \rho/\rho_c$. H denotes the enthalpy, S denotes the entropy, c_p denotes the specific heat and R is the universal gas constant.

Contribution of the compressibility of the real gas is given as a summation which is a function of δ and τ. The summation consists of 28 terms, each term having four constant coefficient. Similarly, vapor pressure for a given temperature, saturated

liquid density and saturated vapor density are also given as functions of τ, each having multiple terms.

Once the Helmholtz energy contribution of ideal gas and compressibility of the real gas are calculated, pressure (P), internal energy (u), enthalpy (h), entropy (s), specific heat (c_p) are calculated as given below:

$$P = P_c \frac{\delta}{\tau \, Z_c} \left(1 + \delta \frac{\partial \bar{a}}{\partial \delta} \right) \tag{A.49}$$

$$u = R \, T \, \tau \left(\frac{\partial a^o}{\partial \tau} + \frac{\partial \bar{a}}{\partial \tau} \right) \tag{A.50}$$

$$h = R \, T \, \tau \left(\frac{\partial a^o}{\partial \tau} + \frac{\partial \bar{a}}{\partial \tau} \right) + \delta \frac{\partial \bar{a}}{\partial \delta} + 1 \tag{A.51}$$

$$s = R \, \tau \left(\frac{\partial a^o}{\partial \tau} + \frac{\partial \bar{a}}{\partial \tau} \right) - a^o - \bar{a} \tag{A.52}$$

$$
\begin{aligned}
c_p = {} & -R \, \tau^2 \left(\frac{\partial^2 a^o}{\partial \tau^2} + \frac{\partial^2 \bar{a}}{\partial \tau^2} \right) \\
& + R \left(1 + \delta \frac{\partial \bar{a}}{\partial \delta} - \delta \, \tau \frac{\partial^2 \bar{a}}{\partial \delta \partial \tau} \right)^2 \bigg/ \left(1 + 2 \, \delta \frac{\partial \bar{a}}{\partial \delta} + \delta^2 \frac{\partial^2 \bar{a}}{\partial \delta^2} \right)
\end{aligned}
\tag{A.53}
$$

For the model developed in this study, temperature and pressure are given as input parameters. However, the equations above require temperature and density as input parameters. Pressure is a calculated value. It is not possible to derive an analytical equation for calculation of density with temperature and pressure as input values from the given equations. Therefore, a code is generated in order to find the density. An initial guess for density is done depending on whether the temperature and pressure are higher or lower than the critical values. For this initial guess, a pressure is calculated from equation (A.49). By comparing the guessed pressure with the input value, the density value is updated using Newton-Rhapson method. The final value of

density is calculated with an error between input pressure and calculated pressure below 10^{-8}.

The flowchart of the code for calculation of thermophysical properties is given in Figure B.1.

In [13], viscosity is calculated by summation of contribution of dilute gas viscosity and residual fluid viscosity.

$$\mu(T) = \mu^o(T) + \mu^r(\tau, \delta) \qquad \text{(A.54)}$$

The dilute gas contribution is calculated as follows:

$$\mu^o(T) = \frac{0.0266958 \sqrt{M\,T}}{\sigma^2\,\Omega\,(T^*)} \qquad \text{(A.55)}$$

Where M is the molar weight, σ is the Lennard-Jones size parameter, Ω is the collision integral and T^* is the ratio of the temperature to Lennar-Jones energy parameter. Contribution of the residual fluid viscosity is given as a summation of 6 terms which are functions of τ and δ.

The thermal conductivity is calculated as a summation of 3 parts, which are contribution of dilute gas thermal conductivity, residual fluid thermal conductivity and thermal conductivity critical enhancement.

$$k(T) = k^o(T) + k^r(\tau, \delta) + k^c(\tau, \delta) \qquad \text{(A.56)}$$

The contribution of dilute gas thermal conductivity is given as follows:

$$k^o = N_1 \left[\frac{\mu^o(T)}{1\,\mu\,\text{Pa.s}} \right] + N_2 \tau^{t_2} + N_3 \tau^{t_3} \qquad \text{(A.57)}$$

Where N_1, N_2, t_1 and t_2 are constants. Contribution of the residual gas thermal conductivity is given as a summation of 6 terms, which are functions of τ and δ. For calculation of thermal conductivity enhancement in the critical region, the equation of Ochowy and Senger is used as follows:

$$k^c = \rho \, c_p \frac{B \, R_0 \, T}{6 \, \pi \, \xi \, \eta(T,\rho)} (\tilde{\Omega} - \tilde{\Omega}_0) \qquad \text{(A.58)}$$

Where B is the Boltzmann's constant (usually denoted with k), R_0 is a constant, ξ is a fluid-specific term and $\tilde{\Omega}$ is a function of specific heat and fluid-specific terms, which require calculation of derivative of density with respect to pressure at constant temperature.
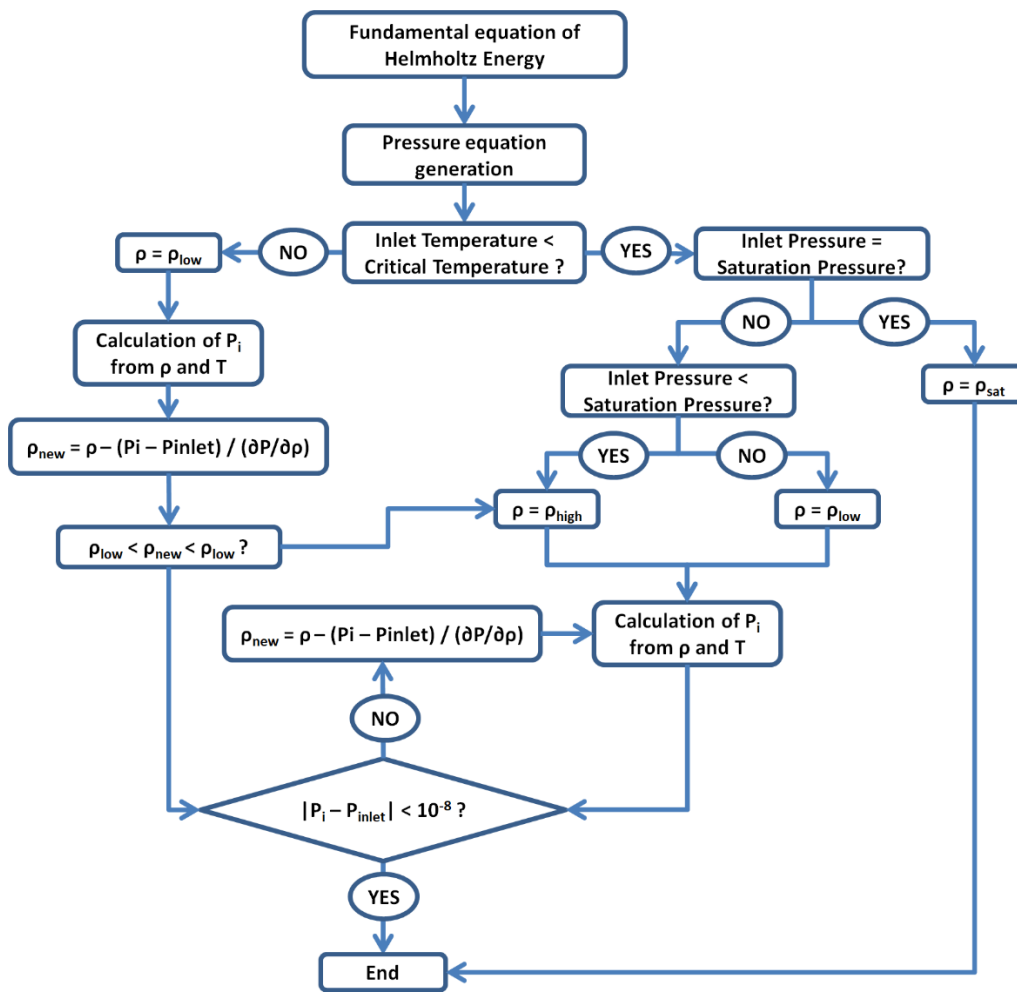

Figure B.1. Flowchart of the code generated for calculation of thermophysical properties of argon

CURRICULUM VITAE

PERSONAL INFORMATION

Surname, Name: Baki, Murat

Nationality: Turkish (TC)

Date and Place of Birth: 6 July 1988, Ankara

Marital Status: Married

Phone: +90 533 360 73 47

email: muratbaki@yahoo.com

EDUCATION

Degree	Institution	Year of Graduation
MS	University of Duisburg Essen, Mechanical Engineering	2012
BS	METU, Mechanical Engineering	2009
High School	TED Ankara Collage Private High School, Ankara	2005

WORK EXPERIENCE

Year	Place	Enrollment
2012-Present	ASELSAN, MGEO	Mechanical Design Engineer
2010-2011	Zentrum für Brennstoffzellen Technik	Student Researcher
2008 July	Türk Traktör	Intern Engineering Student
2007 August	FMC Nurol	Intern Engineering Student

FOREIGN LANGUAGES

Advanced English, Intermediate German

PUBLICATIONS

F. Can, A. B. Erdogmus, M. Baki, M. K. Aktas. *Cooling Characterization of Conceptual Joule-Thomson Cryogenic Cooler*. International Conference of Cryogenics and Refrigeration Technology, 22 – 25 June 2016, Bucharest, Romania

F. Can, A. B. Erdoğmuş, M. Baki, M. K. Aktaş, M. A. Güler. *Design of miniature bellow in a conceptual Joule-Thomson cooler*. International Cryocooler Conference 19 (ICC 19), 20 – 23 June 2016, San Diego, CA

M. Baki, T. Okutucu Özyurt, C. Sert. *Kriyojenik bir soğutucunun alt parçası olan, ters akışlı, reküperatif, helisel sarımlı kılcal boru ısı değiştiricinin sayısal modelinin oluşturulması*. ULIBTK'17, 13 – 16 Eylül 2017, Çorum, Türkiye

M. Baki, H. T. Okutucu Özyurt, C. Sert. *Improved 1D Numerical Model and Optimization of Joule-Thomson Cryocoolers*. Cryogenics (in progress)